12-2014

Majorana Fermions in Chiral Topological Superconductors

Eugen Florin Dumitrescu
Clemson University

MAJORANA FERMIONS IN CHIRAL TOPOLOGICAL SUPERCONDUCTORS

A Dissertation
Presented to
the Graduate School of
Clemson University

In Partial Fulfillment
of the Requirements for the Degree
Doctor of Philosophy
Physics

---

by
Eugen Florin Dumitrescu
December 2014

Accepted by:
Dr. Sumanta Tewari, Committee Chair
Dr. Catalina Marinescu
Dr. Murray Daw
Dr. Jian He

Abstract

Majorana fermions were first proposed in the context of high energy physics by Ettore Majorana in 1937, just before his mysterious disappearance. Now, over 70 years later, signatures of condensed matter analogues of Majorana fermions are finally appearing in low-dimensional superconductor-based heterostructures. In low-dimensional systems, these order parameter, defect-bound Majorana quasiparticles obey non-Abelian quantum statistics and can therefore be used as the building blocks of a topological quantum computer. In this thesis we will analyze the signatures associated with, and the robustness of, Majorana bound states in a variety of one-dimensional superconducting platforms. Our main result is the finding that spatially localized Majorana modes may coexist, without an induced energy splitting, in the presence of additional symmetries. The effects and robustness of Majorana bound states in the presence of timer-reversal, chiral and spatial symmetries are analyzed in detail. Our results allow us to explain the unexpected robustness of a zero-bias signal in recent experiments purporting to observe Majorana excitations.

Acknowledgments

I would like to thank the many people who made my research at Clemson and this thesis in particular a great experience. To Dr. Tewari, I am grateful for the many discussions and effort you put into guiding me through this research project. It has been a pleasure working with you and I am excited to put the knowledge gained at Clemson to use in the next stage of my scientific career. To my committee members, I am very grateful for advice I've been given about research and perspective on what it means to be a scientist in general. Your words have helped inspire and motivate me many times. Additionally, I thank my parents and close friends for their constant support and encouragement. Your support was crucial in the successful completion of this work.

Table of Contents

Title Page . . . . . **i**

Abstract . . . . . **ii**

Acknowledgments . . . . . **iii**

List of Tables . . . . . **v**

List of Figures . . . . . **vi**

1 Introduction **1**
1.1 Majorana Fermions as Fundamental particles 1
1.2 Topological quantum computation 6
1.3 Non-Abelian anyons and topological phases of matter 10
1.4 Emergent Majorana fermions in superconductors 14

2 Topological thermoelectric effects in spin-orbit coupled electron and hole doped semiconductors 20
2.1 Berry phase and topological Hall and Nernst effects 22
2.2 Topological Hall and Nernst effects in electron doped semiconductors 24
2.3 Topological Hall and Nernst effects in hole doped semiconductors 27

3 Topological Properties of one-dimensional superconductors 36
3.1 Topological superconducting platforms 37
3.2 The spinfull Kitaev model and chiral symmetry 40
3.3 True time-reversal invariance 46
3.4 Spatial reflection symmetry 54
3.5 Conclusion 62

4 Majorana Bound States in Chiral Ferromagnetic Nanowires 64
4.1 Introduction 65
4.2 Experimental Setup and Theoretical Model 69
4.3 Topological Properties and Quantum Phase Transitions 71
4.4 Scanning Tunneling Differential Conductance 76
4.5 Experimental Implications 81
4.6 Chiral Fractional Josephson Effect 91
4.7 Summary 93

5 Conclusions and Summary 95
5.1 Summary of results 95
5.2 Future Directions 97

Bibliography 100

List of Tables

3.1 Possible one-dimensional topological invariants in the presence of various perturbations . . . 53

List of Figures

1.1 A spatially dependent mass term (red) $\phi(x) = tanh(z)$ with a sign flip at the origin. With this potential there exists a single zero energy mode, $\psi(x) = \exp\left[-(mc/\kappa)\int \phi(x')dx'\right]$ (blue) which is localized to the domain wall. 5

1.2 The state of a two level quantum system is represented by a unit vector on the Bloch sphere. Any controllable two level quantum system can be used as a qubit. 8

1.3 A simple two qubit quantum circuit involving Hadamard and controlled-NOT gates in series followed by a measurement operation on both qubits. 10

1.4 Panel (a) shows the operation $\hat{T}$ which swaps two particles. Panel (b) shows a braid which is topologically equivalent to two swaps, i.e. $\hat{T}^2$. 11

1.5 Panel (a): Probability amplitude of a Bogoliubov quasiparticle (red line) bound to a defect in the order parameter (dashed blue). Panel (b): Caroli, de-Gennes, Matricon energy levels for defect bound quasiparticles in a s-wave superconductor (red) and vortex bound energies in a topological p-wave superconductor (light blue). 18

1.6 a) The electron operators on each site may be decomposed into their real and imaginary parts, each of which is described by a Majorana operator. Eq. 1.25 Kitaev shows the Hamiltonian (for specific parameters) can be written in terms of Majoranas coupled from the same site, or adjacent sites. b) The leftover Majorana operators come from the two ends of the wire and leak into the bulk for generic parameters values. 19

2.1 Contour plot of the Berry curvature $\mathbf{\Omega}_-$ in the lower band of electron-doped semiconductors. The Berry curvature is sharply peaked at a finite value of k_x near the band-degeneracy point in the absence of the Dresselhaus coupling. 25

2.2 Anomalous Hall conductivity versus chemical potential μ at zero temperature for a two-dimensional electron-doped semiconductor. We have used $\alpha_R = \alpha_D = 4.74 \times 10^4$ m/s $m^* = .067m_e$ and $h_y = 0.2$ meV. The electronic band structure versus k_x is shown in the inset along with the minimum energy gap Δ indicated by the dashed lines 26

2.3 Anomalous Nernst coefficient versus chemical potential for 2DEG. The dashed lines show the regime of the energy gap Δ between the bands. The same parameters have been used as in Fig 2.2 with the exception of $T = 0.1K$ 28

2.4 (a) Band structure of the 2DHG in the k_x direction for $k_y = 0$. (b) Energy gap at origin between lower bands. Here we have used $\alpha_R = \alpha_D = 2 \times 10^5$ m/s, $h_y = 5$ meV, $\gamma_1 = 6.92$,$\gamma_2 = 2.1$, $\gamma_3 = 2.9$ and $a = 8nm$ which are chosen for GaAs. 29

2.5 (Color online) Contour plot of the Fermi surface at μ corresponding to the topological regime ($\mu = -8.5$ meV). Color plot indicates the proportion of light-hole character ($m_j = \pm 1/2$) in the top valence band. 31

2.6 (Color online) Contour plot of Berry curvature of each band (units of m^2) where (a) corresponds to the lowest band and (d) to the highest. The y and x axis are k_y and k_x respectively with units of m^{-1}. As seen from the denominator of Eq. (2.10) these functions are sharply peaked at values of **k** near the near-band-degeneracy points. 32

2.7 Plot of the anomalous Hall conductivity for the hole doped semiconductor at T=0 with the same paramaters as those used in Fig. 2.4. 33

2.8 Plot of the anomalous Nernst coefficient for the $[110]$ grown hole-doped quantum well near the topological regime of the chemical potential. The topological regime of μ is characterized by a plateau of the anomalous Nernst coefficient (at vanishing values) flanked by two peaks of opposite signs as in the case of the electron-doped semiconductors. The parameters used are the same as in Fig. 2.4 except that $T = 0.1K$. 34

3.1 (Color online) (a) Low energy BdG quasiparticle spectrum for TR-symmetric Kitaev chain corresponding to Eq. (3.1) which hosts a pair of Majorana Fermions. The parameters used are as follows: $\Delta_0 = 0.5$meV, $\mu = 0.75$ meV, $N = 300$ sites, $a = 15$ nm, corresponding to a wire length of 4.5μm and a hopping amplitude of $t = 11$meV. (b) The response of the low energy spectrum to the TR-breaking perturbations given in Eq. (3.2). We have added bulk Zeeman splitting (red circles, $V_y, V_z = 0.4$ meV), magnetic impurity (blue squares) at wire endpoints of magnitude $J_y, J_z = 1$ meV, and mixing by the $S_y = 0$ ($S_z = 0$) component of the order parameter $\Delta_{\uparrow\uparrow} = \Delta_{\downarrow\downarrow} = 0.5\Delta_0$, green diamonds ($\Delta_{\uparrow\downarrow} = \Delta_{\downarrow\uparrow} = 0.5\Delta_0$, yellow triangles). (c) Zeeman splitting in the $\hat{x}$ direction ($V_x = 0.1$ meV, red circles) and localized at the endpoints ($J_x = 0.5$ meV, blue squares) split the MFs to finite energy 39

3.2 (Color online) Parametric plots of Re$(Det(A(k)))$ and Im$(Det(A(k)))$ as the momentum k is varied through the 1D Brillouin zone from $k = -\pi$ and π. (a) The winding of the angle $\theta(k)$ for the TR-symmetric Kitaev chain in the topologically non-trivial (red) and trivial (blue) phases corresponding to $|\mu| < 2t$ and $|\mu| > 2t$, respectively, indicating the existence of 2 and 0 MFs at each end. (b) The winding number in the presence of perturbation ($\Delta_{\uparrow\uparrow} = \Delta_{\downarrow\downarrow} = 0.5\Delta_0$), and 3 values of the Zeeman splitting, $V_y, V_z = 0.5\mu$ (red), 1.5μ (blue), and 3.3μ (purple). With increasing Zeeman fields, the Fermi surfaces disappear in turn and W decreases from 2 (red) to 1 (blue) to 0 (purple) indicating the corresponding disappearance of the MFs. 42

3.3 (a) The winding of the angle $\theta(k)$ for the ($S_y = 0$) Kitaev chain with $\Delta_{\uparrow\uparrow} = \Delta_{\downarrow\downarrow}$ with the two spin sectors uncoupled (red) and coupled by a Zeeman splitting $V_y = 0.25$ meV (blue). In both cases $W = 0$. (b) Low energy BdG spectrum for the uncoupled spins (red circles) shows 2 *topologically unprotected* MFs at each end. Since the MFs are unprotected (see text), even a chiral symmetric perturbation $V_y = 0.25$ meV splits them to finite energy (blue squares). (c) Increasing the Zeeman splitting in the $\hat{z}$ direction ($V_z > \mu$) drives the system through a topological phase transition into a phase with winding number $W = 1$. We show the winding for uncoupled spins (red) and with additional Zeeman splitting $V_y = 0.25$ meV (blue). (d) Low energy BdG spectrum in the $W = 1$ regime for uncoupled spins (red circles) and in the presence of V_y (blue squares) illustrating the topological protection of the MF. . . 44

3.4 (a) Low energy BdG spectrum of four parallel chains coupled by transverse hopping t_y. $t_y/t_x = 0.2, 0.75, 1.5$ correspond to 8 (red circles), 6 (blue circles), and 4 (green diamonds) MFs at each end. (b) Quasiparticle gap closing and TQPT (separating phases with different number of MFs) tuned by the transverse hopping. Panels (c, d) show the bulk energy-momentum dispersion in the gapped regime with 8 MFs and as the bulk gap closes leading to the regime with 6 MFs at each end. 45

3.5 (a) Low energy ABS spectrum as a function of ϕ for TR-symmetric Kitaev chain with parameters as in Fig. 1. Each red curve is twofold degenerate. (b) TR-breaking bulk Zeeman fields $V_y, V_z = .25$ meV lift the degeneracy but preserves the 4π periodicity of the spectrum. (c) Adding the order parameter component with $\Delta_{\uparrow\uparrow} = \Delta_{\downarrow\downarrow} = 0.5\Delta_0$, although it breaks the TR symmetry, preserves the 4π periodicity (d) The spectrum with $V_x = 1$ meV added to the junction breaks chiral symmetry and results in a conventional 2π Josephson effect. 47

3.6 (Color online) (a) Probability amplitude $|\Psi(x)|$ of the lowest energy solution to Eq. 3.6 on a finite system with a length of 300 sites. (b) The low energy BdG spectrum as a function of chemical potential μ. Each band is doubly degenerate, with 2 MBSs at each end of the nanowire in the $|\mu| < 2\alpha_R$ topologically non-trivial regime. (c) Parametric plot of $\mathrm{Re}(Det(A(k)))$ and $\mathrm{Im}(Det(A(k)))$ as the quasi-momentum k is varied through the 1D Brillouin zone ($k \in [-\pi, \pi]$). The red curve ($|\mu| < 2\alpha_R$, non-trivial regime) winds about the origin twice as k is varied through the Brillouin zone yielding a chiral invariant $W = 2$. Upon increasing the chemical potential, the blue curve ($|\mu| > 2\alpha_R$ topologically trivial regime) winds about the origin 0 times indicating a decrease in the chiral invariant from $W = 2$ to $W = 0$. 49

3.7 (Color online) (a) Winding curves for the bulk BdG Hamiltonian given by Eqs. (3.6,3.9) which preserves the chiral symmetry ($\boldsymbol{b} \perp \hat{a}$). The red, blue, and green curves yield chiral invariants $W = 2, 1, 0$ connected by gap closures and topological phase transitions. (b) Low energy BdG quasiparticle spectrum corresponding to the winding curves in panel (a). Here N counts the number of positive (negative) energy eigenvalues above (below) the Fermi energy. The chiral invariant counts the number of topologically protected modes at each end of the nanowire. 51

3.8 (Color online) (a) Energy splitting of the MBSs in the presence of Zeeman splitting V along $\hat{y}$ (along the direction of spin orbit direction) as described in Eq. (3.9). (b) Energy splitting as a function of Zeeman field along three orthogonal directions $\boldsymbol{b}_{1,2,3}$ described in the text on a log-log scale are found (from the slope) to split as V,V^3 and V^5, where V is the magnitude of the Zeeman field. Thus, in the presence of next-nearest neighbor spin-orbit coupling described by Eq. 3.10, the MBSs split in every direction. Both axes are in units where the pairing potential $\Delta_1 = 2$. 54

3.9 (Color online) (a) Chiral topological invariant $W = 2$ indicating two topologically protected MFs at each end of a single chain described by Eq. (3.15) (b) Mirror topological invariant $\gamma_M = 2$ (difference of the winding numbers in the two mirror subsectors) also indicating two MFs at each end of a single chain in Eq. (3.15). 57

3.10 (Color online) Phase diagram for a double chain set-up of TR-invariant Kitaev system (or generic class DIII superconductors) coupled by weak transverse hopping $t_y \ll t_x$. A large range of μ accommodates the topological phase indexed by the topological invariant $|W| = 4$ which counts the number of localized Majorana modes at each end. 59

3.11 (Color online) Low energy BdG quasiparticle spectrum for TR-symmetric Kitaev system (class DIII superconductor) for $N_y = 2$ (red circles) in the absence of chiral and mirror symmetries. The eight MFs (four on each end) are protected from splitting by spatial reflection. Blue squares show same number of protected zero modes in the presence of local chemical potential disorder which breaks spatial reflection. Green diamonds and black triangles show two MFs at each end for class D, $N_y = 2$, systems with or without spatial reflection, respectively. 60

3.12 (Color online) Effects of reflection symmetry breaking on the two dimensional band-structure. We have taken periodic boundary conditions along the y-direction and open boundary conditions along x. (a) In the presence of reflection symmetry, and one of chiral or time-reversal symmetries, a highly degenerate Majorana flat-band emerges if the transverse hopping is small (i.e. $t_y \ll t_x$). (b) Reflection symmetry breaking by the addition of a transverse ($\alpha \sin(k_y)$) Rashba type spin-orbit coupling term splits the Majorana band at all k_y except the TR-invariant momenta $k_y = 0, \pi$. (c) Uniform hopping $t_y = t_x$ gaps out most of the flat-band except for the states near the origin in momentum space. (d) A single degenerate point remains in the presence of uniform hopping and transverse spin-orbit coupling. 61

4.1 Schematic diagram of the proposed ferromagnetic heterostructure 71

4.2 Comparison of the topological band-structure for the class D and BDI systems 72

4.3 (Color online) (a) The zero-bias differential conductance as a function of chemical potential μ for various wire widths W. Since each Majorana modes contributes a factor of $2e^2/h$ to the zero-bias signal, this measurement directly probes the number of Majorana states present. For a given geometry the maximum possible conductance is $G_{max} = 4We^2/h$ (not shown here). (b) Representative dI/dV curves from parameter regimes with an integer topological invariant $|W| = (0, 1, 2)$ are given by the green, blue and red curves respectively. Inset shows the quantized peak height for the blue ($2e^2/h$) and red ($4e^2/h$) curves. (c) Finite temperature thermally broadens the zero-bias conductance peak width as well as reducing the height to well below the quantized value of $2e^2/h$. (d) Weak STM - FM nanowire coupling, i.e. small t', in conjunction with finite temperature ($T = 0.05t$) further reduces the peak height. . . . 78

4.4 (Color online) Spatially resolved differential conductance profiles from the left edge to the middle of a wire with $L = 200$. Panels a)-d) are broadened by temperatures $T = (0, 0.005, 0.010, 0.015)t$. Note the color scales are different in each panel and we present the the zero-bias signal in panel e) for clarity. See discussion below Eq. 4.9 for a note on the $T = 0$ result. 80

4.5 (Color online) Majorana wavefunctions for small ($\Delta = 0.01t$), and large ($\Delta = 0.1t$), pairing regimes as calculated for short ($L = 100$) and long ($L = 700$) systems. For both lengths considered in the large pairing regime, panels a,b), the Majorana decay length is much smaller than the system length ($\xi \ll L$), so the zero energy excitations are heavily localized to the FM wire endpoints. Panels c,d) illustrate how reducing the pair potential to $\Delta = 0.01t$ substantially increases the Majorana decay length and while a 700 site system still hosts Majorana states, considerable wavefunction overlap in the 100 site system hybridizes the end modes into conventional, delocalized quasiparticle states. Panels e,f) show the logarithm of the energy splitting ΔE between the two Majorana modes. As the wire length L increases ΔE falls off exponentially. Majorana decay lengths of of $\xi \sim 10$ sites, in the large pairing regime, and $\xi \sim 99$ sites, for the small pairing regime, are extracted from the black linear fits in panels e,f) respectively. 83

4.6 (Color online) Zero-bias differential conductance peak height, panels correspond to same parameter values as used in Fig. 4.5 panels a-d), at one end of the wire ($x = 0$) as a function of STM-FM coupling t' and temperature T. Panels a-c) When the Majorana decay length is significantly shorter than L a quantized zero-bias signal of $2e^2/h$ is seen at zero temperature and $t' > 0.03t$ (dark red on logarithmic color scale). The quantized signal decays rapidly by introducing finite temperature or decreasing t'. Panel d) No zero-bias signal is present near zero temperature (see below Eq. 9 for details) due to Majorana hybridization which splits the zero-bias peak into two separate finite bias signals. The cause of this effect is finite temperature, which smears two finite-bias peaks together for an effective zero bias signal (see to Fig. 4.9 for details). 84

4.7 (Color online) Differential conductance calculated using an STM coordinate $x = 0, L/4, , L/2$ for a long wire $L = 700$ in the small pairing regime. Solid and dashed lines are at temperature $T = 0, 0.01t$ respectively, and green (red) lines correspond to a STM-FM coupling of $t' = 0.01t$ $(0.005t)$. Panel a) shows a clear zero-bias signature which is visible at the wire endpoints for both zero and finite temperature. The green dashed line ($T = \Delta$) displays a peak height ($10^-3e^2/h \sim 40nS$) and width ($\sim \Delta$) which are comparable to the experimentally reported values. Panels b,c) The zero temperature Majorana peak decays as the STM moves into the FM nanowire bulk. The peak completely vanishes at the midpoint, and is not visible at zero or finite temperature signal. 86

4.8 (Color online) Differential conductance spatial profile as a function of the STM coordinate x. Panels a) b) correspond to temperature $T = 0, 0.01t$ respectively, and we present the zero temperature data on a logarithmic scale for improved visibility. At zero temperature, the spatially localized Majorana mode resides within a well defined superconducting gap which not visible at finite temperature due to thermal smearing effects. Note that the true spatial extent of the Majorana mode is revealed by the finite temperature result, i.e. on a linear scale. 87

4.9 (Color online) When the ferromagnetic nanowire is short (i.e. $L \sim \xi$) Majorana bounds states at opposite ends hybridize as their wavefunctions overlap significantly in the bulk. Panel a) Using the same parameters from the Fig. 4.8 except $L = 100$, we see that the zero-bias Majorana signature splits into two distinct peaks centered near $V = \pm 0.01t$. The green, red, and blue curves correspond to the differential conductance calculated at $x = 0, L/4, L/2$ respectively, and the solid (dashed) lines denote the zero (finite $T = \Delta = 0.01t$) temperature. Panels b,c) Spatially resolved differential conductance along the longitudinal axis for zero (on a log scale) and finite temperature. Solid and dashed lines indicate the position of the dI/dV curves presented in panel a). 88

4.10 a) Top view of ring geometry JJ formed by weakly coupling ($t'' = t/10$) the two ends of a nanowire. The phase difference across the junction is controlled by the magnetic flux, Φ, threading the ring. b) Evolution of subgap Andreev bound states as a function of the phase difference between two superconductors in a Josephson junction setup. Zero energy crossings are absent in the ABS spectrum in the topologically trivial regime. c) In the $|\mathcal{W}| = 1$ phase, the ABS spectrum crosses zero energy for the single value $\phi = \pi$. Transitions between the subgap branches are forbidden by particle-hole symmetry so that Fermion parity flips as ϕ evolves by 2π. d,e) Spectra in a system indexed by topological invariant $|\mathcal{W}| = 3, 5$. There are $|\mathcal{W}|$ protected zero energy crossings and chiral symmetry forbids transitions between different sets of subgap branches. 91

Chapter 1

Introduction

The goal of this first chapter is to introduce the reader to central concepts including Majorana fermions in general, topological quantum computation and emergent quasiparticles in superconductivity. Beginning with a historical perspective, we introduce Majorana fermions as originally proposed in the context of high energy particle physics by Ettore Majorana. Fundamental particles which are candidates for Majorana fermions are discussed here and we end by commenting on the status of neutrino-less double-beta decay experiments currently being performed.

Next, we provide an introduction to quantum information theory and quantum computation. Quantum logic operations as well as quantum error correction schemes are discussed. In qualitative terms, we then introduce the paradigm of topological quantum computation and explain how this approach to quantum computation provides an route to decoherence free quantum computation.

Afterwards we turn our attention to condensed matter realizations of topological quantum field theories which can be used in topological quantum computation. We also provide an introduction as to how Majorana bound state, which should obey non-Abelian quantum exchange statistics, emerge in condensed matter systems as quasiparticle excitations in certain superconducting systems.

1.1 Majorana Fermions as Fundamental particles

In 1926 Erwin Schrödinger introduced his famous wave equation describing the time evolution of a quantum state[1]. The Schrödinger equation is a wave equation which determines the time evolution of a

quantum mechanical wavefunction $\Psi \equiv \Psi(r,t)$,

$$i\hbar\frac{\partial\Psi}{\partial t} = H\Psi \tag{1.1}$$

The solution Ψ describes a particle of mass m in the presence of a possibly spatially varying and time dependent potential $V \equiv V(r,t)$. The wavefunction is related to the probability amplitude ($\rho(x,t) = |\Psi(x,t)|^2$) and must meet the normalization condition $\int d^3x|\Psi|^2 = 1$. Physically this means that the particle exists somewhere in space. The Hamiltonian in classical mechanics is a function defined over phase space (coordinates and momenta q_i, p_i) which is the sum of kinetic and potential energy, $H = p^2/(2m) + V$. Using the differential momentum operator $p \mapsto -i\hbar\nabla$ the quantum mechanical Hamiltonian operator becomes

$$H = \frac{-\hbar^2}{2m}\nabla^2 + V(r,t) \tag{1.2}$$

where the first term represents the kinetic energy and the second is the potential energy.

Spin, which is represented by $\boldsymbol{S}$ is a completely quantum mechanical property of particles which has no classical analog. This quantum property is known to couple with a magnetic field, and for example, the spin of an electron gives rise to a magnetic moment $\boldsymbol{\mu} = -e/(mc)\boldsymbol{S}$. To incorporate the spin degree of freedom into the wavefunction, we introduce the spinor χ and write the composite wavefunction as $\Psi \equiv \Psi(r,t)\chi$. For example, if we consider a spin-$1/2$ particle which has its spin projected along a direction α in spin space, the spinor is $\chi = (\langle+|\alpha\rangle, \langle-|\alpha\rangle)^T$ where T denotes the transpose. This spinor is an ad-hoc modification to the Schrödinger equation intended to incorporate the discrete spin degree of freedom.

1.1.1 Dirac Equation

Soon after its introduction, many physicists worked on developing a relativistic generalization the Schrödinger equation. Motivated by the relativistic energy momentum relation $E^2 = \boldsymbol{p}^2c^2 + m^2c^4$, or in relativistic notation,

$$p^\mu p_\mu - mc^2 = 0 \tag{1.3}$$

where we have used Einstein summation rules and $\mu, \nu \in (0,1,2,3)$ [2]. A relativistic wave equation had already been developed by promoting the four momenta to operators by $p_\mu \mapsto i\hbar\partial_\mu$, where $\partial_\mu \equiv \partial/\partial x^\mu$. This process leads to a second order differential equation in space and time. The resulting Klein-Gordon equation reads $\hbar^2\partial^\mu\partial_\mu\psi - m^2c^2\psi = 0$. As it turns out, this equation had been discovered before the

Schrödinger equation but was rejected because it does not conserve probability in the presence of a uniform potential[3, 4]. However, a relativistic quantum field theory describes a field and not a single particle so the Klein-Gordon equation is now understood to describe relativistic spin-0 particles.

In order to obtain a first order differential wave equation Dirac attempted to factor the energy momentum relation Eq. 1.3. One can in fact factor this equation by $p^\mu p_\mu - mc^2 = (\beta_\kappa p_\kappa + mc)(\gamma^\lambda p_\lambda - mc)$ provided that the γ, β satisfy algebraic relations which lead to vanishing momenta cross terms. Dirac discovered that this is possible if the coefficients are not numbers but 4×4 matrices which satisfy the Clifford algebra $\{\gamma^\mu, \gamma^\nu\} = 2g^{\mu\nu}$ where $g^{\mu\nu} = diag(+1, -1, -1, -1)$ is the Minkowski metric and $\{A, B\} = AB + BA$ is the anticommutator[5, 2]. It turns out there are many sets of "gamma" matrices witch satisfy the specified algebra, with one common convention being

$$\gamma^0 = \begin{pmatrix} \mathbb{1} & 0 \\ 0 & -\mathbb{1} \end{pmatrix} \quad \gamma^i = \begin{pmatrix} 0 & \sigma^i \\ \sigma^i & 0 \end{pmatrix}$$

As in the case of the Klein-Gordon equation we promote the four momenta to operators ($p^\mu \mapsto -i\hbar\partial_\mu$) which now act on a four component spinor $\psi = (\psi_1, \psi_2, \psi_3, \psi_4)^T$ (note, the wavefunction is *not* a four-vector). The Dirac equation reads

$$i\hbar\gamma^\mu\partial_\mu\psi - mc\psi = 0. \tag{1.4}$$

In modern quantum field theory the Dirac equation (as well as an adjoint equation) can be derived from the Lagrangian density $\mathcal{L} = c\bar{\psi}(-i\hbar\gamma^\mu\partial_\mu - mc)\psi$ by the usual procedure leading to the Euler-Lagrange equations.

Interestingly, solutions to Eq. 1.5 come positive and negative pairs $\pm E$. The positive energies are associated with states of particles, while the negative ones are attributed to *anti-particles*. This prediction of antiparticles, Dirac's had reservations about this interoperation and argued that all negative energy solutions were filled and thus not observed, is one of the great triumphs of quantum mechanics. Also, note that while spin was incorporated into the the Schrödinger by the introduction of a spinor wavefunction, it arises naturally in the construction of the Dirac equation.

The positive energy solutions describe usual spin-half particles such as electrons. Dirac concluded the negative energy solutions correspond to anti-electrons, now called positrons, which were discovered soon after [6]. In Dirac's initial interpretation the charge neutral ground state we observe and call the vacuum

is really a 'Dirac sea', similar to the Fermi sea in condensed matter, and consists of negative energy levels filled by positrons. In this sense, the Dirac equation is a many particle equation, with individual particles populating the single particle energy levels[6].

1.1.2 Self-conjugate Fermions: The Majorana Representation

A few years later, Ettore Majorana found himself wondering if a complex representation was necessary for the Dirac equation. in 1938 he found the following representation of the gamma matrices where each of the γ^μ's are imaginary:

$$\gamma^0_M = \begin{pmatrix} 0 & \sigma^2 \\ \sigma^2 & 0 \end{pmatrix} \gamma^1_M = \begin{pmatrix} i\sigma^3 & 0 \\ 0 & i\sigma^3 \end{pmatrix} \gamma^2_M = \begin{pmatrix} 0 & \sigma^2 \\ -\sigma^2 & 0 \end{pmatrix} \gamma^3_M = \begin{pmatrix} -i\sigma^1 & 0 \\ 0 & -i\sigma^1 \end{pmatrix} .$$

which in turn makes the Eq. 1.5 a real differential equation. Therefore the fields can be real in the Majorana representation and the solutions satisfy the self-conjugate *Majorana relation* $\psi = \psi^\dagger$.

1.1.3 Fundamental Majorana Particles

In general, neutral particles which are their own antiparticles are quite common. For example, photons (γ) and the neutral pion (π^0) are both their own antiparticles. However these particles are bosons, so they are not subject to the Dirac equation. The most famous neutral particle is a neutron, is it a Majorana fermion? Fortunately for the stability of atoms and life, the neutron is not its own antiparticle, and the many neutrons which coexist in atomic nuclei are in no danger of self-annihilating. The reason for this is that neutrons are Baryons which are composite particles made up of quarks. A neutron (n^0) is composed of one up quark and two down quarks, giving it a total baryon number of $B_q = 1/3(n_q + n_{\bar{q}}) = +1$. Since, quarks ($u$) are distinct from anti-quarks ($\bar{u}$) the neutron is still described by a complex field.

The next obvious candidate, due to its presumed charge neutrality, for Majorana fermions was the neutrino (ν). Neutrinos were discovered in 1956 at the Savannah River National Laboratory[7]. However, while neutrinos always have left-handed chirality while anti-neutrinos ($\bar{\nu}$) always have right handed chirality. This initially implies that $\nu, \bar{\nu}$ are distinct particles. However, in principle chirality depends on ones reference frame and neutrino-less double beta decay, such as the process $Ge_{76} \rightarrow Se_{76} + 2e$, is currently the subject of intense research[8].

1.1.4 Zero-modes in a modified Dirac Equation

The Dirac equation has also found applications in the context of condensed matter physics when the low-energy dynamics is described by matrix equations with a linear momentum dependence. In condensed matter systems, the positive (negative) energy solutions correspond to conduction (valence) electrons, usually the electrons are really some modified quasiparticles, instead of fundamental electrons (positrons). Often, an constant mass term separates the positive and negative energy solutions by a $2|m|$ gap. In superconducting systems the constant mass is the energy gap due to cooper pair condensation and is related to the pair potential $m = \Delta$.

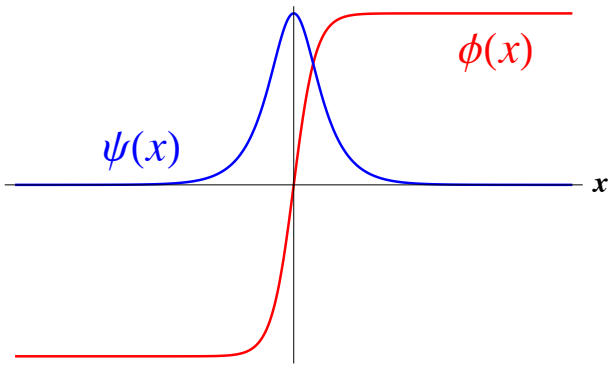

Figure 1.1: A spatially dependent mass term (red) $\phi(x) = tanh(z)$ with a sign flip at the origin. With this potential there exists a single zero energy mode, $\psi(x) = \exp\left[-(mc/\kappa)\int \phi(x')dx'\right]$ (blue) which is localized to the domain wall.

An interesting situation which we may occur is when the mass term is spatially dependent; that is, $m \to \phi(x)$. A 1D a mass flip between $\pm m$, illustrated in Fig. 1.1, is known as a mass kink leads leads to bound state solutions in addition to the $\pm E$ continuum states. The bound states localized about the kink are isolated at $E = 0$, falling within the mass gap. The mid-gap states can be found not only through an explicit solution of the differential equation 1.5 but also by mathematical index theorems which count the number of zero-modes in terms of the topological properties of the background $\phi(x)$. This raises a question of whether the mid-gap state is empty or occupied in the vacuum state? Also, what is its charge? In 1976 Jackiw and Rebbi [9] showed that the empty state carries charge $Q = -1/2$ and when it is filled $Q = 1/2$. This important result shows an example of a quantum system with a *fractional* eigenvalue. Fractional quantum numbers have since become ubiquitous in condensed matter physics with realizations in polyacetylene and the fractional

quantum Hall effect.

$$(\boldsymbol{\alpha} \cdot \boldsymbol{p} + \beta\phi(x))\Psi = i\hbar\frac{\partial}{\partial t}\Psi \tag{1.5}$$

The Jackiw-Rebbi model describes a one-dimensional relativistic particle (i.e. obeys the Dirac equation) coupled with a static soliton field (Alternatively, a Dirac particle under a Lorentz scalar potential). The scalar field in this model can be thought of as a position dependent mass term. Fig. 1.1 shows the real scalar potential $\phi(x) = tanh(z)$ whose amplitude changes sign across the origin. This potential leads to a single zero energy mode $\psi(x) = \exp\left[-(mc/\kappa)\int \phi(x')dx'\right] = exp\left[-(mc)\ln\cosh(z)\right]$ which is pinned to the domain wall. Later in this work we how this model is realized in Josephson junctions constructed from two topological superconductors and held a phase difference $\phi = \pi$. This model is at the heart of the 4π periodicity Josephson effect.

1.2 Topological quantum computation

An extraordinary consequence of quantum theory is that information itself is fundamentally quantum mechanical. Classically, the fundamental unit of information is a bit: a single digit represented as either a 0 or 1. Today's digital information is usually physically encoded as voltages on a circuit or magnetic domains on an optical disc In contrast, *qubits* (short for quantum bits) are subject to the principle of quantum superposition, and are a linear superpositions of the 0 and 1 states simultaneously. An array of qubits on which logic operations are performed, and the result of a calculation is read out, is called a quantum computer. Due to the massive parallel processing power endowed by quantum superposition, these computers can potentially carry out select computational tasks which are impossible for the world's most powerful supercomputers (or any conceivable classical computer). In addition to simulation of complex physical, chemical, and biological phenomena (such as protein folding molecular dynamics), quantum computers would revolutionize digital security by rendering conventional public-key cryptography algorithms useless.

Despite the unprecedented success of quantum theory, manipulating quantum systems while coherently preserving encoded information still poses a formidable challenge. The interference process by which quantum information is spoiled, when a *target* system (the system of interest) interacts with a surrounding environment, is called *decoherence*. Given the tremendous technological and scientific implications of quantum computation, the reduction of quantum decoherence is of paramount importance. Significant progress

recently been made made, for example some single qubits (i.e. isolated systems not interacting with other qubits) have reached fidelities of over 99 % and in some cases the coherence times are approaching the microsecond range (a very long time for a quantum object).

In contrast to most error correction schemes, topological quantum computation provides an alternative approach which is fundamentally decoherence free. The important idea is to encode information in non-local quantum state, so as to hide them from coupling with the environment which is generically a local process. We shall now introduce the process of quantum computation, paying special attention to quantum logic operations. Afterwards we discuss how quantum information which is encoded in topological quantum degrees of freedom, specifically using Majorana bound states, can be used to construct intrinsically fault-tolerant quantum logic gates simply by manipulating the spatial positions of quasiparticles.

1.2.1 Principles of quantum computation

The process of quantum computation consists of three steps. First, qubits are initialized into a predetermined state. For example, the initial configuration of two qubits could be the pure state $|0,0\rangle$. Following Initialization, one must apply quantum logic operations to the qubits. The series of logical operations depends on the specific quantum algorithm which is being implemented. Finally the information is read out by physically measuring some observable quantity which results in a classical bit. In the context of this thesis, we shall mainly discuss with the middle step, specifically we will address the basics of how quantum logic operations may be performed by physically braiding quasiparticles in topological ordered non-Abelian phases of matter.

In classical information theory, the bit is an abstract mathematical quantity which may take a value of 0 or 1. Computation is the manipulation of bits through the use of logic gates – for example OR, NOT, AND, NAND gates – to implement an algorithm. Examples of physical implementations of bits include voltages on semiconducting transistors, magnetic domains or light in optical cables. The quantum mechanical analog of the bit is the quantum bit, or qubit. This abstract quantity is the fundamental unit of quantum information theory.

In principle any quantum mechanical two state system can be used as a qubit. For example, we could use the two spin states of an electron, the location of an electron in a double well potential (or quantum dots), or the direction of supercurrent in a superconducting ring. A qubit is usually represented in terms of two quantum states $|0\rangle, |1\rangle$. These pure quantum states are usually taken to be the computational basis states, analogous to the role of 0 and 1 in classical computing. However, while classical bits are restricted to the

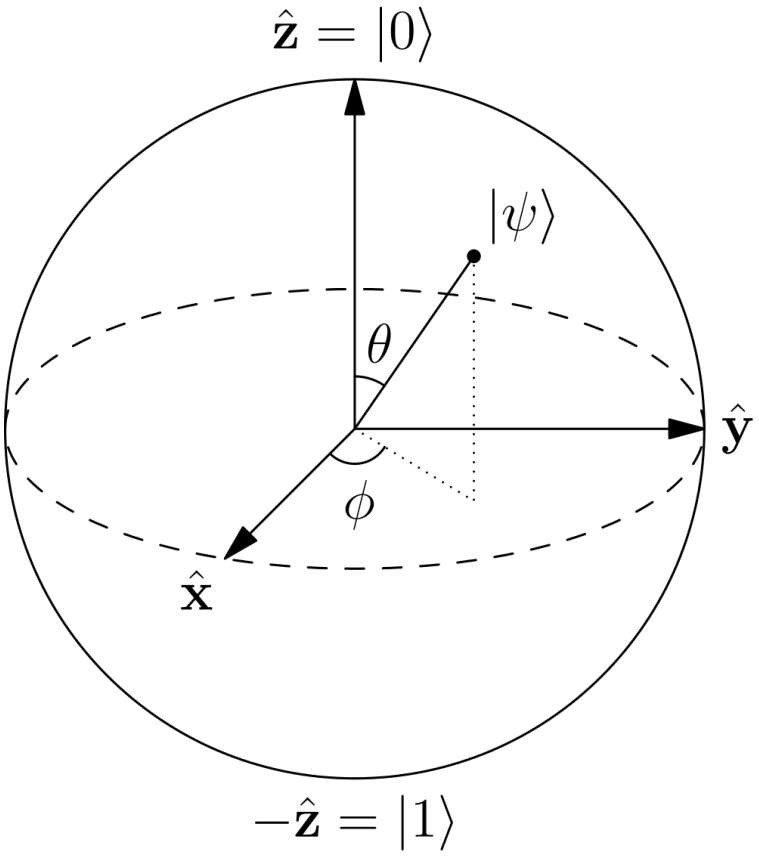

Figure 1.2: The state of a two level quantum system is represented by a unit vector on the Bloch sphere. Any controllable two level quantum system can be used as a qubit.

values $0, 1$, a qubit may be any complex linear superposition of $|0\rangle, |1\rangle$ and the general state $|\psi\rangle$ is represented as a vector in a two-dimensional complex vector space

$$|\psi\rangle = \alpha|0\rangle + \beta|1\rangle. \tag{1.6}$$

Here the coefficients $\alpha, \beta \in \mathbb{C}$ are complex numbers subject to the constraint $|\alpha|^2 + |\beta|^2 = 1$ which normalizes $|\psi\rangle$ to unit length. The coefficients α, β can be paramterized by the angles θ, ϕ as illustrated in Fig. 1.3 by the Bloch sphere. The north and south poles of the Bloch sphere are the pure states $|0\rangle, |1\rangle$.

1.2.2 Quantum Logic gates

Let us first consider an example of a single qubit quantum logic gate in order to later understand more operators. First consider the NOT gate denoted by X. This action of this logical operation is to interchange the computational basis states:

$$\begin{aligned} |0\rangle &\rightarrow |1\rangle \\ |1\rangle &\rightarrow |0\rangle \\ \alpha|0\rangle + \beta|1\rangle &\rightarrow \alpha|1\rangle + \beta|0\rangle. \end{aligned} \tag{1.7}$$

X can also be written in matrix form as the first Pauli matrix σ_x and is known as the Pauli-X gate. Likewise there are also Pauli-Y, Z gates which are simply rotations of the Bloch sphere (Fig. 1.3). Obviously the action of two Pauli-types gates in series is the identity operation since $\sigma_i^2 = \mathbb{1}$.

Let us also consider a quantum gate with no classical analog, that is, the Hadamard gate. The action on the basis states and a general superposition between them by H is:

$$\begin{aligned} |0\rangle &\rightarrow \frac{|0\rangle + |1\rangle}{\sqrt{2}} \\ |1\rangle &\rightarrow \frac{|0\rangle - |1\rangle}{\sqrt{2}} \\ \alpha|0\rangle + \beta|1\rangle &\rightarrow \frac{\alpha+\beta}{\sqrt{2}}|0\rangle + \frac{\alpha-\beta}{\sqrt{2}}|1\rangle. \end{aligned} \tag{1.8}$$

This is algebraically we write $H = 1/\sqrt{2}(\sigma_x + \sigma_z)$. The Hadamard gate is quantum mechanical in the sense that the action on classical basis states is a quantum superposition of basis states.

In general, any quantum gate can be represented by a unitary matrix U. Remember that unitary matrices obey $U^\dagger = U^{-1}$ and preserve length, that is, $||U|\psi\rangle|| = |||\psi\rangle||$ where $||v||$ denotes the length of the vector v.

In classical information theory any logic operation can be constructed by a composition of AND and NOT gates. One can then build any computing devise solely from these gates. It may not be an efficient computer, but it will work. Again, this means logic operation such as the OR gate or arithmetic operations like addition can be constructed from this set of two gates. The AND and NOT gates are therefore *universal* for classical computation. Other universal gate sets exist with one example being just the NAND gate.

In the case of quantum computation, one simple universal gate set is the CNOT gate combined with

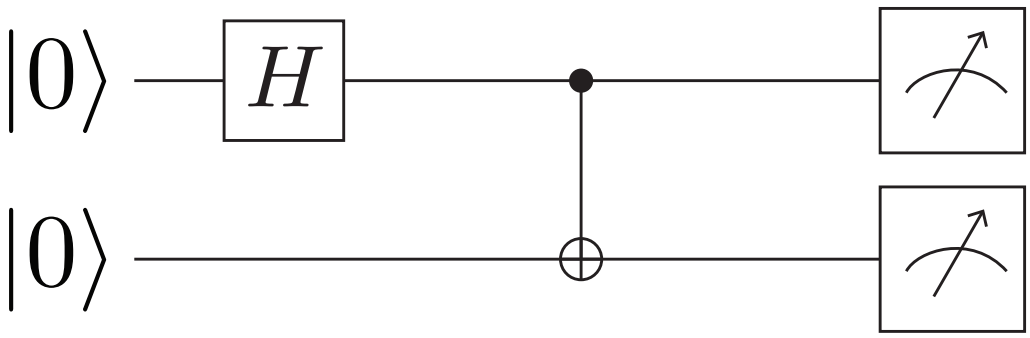

Figure 1.3: A simple two qubit quantum circuit involving Hadamard and controlled-NOT gates in series followed by a measurement operation on both qubits.

arbitrary control of a single-qubit. With this set of operations one may build up any unitary operation on the set of n qubits.

1.3 Non-Abelian anyons and topological phases of matter

A real life topological phase of matter will be necessary to implement an intrinsically fault tolerant quantum computer. A topological phase of matter is a physical system which is described by a topological quantum field theory [10]. In the presence of quasiparticle excitations, a highly degenerate ground state manifold is characteristic of a topological phase of matter. Topological states of matter are immune to most types of decoherence due to the topological nature of the ground state manifold. One important property of a topological phase, with a ground state degeneracy, is that no local operator may transform the many body ground state wavefunction into another ground state wavefunction. Note that by local we are referring to operation on the state by an operator which is defined at a single point in spacetime. Since noise processes are in general local, topological state are virtually immune to errors. Indeed, only physically braiding quasiparticles induces dynamics within the degenerate ground state subspace.

In order to understand how a topological quantum computer operates let us first discuss quantum statistics. The indistinguishability of quantum particles of the same type is an axiom in quantum mechanics. For example, all electrons are *exactly* the same as all other electrons, likewise for quarks, neutrinos and any other particles appearing the in standard model. Because of this principle, no physical observable should

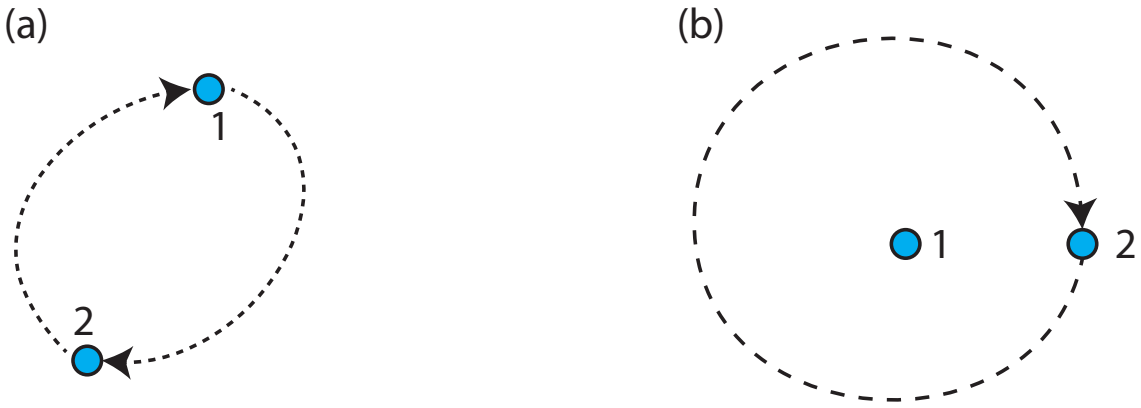

Figure 1.4: Panel (a) shows the operation $\hat{T}$ which swaps two particles. Panel (b) shows a braid which is topologically equivalent to two swaps, i.e. $\hat{T}^2$.

change under the exchange of two particles. In quantum mechanics, physical observables are related to the probability density $|\Psi|^2$. Therefore, by interchanging two particles the wavefunction may change, provided $|\Psi|^2$ remains invariant. The behavior of many-body wavefunctions under the interchange of two particles depends on the type of particle and is described by the quantum spin-statistics theorem.

Consider a generic N body wavefunction, which we denote by $\Psi \equiv \Psi(x_1, x_2, ..., x_N)$. First, we interchange particles 1 and 2 as seen in Fig. 1.4 panel (a) and we denote this operation by $\hat{T}$. The dashed lines and arrows depict the world lines of the particles and their direction during the exchange process. We write $\Psi(x_2, x_1, ..., x_N) = \hat{T}\Psi(x_1, x_2, ..., x_N)$ subject to the constraint $\hat{T}^\dagger\hat{T} = 1$ as enforced by the invariance of $|\Psi|^2$ under $\hat{T}$. For our purposes it will be useful to consider the effect of interchanging particles twice, an operation denoted by $\hat{T}^2$. The particle world lines for the double exchange process may be topologically deformed into a trivial world line for particle 1, while particle 2 encircles particle 1 before returning to its original position. This process is illustrated in Fig. 1.4 panel (b). In a three dimensional world, we may take the world line loop created by tracing the trajectory of the second particle out of the plane and deform it to a trivial loop. Thus, the double exchange operation is trivial and we write $\hat{T}^2 = 1$. Since the double exchange is just the identity operator there are two possibilities where $\hat{T} = \pm 1$. In the case that $\hat{T} = 1$ we have $\Psi(x_2, x_1, ..., x_N) = \Psi(x_1, x_2, ..., x_N)$ which is familiar form of a symmetric bosonic wavefunction. Likewise, when $\hat{T} = -1$ yields a wavefunction antisymmetric under exchange $\Psi(x_2, x_1, ..., x_N) = -\Psi(x_1, x_2, ..., x_N)$ which describes fermions and is at the heart of the Pauli exclusion principle.

However, our preceding argument hinged on the fact that we were free to take the loop out of the

plane, defined by the original loop and particles, in order to deform the second particle's world line into a trivial loop. In a two dimensional system the loop cannot contract to a trivial loop without colliding with particle 1. Because of this fact, $\hat{T}$ need not square to unity and we are left with our original condition, i.e. that $\hat{T}^\dagger\hat{T} = 1$. This condition is obviously satisfied if $\hat{T}$ is simply a number on the complex unit circle. In this case the many body wavefunction would transform by $\Psi(x_2, x_1, ..., x_N) = e^{i\theta}\Psi(x_1, x_2, ..., x_N)$ which reduces to the familiar bosonic and fermionic conditions if $\theta = 0, \pi$ respectively. Particles obeying this kind of exchange statistics have been dubbed "Anyons" [11], since θ can in principle take any value, and are associated with fractionalized particles. Note that the phase θ is the result of a pairwise exchange of particles (independent of the exchange trajectory), however this does not imply the wavefunction is multi-valued and x_j simply refers to the position of a particle and the wavefunction is a continuous function of the single particle coordinates x_j. Famously, quasiparticle excitations with charge $q = e/3$ appearing the $\nu = 1/3$ fractional quantum Hall effect (FQHE), described by the Laughlin wavefunction[12], are anyons with $\theta = 2\pi/3$.

There exists yet an even more exciting possibility, with even stranger exchange statistics than simply a complex phase. The operator $\hat{T}$ may be unitary matrix relating two distinct, but locally identical, wavefunctions within a degenerate ground state manifold. That is, we could have $\Psi_i(x_2, x_1, ..., x_N) = \hat{T}_{ij}\Psi_j(x_1, x_2, ..., x_N)$ where the indices i, j label distinct ground states within a basis of degenerate states[10]. It turns out that this may actually be the case in certain states topological state of matter such as the $\nu = 5/2, 12/5$ FQHE and in low dimensional topological superconductors. For example, we shall see that in p-wave superconductors the excitations bound to defects, such as edges and vortices, are described by self-conjugate second quantized operators γ which can be regarded as half a conventional electronic degree of freedom, i.e. we shall see that $c = \gamma_1 + i\gamma_2$. As such, it takes $2n$ vortices to encode n electronic degrees of freedom. If there are 4 vortex bound quasipartilces we can define two zero energy electronic degrees of freedom c_a, c_b and the ground state subspace is spanned by the four orthogonal states $|00\rangle, |01\rangle, |10\rangle, |11\rangle$.

However low dimensional ($d = 2$) condensed matter systems provide a platform for unusual and exotic exchange statistics. Particles which are neither bosons nor fermions are called "anyons" as coined by Frank Wilzcek[11]. To understand anyons first consider an exchange operation, constrained to two dimensions, involving the braiding of one particle around another. This operation is topologically equivalent to exchanging two particles twice in a closed loop as shown in Fig. 1.4 panel (a). In this case, the world line of particle A cannot be contracted to a trivial loop since it must intersect the other particle, which is against the rules (we will not allow fusion of Majorana states or other vortex bound quasiparticles).

Let us briefly note that condensed matter physics provides a realistic setting for truly two-dimensional

physics. For example, a two-dimensional electron gas (2DEG) can be formed at the interface between two insulating semiconductors. In a 2DEG electrons are free to move in two dimensions (along the heterostructure interface) and are tightly bound in the normal direction. This tight confinement, along say $\hat{z}$-direction, leads to quantized transverse momentum $\langle k_z \rangle$. If the confinement is strong and the electron density and temperature all the electrons are confined to the lowest k_z subband and they system is effectively two dimensional. Furthermore, provided the electrons are mobile enough, a strong magnetic field can drive this system into a quantum hall state in which excited state are separated from the ground state by a finite energy gap.

As shown by Ivanov[13], braiding (i.e. adiabatically interchanging) two Majoranas, associated with the same electron operator, around one another transforms the state vector by

$$\Psi \mapsto \exp\left[i\frac{\pi}{4}\sigma_z\right]\Psi \tag{1.9}$$

where Ψ represents the two dimensional state vector *within the degenerate zero-energy subspace*. Thus, the adiabatic exchange of two MBSs constitutes a non-Abelian unitary transformation and the final state is not the same as the initial Ψ. In general, if there are $2n$ MBSs (whose operators $\gamma_i,\ i = 1, 2, ...2n$ commute with the Hamiltonian), bound to $2n$ vortices for example, one can combine them into n complex fermionic operators. Since each electronic state can be empty or occupied, the n complex fermion operators give rise to a degeneracy of $D = 2^n$. Under slow adiabatic braiding of the vortices (separated by a distance greater than $\xi_0 \sim v_F/\Delta$) transitions between the subgap states are forbidden, and the unitary evolution within the space of ground states occurs.

Pulling two sets of Majorana particle anti-particle pairs out of the vacuum will result in the initial state:

$$|\Psi_i\rangle = |00\rangle = \begin{pmatrix} 1 \\ 0 \\ 0 \\ 0 \end{pmatrix} \tag{1.10}$$

where we have used the basis $(|00\rangle, |01\rangle, |10\rangle, |11\rangle)$ in representing the initial state as a four component

spinor. Then by braiding particles 2,3 ,as shown by Ivanov, the state

$$|\Psi_f\rangle = M(\sigma_2)|\Psi_i\rangle = \frac{1}{\sqrt{2}}(|00\rangle + |11\rangle) = \begin{pmatrix} 1 \\ 0 \\ 0 \\ -i \end{pmatrix} \tag{1.11}$$

Also, consider the evolution of the electronic operators under a U(1) transformation to the superconducting order parameter $\Delta \mapsto \Delta e^{i\phi}$. Under such a transformation the electron and hole operators are modified by a phase factor $c \mapsto e^{i\phi/2}c, c^\dagger \mapsto e^{-i\phi/2}c^\dagger$. Note $\phi = 2\pi$ is a special case which takes all $c, c^\dagger \mapsto -c, -c^\dagger$. Using Eqs. 1.23,1.26 and we can see that the Majorana operators transform as $\gamma \mapsto -\gamma$ under a 2π winding of the superconducting phase.

In Fig. 1.4 we consider a two-dimensional space with two Majorana zero modes bound to vortices at positions x_1, x_2. Here the pair potential is taken to be a single valued function at all points in the two dimensional space, jumping by 2π across the branch cut indicated by the red dashed line in panel b).

1.4 Emergent Majorana fermions in superconductors

1.4.1 Historical Introduction and BCS Theory

Consider a system of electrons interacting by some spin-conserving potential. Using $c^\dagger(c)$ to represent electron creation (annihilation) operators, the momentum space Hamiltonian describing the interacting electron system is

$$H = \sum_{k,\sigma} c^\dagger_{k\sigma} c_{k\sigma} \epsilon_k + \sum_{k_1 k_2 k_3 k_4 \sigma\sigma'} U(k,q) c^\dagger_{k_1\sigma} c^\dagger_{k_2\sigma'} c_{k_3\sigma'} c_{k_4\sigma}. \tag{1.12}$$

Here, the first term describes the single particle kinetic energy, while the second describes interactions between electrons. In the BCS problem one considers the interaction to be momentum independent within a small shell (of width $2\hbar\omega_D$) around the Fermi surface, and attractive for electrons of opposite momentum and spin (i.e. $k\uparrow, -k\downarrow$). We write,

$$U_{kq} = \begin{cases} -U & \text{if } E_F - \hbar\omega_D \leq \epsilon_k, \epsilon_q \leq E_F + \hbar\omega_D \\ 0, & \text{otherwise} \end{cases} \tag{1.13}$$

These assumptions simplify Eq. 1.12 to [14]

$$H_{BCS} = \sum_{k,\sigma} c^\dagger_{k\sigma} c_{k\sigma} \epsilon_k - U \sum_{kq} c^\dagger_{k\uparrow} c^\dagger_{-k\downarrow} c_{-q\downarrow} c_{q\uparrow} \tag{1.14}$$

where the summation is taken within over a thin shell of width $\hbar\omega_D$ around the Fermi surface.

At this point the interaction term in the Hamiltonian is treated using a mean field approximation. We do this by expanding the two operators in interaction term in Eq. 1.14 about their expectation value. We write, $c^\dagger_{k\uparrow} c^\dagger_{-k\downarrow} = \langle c^\dagger_{k\uparrow} c^\dagger_{-k\downarrow} \rangle + (c^\dagger_{k\uparrow} c^\dagger_{-k\downarrow} - \langle c^\dagger_{k\uparrow} c^\dagger_{-k\downarrow} \rangle)$ and we only keep the term in brackets to first order. The resulting mean field Hamiltonian is

$$H_{BCS} = \sum_{k,\sigma} c^\dagger_{k\sigma} c_{k\sigma} \epsilon_k - U \sum_{kq} \left[\langle c^\dagger_{k\uparrow} c^\dagger_{-k\downarrow} \rangle c_{-q\downarrow} c_{q\uparrow} + \langle c_{-q\downarrow} c_{q\uparrow} \rangle c^\dagger_{k\uparrow} c^\dagger_{-k\downarrow} + \langle c^\dagger_{k\uparrow} c^\dagger_{-k\downarrow} \rangle \langle c_{-q\downarrow} c_{q\uparrow} \rangle \right] \tag{1.15}$$

Defining $U \sum_k \langle c^\dagger_{k\uparrow} c^\dagger_{-k\downarrow} \rangle \equiv \Delta$ this becomes

$$H_{BCS} = \sum_{k,\sigma} c^\dagger_{k\sigma} c_{k\sigma} \epsilon_k - U \sum_{k} \left[\Delta c_{-k\downarrow} c_{k\uparrow} + \Delta^* c^\dagger_{k\uparrow} c^\dagger_{-k\downarrow} \right] + |\Delta|^2 \tag{1.16}$$

where we shall ignore the last term since it only contributes a constant to the energy. Thus, using the mean field approximation we have reduced our Hamiltonian to a bilinear form in the creation and annihilation operators. As we shall see in the next section, such a Hamiltonian can always be diagonalized by a Bogoliubov-Valentin transformation which will have important implications for Majorana quasiparticle excitations.

1.4.2 Quasiparticle Excitations and Majorana Modes

By definition mean-field lattice Hamiltonians are quadratic in field operators $c_i, c_i^\dagger$ acting on site i. A typical superconducting Hamiltonian look like

$$H = \sum_{ij} \left(c^\dagger_{i\uparrow}, c^\dagger_{i\downarrow}, c_{i\uparrow}, c_{i\downarrow} \right) \begin{pmatrix} H_0^{\uparrow\uparrow} & H_0^{\uparrow\downarrow} & \Delta^{\uparrow\uparrow} & \Delta^{\uparrow\downarrow} \\ H_0^{\downarrow\uparrow} & H_0^{\downarrow\downarrow} & \Delta^{\downarrow\uparrow} & \Delta^{\downarrow\downarrow} \\ \Delta^{\uparrow\uparrow} & \Delta^{\uparrow\downarrow} & -H_0^{\uparrow\uparrow} & -H_0^{\uparrow\downarrow} \\ \Delta^{\downarrow\uparrow} & \Delta^{\downarrow\downarrow} & -H_0^{\downarrow\uparrow} & -H_0^{\downarrow\downarrow} \end{pmatrix} \begin{pmatrix} c_{j\uparrow} \\ c_{j\downarrow} \\ c^\dagger_{j\uparrow} \\ c^\dagger_{j\downarrow} \end{pmatrix} \tag{1.17}$$

If we use $\Psi_i = (c_{i\uparrow}, c_{i\downarrow}, c^\dagger_{i\downarrow}, -c^\dagger_{i\uparrow})^T$ as a four component spinor acting on site i, the Hamiltonian

becomes

$$H = \sum_{ij} \Psi_i^\dagger H_{ij} \Psi_j. \tag{1.18}$$

The property $H_{ji} = H_{ij}^*$ follows from the fact that H is a Hermitian matrix. Bogoliubov-de Gennes (BdG) Hamiltonians describe quasiparticle excitations above the BCS vacuum and are expressed in terms of (two or four component) Nambu spinors which mix particles and holes. In this work we use the time-reversed Nambu basis $\Psi_i = (c_{i\uparrow}, c_{i\downarrow}, c_{i\downarrow}^\dagger, -c_{i\uparrow}^\dagger)^T$. Here $c_{i\sigma}^\dagger, c_{i\sigma}$ are electronic creation and annihilation operators which obey the usual fermionic anti-commutation relations:

$$\begin{aligned} \left\{c_{i\sigma}, c_{j\sigma'}\right\} &= 0 \\ \left\{c_{i\sigma}^\dagger, c_{j\sigma'}^\dagger\right\} &= 0 \\ \left\{c_{i\sigma}, c_{j\sigma'}^\dagger\right\} &= \delta_{ij}\delta_{\sigma\sigma'}. \end{aligned} \tag{1.19}$$

BdG Hamiltonians contain off diagonal $c^\dagger c^\dagger$ terms. In momentum space we write $H = \sum_k \Psi_k^\dagger H(k) \Psi_k$. Explicitly, in terms of the four component spinor $\psi_k = (c_{k\uparrow}, c_{k\downarrow}, c_{-k\uparrow}^\dagger, -c_{-k\downarrow}^\dagger)^T$ the BdG Hamiltonian is:

$$H = \sum_k \left(c_{k\uparrow}^\dagger, c_{k\downarrow}^\dagger, c_{-k\uparrow}, c_{-k\downarrow}\right) \begin{pmatrix} H_0^{\uparrow\uparrow} & H_0^{\uparrow\downarrow} & \Delta^{\uparrow\uparrow} & \Delta^{\uparrow\downarrow} \\ H_0^{\downarrow\uparrow} & H_0^{\downarrow\downarrow} & \Delta^{\downarrow\uparrow} & \Delta^{\downarrow\downarrow} \\ \Delta^{\uparrow\uparrow} & \Delta^{\uparrow\downarrow} & -H_0^{\uparrow\uparrow} & -H_0^{\uparrow\downarrow} \\ \Delta^{\downarrow\uparrow} & \Delta^{\downarrow\downarrow} & -H_0^{\downarrow\uparrow} & -H_0^{\downarrow\downarrow} \end{pmatrix} \begin{pmatrix} c_{k\uparrow} \\ c_{k\downarrow} \\ c_{-k\uparrow}^\dagger \\ c_{-k\downarrow}^\dagger \end{pmatrix} \tag{1.20}$$

Note that single s-wave superconductivity is descried by $\Delta^{\uparrow\downarrow} = -\Delta^{\downarrow\uparrow} = \Delta_0$ (remember $|s=0\rangle = |\uparrow\downarrow\rangle - |\downarrow\uparrow\rangle$). In a matrix representation we would write the s-wave pair potential term as $H_\Delta = -\Delta_0 \tau_y \sigma_y$, where τ, σ act on the particle hole and spin degrees of freedom.

For convenience, we now transform to the time-reversed Nambu basis. The operator transforming to this basis is

$$U = \begin{pmatrix} \mathbb{1} & 0 \\ 0 & \Theta \end{pmatrix} \tag{1.21}$$

where $\Theta = i\sigma_y \mathcal{K}$ is the time reversal operator (remember this is an anti-unitary operator: $\Theta^\dagger \Theta = -i\sigma_y \mathcal{K} \cdot i\sigma_y \mathcal{K} = -\mathbb{1}$). This 'time-reversed' basis is a natural choice for superconductivity, where conventional s-wave Cooper pairs are bound states between time-reversed electrons. It also simplifies the notation for triplet pairing by simplifying the d-vector notation. Additionally, in this basis it is clear just by inspection which

terms break time revisal symmetry. Where finally in the Nambu spinor representation the BdG Hamiltonian appears as

$$H = \begin{pmatrix} H_0 & \Delta \\ \Delta^* & -\sigma_y H_0^* \sigma_y \end{pmatrix} \tag{1.22}$$

For example consider a Zeeman splitting term in the normal state described by $H_Z = \boldsymbol{V} \cdot \boldsymbol{\sigma}$. In this basis the Zeeman term in the (bottom right) hole sector of Eq. [5] becomes $H_Z \mapsto -\sigma_y(\boldsymbol{V} \cdot \boldsymbol{\sigma})^* \sigma_y = \boldsymbol{V} \cdot \boldsymbol{\sigma}$. Thus, while all time-reversal invariant terms in the normal state switch sign in the hole sector, time reversal breaking terms do not.

Therefore, a Bogoliubov-Valentin (BV) transformation is used rotate the Hamiltonian into a diagonal form $H = E_0 + \sum_n E_n \Gamma_n^\dagger \Gamma_n$. The nth excited quasiparticle creation operator is explicitly written in terms of electronic operators as

$$\Gamma_n^\dagger = \sum_{i\sigma} \left(u_{n\sigma i} c_{i\sigma} + v_{n\sigma i} c_{i\sigma}^\dagger \right) \tag{1.23}$$

where u, v are the matrix elements of a unitary transformation matrix which preserves the algebraic structure of the operators. The BV operators must satisfy $\left[H, \Gamma_n^\dagger\right] = E_n \Gamma_n^\dagger$ and this relation is typically used to determine the coefficients u, v. For fermionic systems in general we may say – in more mathematical language – that the BV transformation is a unitary transformation from a unitary representation of some canonical anti-commutation relation algebra into another unitary representation, induced by an isomorphism of the anti-commutation relation algebra.

Particles and holes are treated on equal footing in a superconductor, since charge is only conserved modulus 2. This fact is apparent in Eq. 1.23 in which the BV quasiparticle operators are a linear combination of electron and hole operators. In other words, an electronic excitation is the same as a partner hole excitation with an additional Cooper pair. This particle-hole symmetry can be expressed in terms of quasiparticle creation and annihilation operators by $\Gamma^\dagger(E) = \Gamma(-E)$. Indeed, this indistinguishability between electrons and holes makes superconductors natural hosts for self-conjugate Majorana excitations. Not that the particle and anti-particle states coincide at the Fermi energy $E = 0$, i.e. $\Gamma^\dagger(0) = \Gamma(0)$. Caroli, de-Gennes and Matricon showed that the energies of bound states in Abrikosov vortices, like the more familiar quantum harmonic oscillator, are $E_n = (n + 1/2)\hbar\omega$[15, 13] where in this case the level spacing is $\hbar\omega \approx \Delta^2/E_F$ (see Fig. 1.5). Thus, in s-wave vortices the zero point energy is responsible for preventing perfectly zero energy modes. What is therefore needed to realize MBSs, is a topological Berry phase, in addition to the familiar Berry phase associated with spin-1/2 fermions, to cancel out the zero point energy[16].

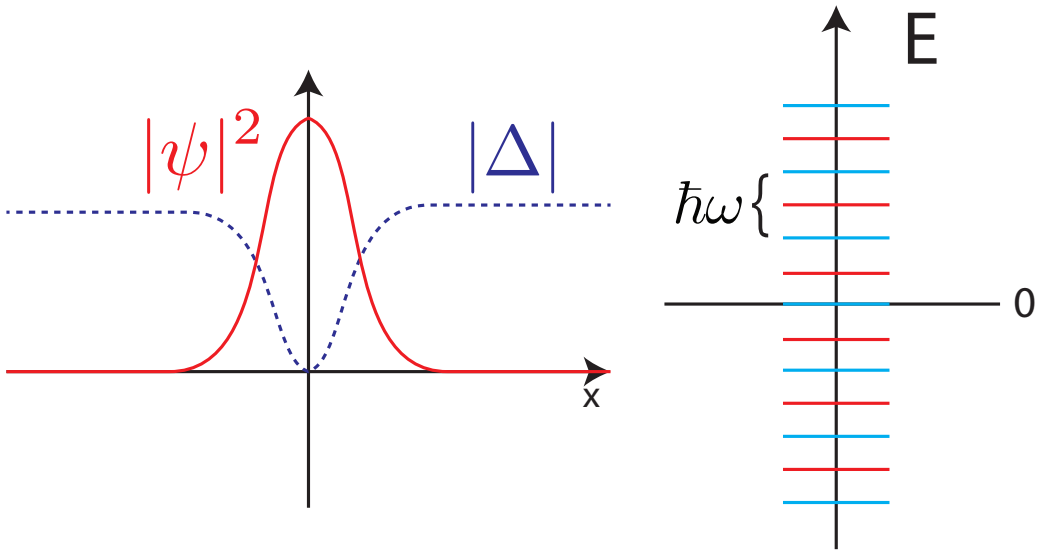

Figure 1.5: Panel (a): Probability amplitude of a Bogoliubov quasiparticle (red line) bound to a defect in the order parameter (dashed blue). Panel (b): Caroli, de-Gennes, Matricon energy levels for defect bound quasiparticles in a s-wave superconductor (red) and vortex bound energies in a topological p-wave superconductor (light blue).

Suppose a gapped system does not host zero energy Majorana modes. The closing of the energy gap (usually at $k = 0$ in the bulk) and subsequent reopening of the gap leaving a pair of zero-energy modes behind is called a topological quantum phase transition. The first phase, i.e. the one with no topological modes, is a topologically trivial phase indexed by a trivial topological invariant. The second phase, in which Majorana modes exist, is called topologically non-trivial.

1.4.3 Kitaev's Decomposition Argument

Let us begin with Kitaev's model for a one-dimensional spinless p-wave superconductor. We write

$$H = \sum_i -t(c_i^\dagger c_{i+1} + c_{i+1}^\dagger c_i) - \mu c_i^\dagger c_i + \Delta c_i^\dagger c_{i+1}^\dagger + \Delta^* c_{i+1}^\dagger c_i^\dagger \tag{1.24}$$

To illustrate how Majorana fermions can emerge in superconducting systems, Kitaev decomposes the complex electron operators at each site into their real and imaginary parts (note we switch notation and

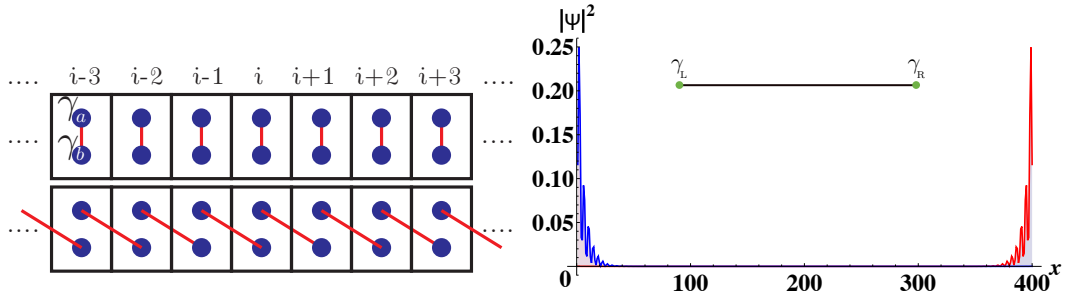

Figure 1.6: a) The electron operators on each site may be decomposed into their real and imaginary parts, each of which is described by a Majorana operator. Eq. 1.25 Kitaev shows the Hamiltonian (for specific parameters) can be written in terms of Majoranas coupled from the same site, or adjacent sites. b) The leftover Majorana operators come from the two ends of the wire and leak into the bulk for generic parameters values.

where γ indicates a real operator, and suppress cite and spin indices for now)

$$\begin{aligned} c &= \gamma_1 + i\gamma_2 \\ c^\dagger &= \gamma_1 - i\gamma_2. \end{aligned} \tag{1.25}$$

Writing the real operators in terms of the electron operators,

$$\begin{aligned} \gamma_1 &= c + c^\dagger \\ \gamma_2 &= (c - c^\dagger)/i \end{aligned} \tag{1.26}$$

it is clear that $\gamma_{1,2}$ are self-conjugate, i.e. $\gamma_a^\dagger = \gamma_a$ for $a = 1, 2$. While the (real) Majorana operators were constructed from fermionic operators, their commutation relations form a Clifford algebra

$$\{\gamma_a, \gamma_b\} = 2\delta_{ab}. \tag{1.27}$$

This is the first hint that Majorana fermions are not actually fermions at all, instead they are non-Abelian anyons. Note that, aside from some pre-factors, Eq. 1.23 becomes Eq. 1.26 in the special case when $u_i = v_i^*, v_i = u_i^*$. The quasiparticle parity $N = c^\dagger c = 1 + \gamma_1\gamma_2$ requires a joint measurement on both Majorana operators. Thus, information concerning the parity is locally obfuscated in the event that the Majorana operators are spatially separated, and this fact is at the heart of topological protection.

Chapter 2

Topological thermoelectric effects in spin-orbit coupled electron and hole doped semiconductors

Recently it has been shown that a 2D electron-doped semiconductor with Rashba type spin-orbit coupling in proximity to a bulk s-wave superconductor and an externally induced perpendicular Zeeman splitting can support a topological superconducting phase with Majorana fermion modes at vortex cores and sample edges [17, 18, 19]. The proposal followed on an earlier similar proposal for topological superconducting states using spin-orbit coupling and Zeeman fields made in the context of cold fermions. [20, 21]. It has also been pointed out by Alicea [22] that in the presence of Dresselhaus spin-orbit coupling co-existing along with the usual Rashba coupling, the topological superconducting state in electron-doped semiconductors can be realized with an in-plane Zeeman field. Since the in-plane Zeeman field can be directly applied by an in-plane magnetic field which is free of the orbital effects, the geometry proposed by Alicea is useful for producing topological superconductivity in two-dimensional electron systems. Very recently it has also been shown [23] that the generic Luttinger Hamiltonian applicable to the hole-doped semiconductors also supports topological superconductivity and Majorana fermions in the presence of a perpendicular Zeeman field in a manner similar to its electron-doped counterpart. The possibility of a larger value of the effective mass and spin-orbit coupling in p-type holes in a semiconductor quantum well makes the hole-doped systems an attractive candidate for realizing topological superconductivity that breaks time-reversal symmetry. The

strategy of producing topological superconductivity and Majorana fermions using Rashba spin-orbit coupling, parallel Zeeman field, and s-wave superconductivity has also been applied to electron- and hole-doped one dimensional semiconducting wires [19, 24, 25, 26]. The one dimensional topological systems are particularly useful for constructing quasi-two-dimensional quantum wire networks [27] which can potentially be used [27, 28, 29] as platforms for non-Abelian statistics [30, 31, 13, 32] and universal quantum computation [33, 10] in the Bravyi-Kitaev scheme[34]. For the purpose of studying anomalous topological transverse response functions such as anomalous Hall and Nernst effects, in this paper we will confine ourselves to two-dimensional hole- and electron-doped semiconductor thin films.

The substantive difference between the topological states in the electron and hole doped semiconductors lies in the fact that while the superconducting order parameter in the former is similar to the chiral p-wave ($p_x + ip_y$) type, the order parameter in the hole-doped system in a perpendicular Zeeman field is predominantly chiral f-wave ($f_x + if_y$) type [23]. A strong perpendicular Zeeman field, however, is difficult to realize experimentally with a magnetic field because of the unwanted orbital effects which are pair breaking[22]. Following Ref. 22, in this paper we will introduce the geometry and Hamiltonian for the hole-doped systems which can support topological superconductivity in the presence of an in-plane Zeeman field making it easier to produce with a magnetic field. We will then analyze the Berry phase mediated topological Hall and thermoelectric effects in electron- and hole-doped systems under external conditions necessary for realizing topological superconductivity with broken time-reversal symmetry. Note that, since we are considering the spontaneous or anomalous components of the Hall and Nernst effects, we will only treat two-dimensional systems in the presence of an *in-plane* Zeeman splitting.

In all the systems mentioned above the chemical potential regime that corresponds to the topological state in the presence of proximity effect is characterized by a single (or odd number of) Fermi surface which breaks the fermion doubling theorem[35]. It has been argued that, in the limit of vanishing superconducting pair potential Δ_0, the single (or odd number) of Fermi surface at the chemical potential constitutes a necessary condition for the existence of topological superconductivity and Majorana fermions at order parameter defects [36]. The breakdown of the fermion doubling theorem and topological superconductivity in all the above cases are achieved by the introduction of a strong Zeeman splitting greater than at least the proximity induced superconducting pair potential Δ_0. At such high values of the Zeeman splitting the superconductivity itself survives because of the spin-chirality induced on the semiconductor Fermi surface by a strong enough spin-orbit coupling[19].

The twin requirements of strong Zeeman splitting as well as spin-orbit coupling on the semicon-

ductor Fermi surface manifest themselves in interesting Berry phase[37] mediated topological effects which have pronounced effects on the anomalous Hall and thermoelectric coefficients [38, 39, 40, 41, 42, 43, 44, 45, 46, 47, 48, 49, 50, 51, 52, 53]. While these effects have been investigated previously, our focus in this paper is near the chemical potential regime - called topological regime hereafter - which supports topological superconductivity in the presence of s-wave proximity effect. We find that the topological regimes in both electron- and hole-doped semiconductors are marked by well-defined plateaus in the anomalous Hall and Nernst effects as a function of the chemical potential. The plateaus are not quantized, however, in the sense of quantized anomalous transport coefficients, because, even in the topological regime, the electron or the hole-doped systems are not fully gapped. Rather, in this regime of chemical potential they have a single (or odd number of) Fermi surface which supports, in the presence of spin-chirality induced by the spin-orbit coupling, the superconducting proximity effect. Even so, in the topological regime, there is a clear separation in the momentum space between the region where the Berry curvature is peaked (near the 'band-degeneracy' points in the absence of the Zeeman splitting) and the region where the Fermi surface lies in the Brillouin zone. Since the Nernst effect is strictly a Fermi surface quantity at zero temperature, the vanishing of the overlapping region in the Brillouin zone between the Fermi surface and the Berry curvature results in a vanishing anomalous Nernst effect in the topological regime. The plateau in the Nernst coefficient at vanishing magnitudes is flanked on either side of the topological regime by well-defined peaks (of opposite signs) arising from the emergence of a second small Fermi surface which destroys topological superconductivity but gives rise to large peaks in the topological Nernst effect. The results presented in this paper may be useful for experimentally deducing the topological regimes of the chemical potential in electron and hole-doped semiconductors supporting Majorana fermions in the presence of proximity effect.

2.1 Berry phase and topological Hall and Nernst effects

As a particle moves adiabatically through a closed contour in its parameter space it acquires a geometric phase known as a Berry phase. In a crystal lattice the wavefunctions for a band are written as $|\Psi_n(\boldsymbol{k},\boldsymbol{r})\rangle = e^{i\boldsymbol{k}\cdot\boldsymbol{r}}\,|u_n(\boldsymbol{k},\boldsymbol{r})\rangle$ according to Bloch's theorem where $|u_n(\boldsymbol{k},\boldsymbol{r})\rangle$ is a Bloch function with the periodicity of the lattice. The eigenfucntions are k dependent and the relevant paramater space is the space defined by the crystal momentum **k**. The Berry connection, $\boldsymbol{A_k} = \langle u_n(\boldsymbol{k},\boldsymbol{r})\,|i\nabla_{\boldsymbol{k}}|\,u_n(\boldsymbol{k},\boldsymbol{r})\rangle$ represents the geometric phase acquired by a Bloch wave function through infinitesimal movement in k-space and is a vector potential. In analogy to electrodynamics the Berry curvature is defined as the curl of this potential as

$\boldsymbol{\Omega}_n(\boldsymbol{k}) = \nabla_{\boldsymbol{k}} \times \boldsymbol{A}_{\boldsymbol{k}}$ which is Berry phase per unit area. The Berry curvature enters into the equations of motion of a wavepacket and is responsible for many intrinsic transport properties. For a system with time reversal symmetry and spatial inversion symmetry the Berry curvature vanishes for all **k** so it is often ignored.

The charge current in the presence of an electric field **E** and a temperature gradient ∇T can be written as $J_i = \sigma_{ij}E_j + \alpha_{ij}(\partial_j T)$ where σ_{ij} and α_{ij} are the electric and thermoelectric conductivity tensors. In the Hall effect a current is applied and a magnetic field is present perpendicular to a conducting sample. In this configuration an electric field is generated perpendicular to the current so that off diagonal terms of σ_{ij} are non-zero. Similarly for the Nernst effect a current will arise normal to the temperature gradient when a perpendicular magnetic field is present. Below we discuss the anomalous or topological Hall and Nernst effects for a system where there is no perpendicular magnetic field but there is still a contribution to the Hall and Nernst effects due to the presence of a non-trivial Berry curvature.

In the presence of an electric field **E**, the group velocity of a Bloch electron is written as [39]

$$\dot{\boldsymbol{r}} = \frac{1}{\hbar}\frac{\partial \epsilon_n(\boldsymbol{k})}{\partial \boldsymbol{k}} + \frac{e}{\hbar}\mathbf{E} \times \boldsymbol{\Omega}_{\mathbf{n}}(\mathbf{k}) \tag{2.1}$$

where the first term is the usual band dispersion and the second term is called the anomalous velocity. This anomalous velocity is responsible for the intrinsic contribution to the anomalous Hall and anomalous Nernst effects, with the Berry curvature acting like a magnetic field in k-space. With the inclusion of the anomalous velocity it immediately follows that by summing the anomalous velocity over all occupied states the charge conductivity is written as,[42, 43]

$$\sigma_{xy} = \frac{e^2}{\hbar}\sum_n \int \frac{dk_x dk_y}{(2\pi)^2}\Omega_n(\boldsymbol{k}) f(E_n(\boldsymbol{k})) \tag{2.2}$$

where $f(E_n) = 1/(1 + \exp(E_n - \mu)/k_B T)$ is the Fermi distribution function, k_B is the Boltzmann constant and T is the temperature.

In order to write an expression for the anomalous Nernst coefficient we first look at the coefficient $\bar{\alpha}_{xy}$ which relates the heat current and electric field by $J_x^h = \bar{\alpha}_{xy}E_y$. α_{xy} can then be solved for by making use of the Onsager relation $\bar{\alpha}_{xy} = T\alpha_{xy}$. The transverse heat coefficient may be written as the velocity multiplied by the entropy density,

$$\bar{\alpha}_{xy} = T\alpha_{xy} = \frac{e}{\beta\hbar}\sum_n \int \frac{dk_x dk_y}{(2\pi)^2}\Omega_n s_n(k), \tag{2.3}$$

where the entropy density of an electron gas is given as $s(k) = -f_k \ln f_k - (1-f_k)\ln(1-f_k)$ with f_k as the Fermi distribution function. Using the above equation and this form for the entropy density, the coefficient α_{xy} may be re-written as:[42, 43]

$$\begin{aligned} \alpha_{xy} &= \frac{e}{\hbar}\frac{1}{T}\sum_n \int \frac{dk_x dk_y}{(2\pi)^2}\Omega_n \times \\ &\{E_n(\boldsymbol{k}) f(E_n(\boldsymbol{k})) - k_B T \log[1 - f(E_n(\boldsymbol{k}))]\}\,. \end{aligned} \tag{2.4}$$

Through the use of these Berry phase mediated thermoelectric effects one can characterize the topological regimes in chemical potentials which support the topological superconducting state in the presence of superconducting proximity effect. We will deliberately choose quantum well configurations with appropriate spin-orbit couplings which will allow an in-plane Zeeman field for the topological state so the conventional Hall and thermoelectric effects make no contributions in experiments.

2.2 Topological Hall and Nernst effects in electron doped semiconductors

As a warm-up, following Alicea, [22] we first consider a zinc-blend semiconductor quantum well grown in the [110] direction with an in-plane magnetic field applied parallel to the semiconductor film. In such a quantum well we expect both Rashba and Dresselhaus spin orbit couplings to be present and the Hamiltonian of this system on the $(x-y)$ plane is written as, [22]

$$H = \frac{\hbar^2 k^2}{2m^*} + \alpha_R(\boldsymbol{\sigma} \times \boldsymbol{k}) \cdot \hat{z} + \alpha_D k_x \sigma_z + h_y \sigma_y \tag{2.5}$$

Here, α_R and α_D are the strengths of the Rashba and Dresselhaus couplings, m^* is the effective mass of the electrons, h_y the magnitude of the in-plane Zeeman field and the $\boldsymbol{\sigma} = (\sigma_x, \sigma_y, \sigma_z)$ are the Pauli matrices. Diagonalizing the Hamiltonian yields energy eigenvalues of $E_\pm = \frac{h^2 k^2}{2m^*} + E_0$, where $E_0 = \sqrt{(\alpha_D k_x)^2 + (\alpha_R k_y)^2 + (\alpha_R k_x - h_y)^2}$. The degeneracy between the two bands is lifted by the presence of both Dresselhaus spin orbit coupling and the in-plane magnetic field. It is easy to see that, in the absence of the Dresselhaus coupling, the in-plane Zeeman splitting can be reabsorbed in the Hamiltonian by a re-definition of the momentum $\alpha_R k_x \rightarrow \alpha_R k_x + h_y$ which leaves the system gapless even with the Zeeman

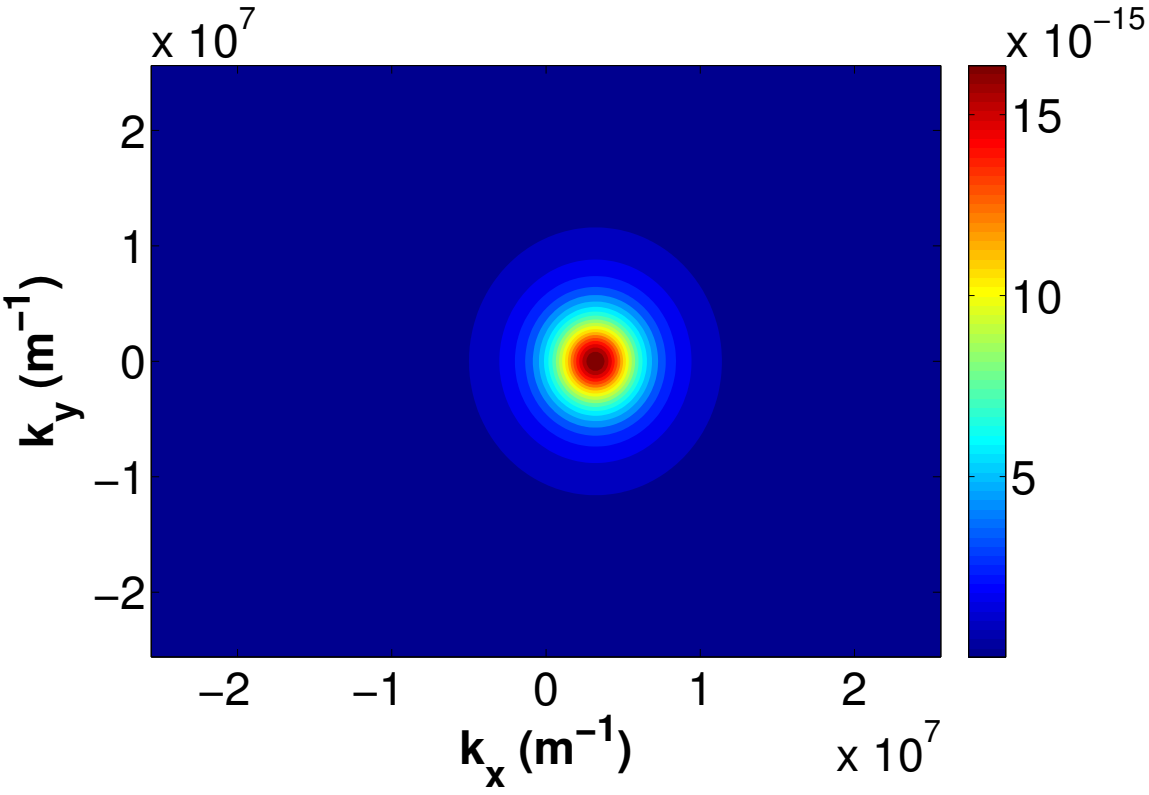

Figure 2.1: Contour plot of the Berry curvature $\mathbf{\Omega}_-$ in the lower band of electron-doped semiconductors. The Berry curvature is sharply peaked at a finite value of k_x near the band-degeneracy point in the absence of the Dresselhaus coupling.

splitting. The existence of a non-zero Dresselhaus term α_D ensures that a finite gap is created near the band-degeneracy points at a non-zero value of k_x even after this re-definition. The minimum gap between the bands, $\Delta = 2\alpha_D h_y/\sqrt{\alpha_R^2 + \alpha_D^2}$, is located at $k_x = \alpha_R h_y/(\alpha_R^2 + \alpha_D^2)$ and $k_y = 0$, [53] which is shown in the inset of figure 2.2.

We calculate the Berry curvatures for this system through $\mathbf{\Omega}_\pm = 2\mathrm{Im}\left\langle \frac{\partial \Phi_\pm}{\partial k_x} \middle| \frac{\partial \Phi_\pm}{\partial k_y} \right\rangle \hat{z}$, where $\Phi\pm$ are the eigenstates of the Hamiltonian in Eq. (2.5). Evaluating this expression analytically we find that[53]

$$\mathbf{\Omega}_\pm = \mp \frac{\alpha_R \alpha_D h_y}{2E_0^3} \hat{z}, \tag{2.6}$$

which are of equal magnitude and opposite signs in the two bands. In Fig. 2.1 we plot $\mathbf{\Omega}_-$ where it can be seen that the Berry curvature is sharply peaked at the gap minimum between the two bands, i.e., at the band degeneracy point in k-space in the absence of the Dresselhaus coupling. We note here that the Berry curvatures are only non-zero for non-zero values of α_D, α_R and h_y.

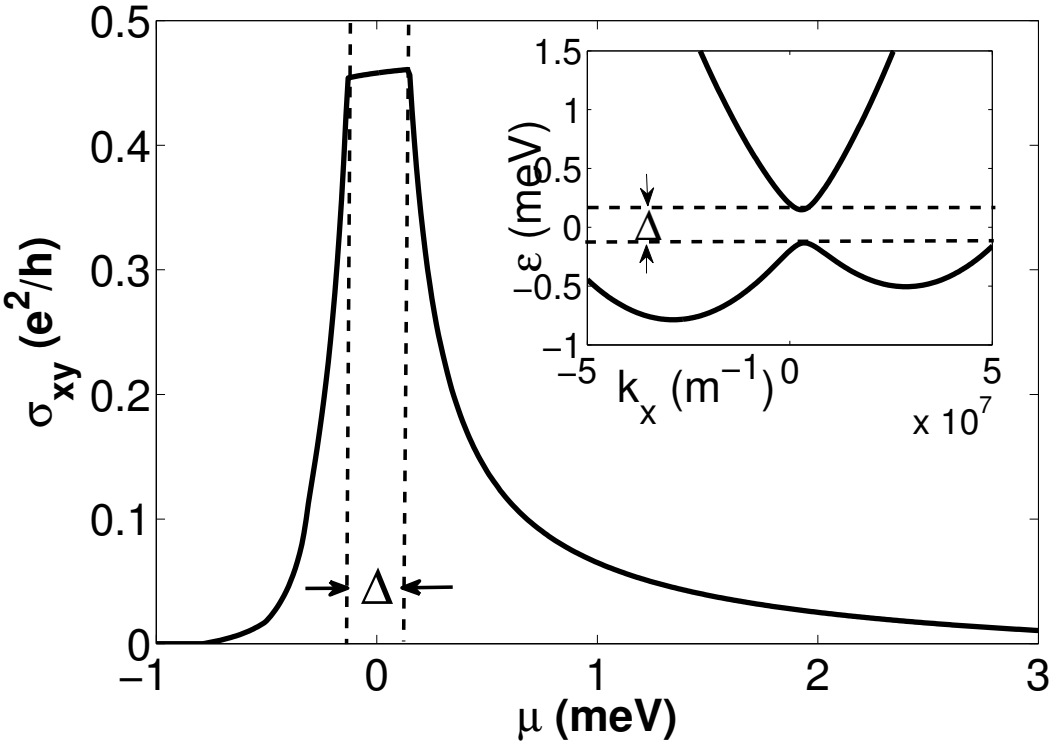

Figure 2.2: Anomalous Hall conductivity versus chemical potential μ at zero temperature for a two-dimensional electron-doped semiconductor. We have used $\alpha_R = \alpha_D = 4.74 \times 10^4$ m/s $m^* = .067m_e$ and $h_y = 0.2$ meV. The electronic band structure versus k_x is shown in the inset along with the minimum energy gap Δ indicated by the dashed lines

Figure 2.2 shows the dependence of the anomalous Hall conductivity on the chemical potential μ at zero temperature. The band structure near the origin is shown in the inset. Below $\mu \cong -0.5meV$ there is no contribution to the integral for the anomalous Hall coefficient (see Eq. (2.2)) as the states near the band gap minimum which have large Berry curvatures (Fig 2.1) are unoccupied. As μ increases these states are filled and there is a positive contribution to the integral from Ω_-. The quasi-plateau in the hall conductivity for μ corresponds to the energy gap between the two bands where there is a single large Fermi surface away from the origin. It is in this regime of chemical potential that the system supports the topological superconducting state because of the breakdown of the fermion doubling theorem. [17, 18, 19, 22] At higher μ the upper band becomes occupied, leading to a cancelation of the anomalous Hall conductivity due to the equal magnitude but opposite sign of the Berry curvatures of the two bands.

The anomalous Nernst coefficient for an electron-doped semiconductor near the topological regime is plotted against μ in Fig. 2.3. At low temperatures the entropy density $s_n(k)$ is sharply peaked at the Fermi

surface, such that the integrand in Eq. (2.4) is non-zero only for values of μ corresponding to the intersection of the Fermi surface(s) and the states near the minimum band gap (close to the origin) where the Berry curvatures are non-zero. Figure 2.3 illustrates this behavior with a positive peak from the lower band and a negative contribution from the upper band. For the chemical potential slightly below or above the topological regime the system has two (or an even number of) Fermi surfaces one of which lies close to the band degeneracy point. This small Fermi surface, because of a non-zero Berry curvature, gives a finite contribution to the anomalous Nernst effect which differs in sign between the regimes below and above the topological regime. As the topological regime is approached from either side, the Berry curvatures become increasingly sharply peaked (because of a decreasing E_0, see Eq. (2.6)) while the Fermi surface areas themselves go down resulting in a pair of peaks of opposite signs surrounding the topological regime. The topological regime itself is characterized by a single (or odd number of) Fermi surface with no weight near the band degeneracy points with significant Berry curvatures. Thus, the plateau between the two peaks in Fig. 2.3 corresponds to the minimum gap separating the energy bands and indicates the regime in which the topological superconducting state is possible.

2.3 Topological Hall and Nernst effects in hole doped semiconductors

Next we consider thin film hole doped semiconductor quantum wells grown in the [110] direction. In zinc-blende semiconductors the band structure is described by $\boldsymbol{k} \cdot \boldsymbol{p}$ perturbation theory.[54] Here the top valence bands consist of three p-orbitals which have an angular momentum $L = 1$ leading to a six fold degeneracy at the origin. Including spin, the total angular momentum operator becomes $J = L + S$ so that there are four $J = 3/2$ (heavy hole and light hole) and two (split-off) $J = 1/2$ bands which are separated by a large energy gap through atomic spin orbit coupling. We focus on the $J = 3/2$ bands described by the Luttinger Hamiltonian near $k = 0$ which is written as,

$$H_L = \frac{1}{m}\begin{bmatrix} P+Q & -S & R & 0 \\ -S^* & P-Q & 0 & R \\ R^* & 0 & P-Q & S \\ 0 & R^* & S^* & P+Q \end{bmatrix} \tag{2.7}$$

where the quantities P, Q, R are functions of the Luttinger parameters $\gamma_1, \gamma_2, \gamma_3$ and the momentum components k_x, k_y, k_z and act on the basis $|j, m\rangle$ with $j = 3/2$ and $m = 3/2, 1/2, -1/2, -3/2$ with spin quanti-

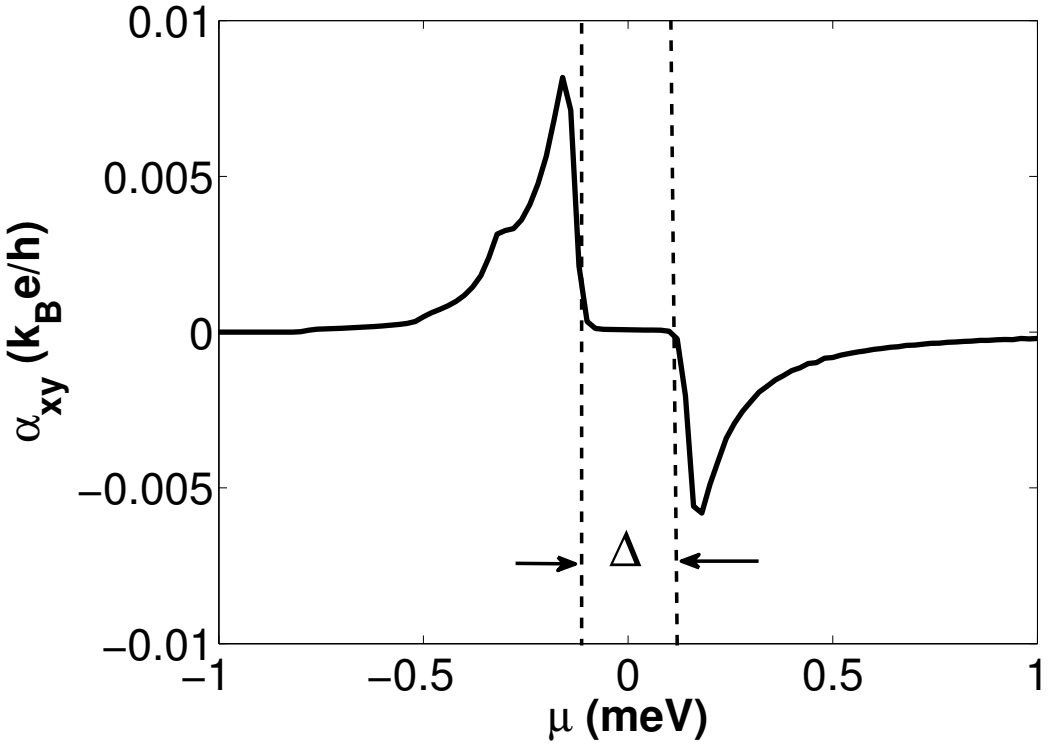

Figure 2.3: Anomalous Nernst coefficient versus chemical potential for 2DEG. The dashed lines show the regime of the energy gap Δ between the bands. The same parameters have been used as in Fig 2.2 with the exception of $T = 0.1K$

zation in the growth direction. In Ref. 23 topological superconducting states with a chiral-f-wave symmetry have been shown to exist in hole-doped quantum wells grown in the [001] direction in the presence of a perpendicular Zeeman field and Rashba spin-orbit coupling. A perpendicular Zeeman field, however, is unsuitable for investigations of the anomalous Hall and Nernst effects because such a magnetic field itself gives rise to conventional Hall and Nernst effects which are expected to dominate over the Berry-phase mediated anomalous response. Therefore, in order to uncover the anomalous Hall and Nernst effects in the topological regime of the hole-doped systems, we consider the semiconductor quantum well in the [110] direction with a Dresselhaus spin-orbit coupling and a parallel Zeeman field.

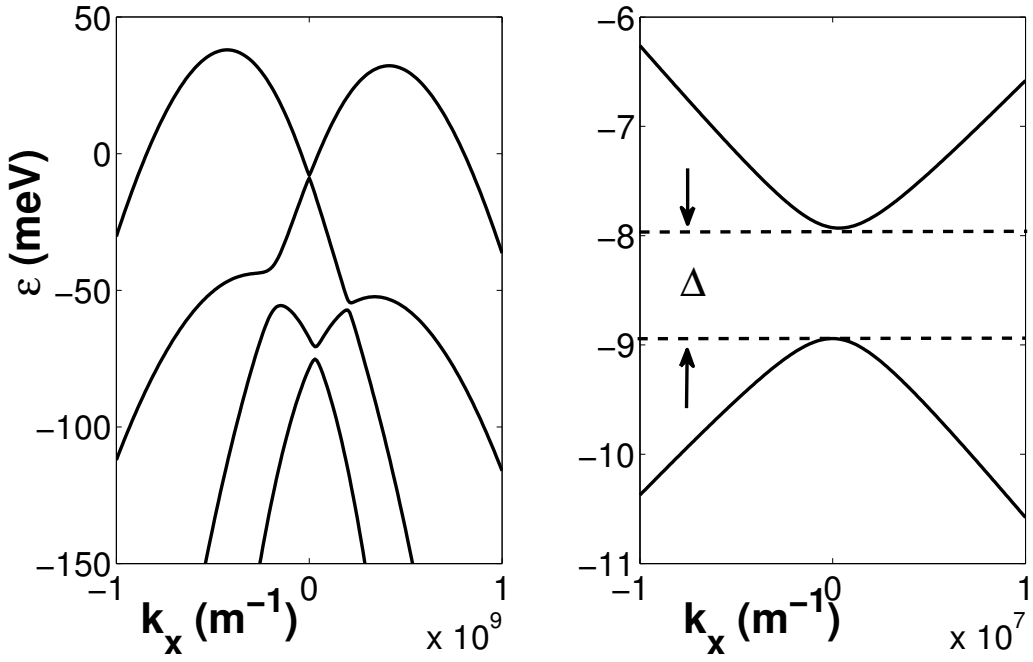

Figure 2.4: (a) Band structure of the 2DHG in the k_x direction for $k_y = 0$. (b) Energy gap at origin between lower bands. Here we have used $\alpha_R = \alpha_D = 2 \times 10^5$ m/s, $h_y = 5$ meV, $\gamma_1 = 6.92$,$\gamma_2 = 2.1$, $\gamma_3 = 2.9$ and $a = 8nm$ which are chosen for GaAs.

For the [110] growth direction, we have for the functions P, Q, R, [55]

$$\begin{aligned} P &= \frac{1}{2}\gamma_1(k_x^2 + k_y^2 + k_z^2) \\ Q &= \frac{1}{2}\gamma_2(k_x^2 - \frac{1}{2}k_y^2 - \frac{1}{2}k_z^2) + \frac{3}{4}\gamma_3(k_y^2 - k_z^2) \\ S &= \sqrt{3}(\gamma_3 k_x - i\gamma_2 k_y)k_z \\ R &= \frac{\sqrt{3}}{4}((\gamma_2 + \gamma_3)k_y^2 + (\gamma_2 - \gamma_3)k_z^3) \\ &\quad -\frac{\sqrt{3}}{2}(\gamma_2 k_x^2 - 2i\gamma_3 k_x k_y) \end{aligned} \tag{2.8}$$

where we now have k_x, k_y, k_z in the $[0, 0, -1]$, $[-1, 1, 0]$, and $[1, 1, 0]$ directions, respectively. Due to the confinement of the quantum well, the momentum is quantized in the growth direction and is approximated by $\langle k_z \rangle = 0$ and $\langle k_z^2 \rangle \approx (\pi/a)^2$ where a is the width of the well. This confinement projects the above Hamiltonian from three dimensions into two and also serves to lift the degeneracy between the heavy and light hole bands.

The single particle Hamiltonian for a two dimensional hole gas in a $[110]$ quantum well which is

expected to support topological superconductivity with s-wave proximity effect is the sum of the Luttinger, spin-3/2 Rashba, and Dresselhaus terms,

$$H = H_L + \alpha_R(\mathbf{J} \times \boldsymbol{k}) \cdot \hat{z} + \alpha_D k_x J_z + h_y J_y \tag{2.9}$$

where $\mathbf{J}$ is the total angular momentum operator given by the spin 3/2 matrices, γ_1, γ_2 and γ_3 are the Luttinger parameters, α_R and α_D are the strengths of the Rashba and Dresselhaus couplings and h_y is an in-plane Zeeman splitting as before. The form of the Rashba and Dresselhaus couplings in Eq. (2.9) for holes can be derived using nearly-degenerate perturbation theory.[54, 56] The band structure for this Hamiltonian is illustrated in Fig. 2.4 with parameters chosen for GaAs. It is clear from Fig. 2.4 that the combined effects of the Rashba, Dresselhaus, and the in-plane Zeeman splitting give rise to several regimes of the chemical potential where a spectral gap opens up near the band-degeneracy points. In analogy with the electron-doped semiconductors, when the chemical potential falls within the spectral gaps (topological regime) the system has an odd number of Fermi surfaces leading to topological superconductivity in the [110] grown hole-doped well in the presence of superconducting proximity effect.

Next, for a robust s-wave proximity effect on a hole-doped quantum well we need to ensure that the top valence band orbital wave functions couple with the orbitals of the adjacent s-wave superconductor. That this coupling is not automatically assured can be seen from the fact that the valence band holes are generically p-wave (in contrast to the conduction band electrons which are typically s-wave), and therefore coupling with the s-orbitals of the superconductor puts certain constraints on the value of m of the top valence band wavefunctions. To illustrate this, suppose the top valence band quantum state contains contributions only from pure eigenstates of J_z as $\left|j = \frac{3}{2}, m = \pm\frac{3}{2}\right\rangle$. Since $m = m_l + m_s$ where m_l and m_s are orbital and spin angular momentum quantum numbers, respectively, $m = \pm\frac{3}{2}$ implies that this state must consist of only $m_l = \pm 1$, $m_s = \pm\frac{1}{2}$ states. However in this case there will be no overlap between the superconductor orbitals if they are s-wave ($m_l = 0$) and the $m_l = \pm 1$ orbitals of the valence band, and no proximity induced superconductivity can be induced in the valence band. Therefore unlike in the electron conduction band, which consists of s orbitals, we must investigate the orbital angular momentum character of the valence bands for holes.

The eigenstates of the Hamiltonian in Eq. (2.9) are pure eigenstates of the operator J_z only at $k = 0$, but as k increases the bands become a mixture J_z eigenstates and can be written as a linear combination in the form $|\Phi_n\rangle = c_1(\boldsymbol{k})\left|\frac{3}{2}, \frac{3}{2}\right\rangle + c_2(\boldsymbol{k})\left|\frac{3}{2}, \frac{1}{2}\right\rangle + c_3(\boldsymbol{k})\left|\frac{3}{2}, \frac{-1}{2}\right\rangle + c_4(\boldsymbol{k})\left|\frac{3}{2}, \frac{-3}{2}\right\rangle$. Figure 2.5 shows the

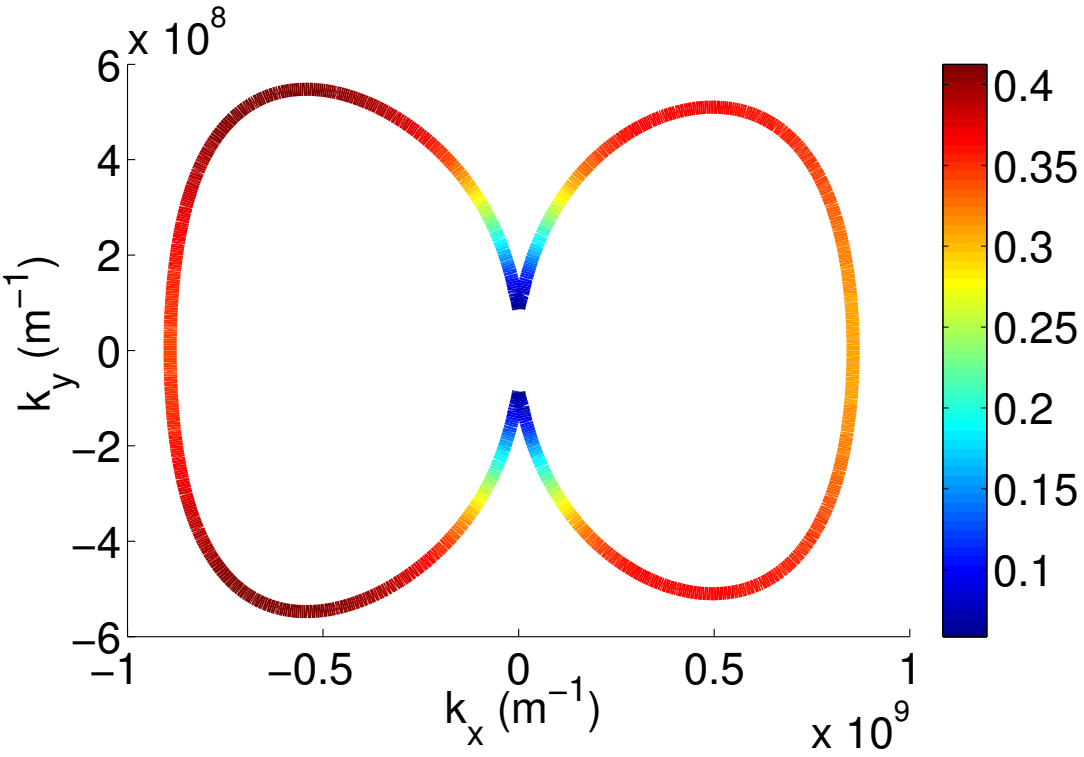

Figure 2.5: (Color online) Contour plot of the Fermi surface at μ corresponding to the topological regime ($\mu = -8.5$ meV). Color plot indicates the proportion of light-hole character ($m_j = \pm 1/2$) in the top valence band.

Fermi surface for a value of μ ($= -8.5$ meV) corresponding to the gap between the HH bands (topological regime, see Fig. 2.4) and the mixing of $m_j = \pm 1/2$ states given by $|c_2|^2 + |c_3|^2$ in the top band at the Fermi surface. Note that $m_j = \pm 1/2$ eigenstates can be re-written in the basis $|m_l, m_s\rangle$ as a linear combination of $\left|m_l = 0, 1, m_s = \frac{1}{2}, -\frac{1}{2}\right\rangle$ which guarantees the presence of $m_l = 0$ states at the Fermi surface allowing for robust proximity induced superconductivity.

Next we wish to calculate the Berry curvatures associated with the hole band structure shown in Fig. 2.4 numerically. In order to facilitate the calculations of the Berry curvatures, we use the following expression for the Berry curvature [39] which is equivalent to the form discussed earlier before Eq. (2.6),

$$\Omega_{xy}^{n} = i \sum_{n' \neq n} \frac{\left\langle \Phi_n \left| \frac{\partial H}{\partial k_x} \right| \Phi'_n \right\rangle \left\langle \Phi'_n \left| \frac{\partial H}{\partial k_y} \right| \Phi_n \right\rangle - (k_x \leftrightarrow k_y)}{(E_n - E_{n'})^2} \tag{2.10}$$

That this form of the Berry curvatures is equivalent to the earlier expression discussed before Eq. (2.6) can be understood by noting that $\langle \Phi_n | \nabla_k | \Phi_{n'} \rangle (E_{n'} - E_n) = \langle \Phi_n | \nabla_k H(k) | \Phi_{n'} \rangle$. [39] Eq. (2.10) has

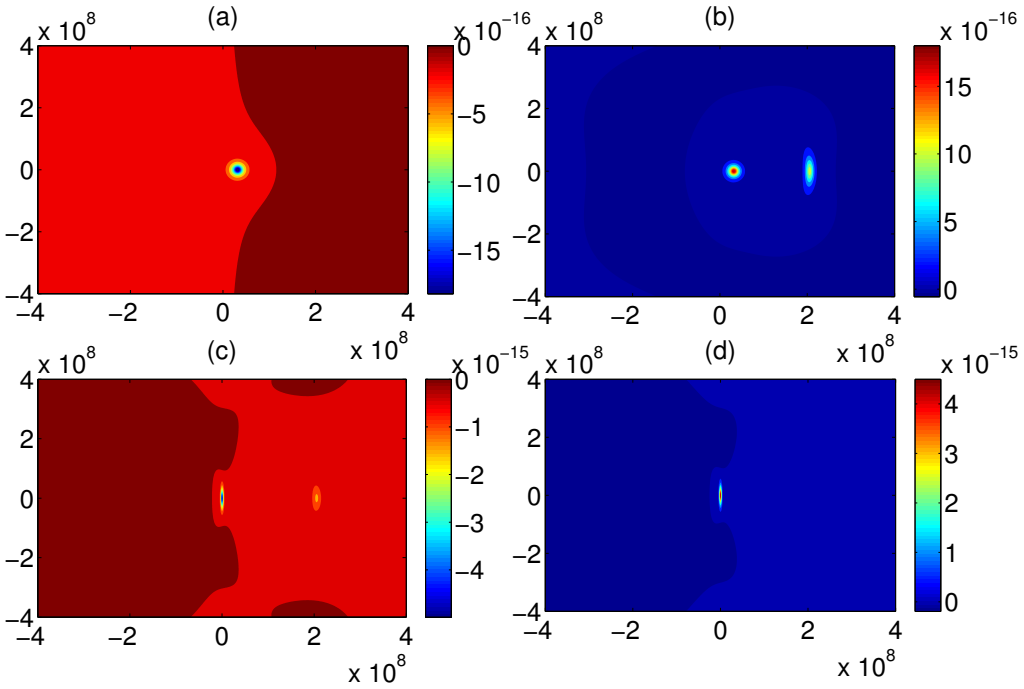

Figure 2.6: (Color online) Contour plot of Berry curvature of each band (units of m^2) where (a) corresponds to the lowest band and (d) to the highest. The y and x axis are k_y and k_x respectively with units of m^{-1}. As seen from the denominator of Eq. (2.10) these functions are sharply peaked at values of **k** near the near-band-degeneracy points.

the additional benefit that the arbitrary phase factors of the eigenstates from numerical diagonalization are ignored as there is no differentiation of the eigenstates involved. A contour plot of the Berry curvatures corresponding to each of the four bands is given in Fig. 2.6. As can be seen from this figure, the Berry curvatures are sharply peaked at points in k-space corresponding to the minimum energy gaps in the band structure of the holes, that is, near the near-band-degeneracy points.

We now calculate the anomalous Hall conductivity through Eq.(2.2) where we use Eq. (2.10) for the Berry curvatures, which is equivalent to the Kubo formula in linear response theory. Fig. 2.7 shows the dependence of σ_{xy} on μ at zero temperature. The physics of this effect is the same as that of the electron doped case but with Berry curvatures and a band structure that are more complicated. Decreasing μ excites more holes, filling each band, such that there are contributions to σ_{xy} corresponding to the overlap of the Fermi distribution function and Berry curvature for each band(Fig 2.6). As μ is made increasingly large and all bands are filled the sum of the contributions approaches zero. There is again, like in the case of the electron doped semiconductors, a small quasi-plateau corresponding to the topological regime of the chemical

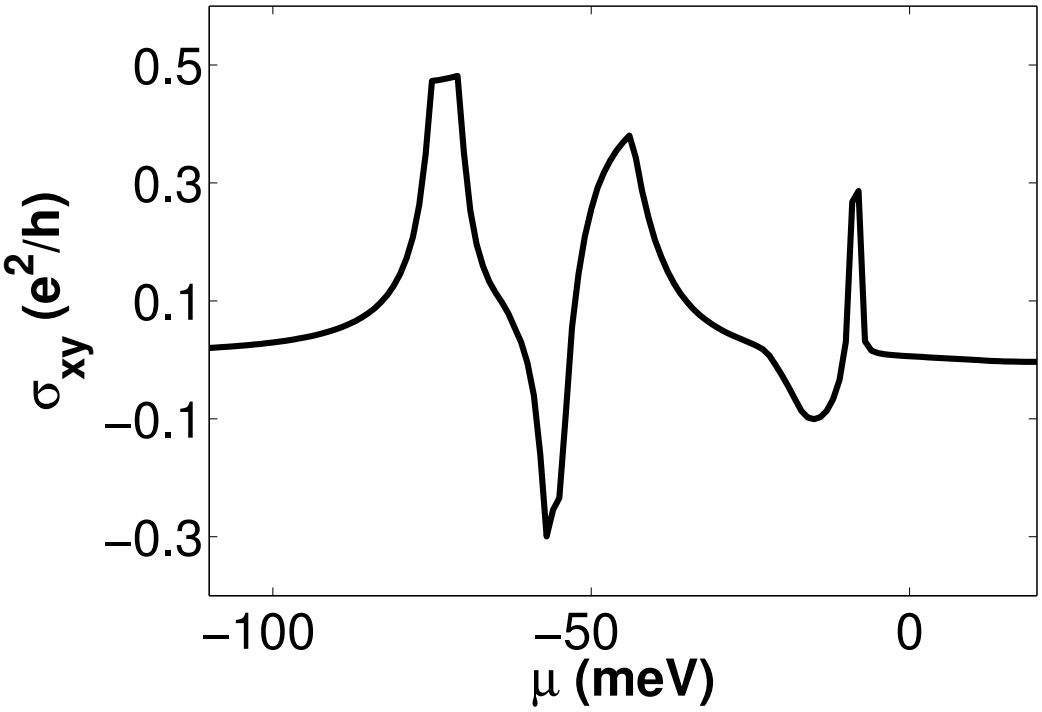

Figure 2.7: Plot of the anomalous Hall conductivity for the hole doped semiconductor at T=0 with the same paramaters as those used in Fig. 2.4.

potential separating the top two bands.

The regime of chemical potential suitable for topological superconductivity in the presence of s-wave proximity effect can be more clearly seen in the anomalous Nernst coefficient which has a well-defined plateau at vanishing values in the topological regime. We calculate the anomalous Nernst coefficient through Eq. (2.4) with the Berry curvatures found by using Eq. (2.10). The μ dependence of the Nernst coefficient is shown in Fig. 2.8 near the regime of μ near the energy gap Δ between the top bands as illustrated in Fig. 2.4. Similar to the electron doped systems, the integrand of Eq. (2.4) is a product of the entropy density, sharply peaked at the Fermi surface, and the Berry curvatures shown in Fig 2.6 which are peaked near the near-band-degeneracy points. There are two contributions to Fig. 2.8 as the Fermi surface corresponding to each band sweeps through the area of k-space near the origin where the Berry curvature is sharply peaked. The plateau for which the coefficient $\alpha_{xy} = 0$ corresponds to the energy gap between the bands which supports the topological superconducting state and is surrounded by well-defined peaks of opposite sign on either side. The vanishing of the Nernst effect, as before, originates from the clear momentum space separation between the single (or odd number of) Fermi surface, which is a requirement for the topological superconductivity

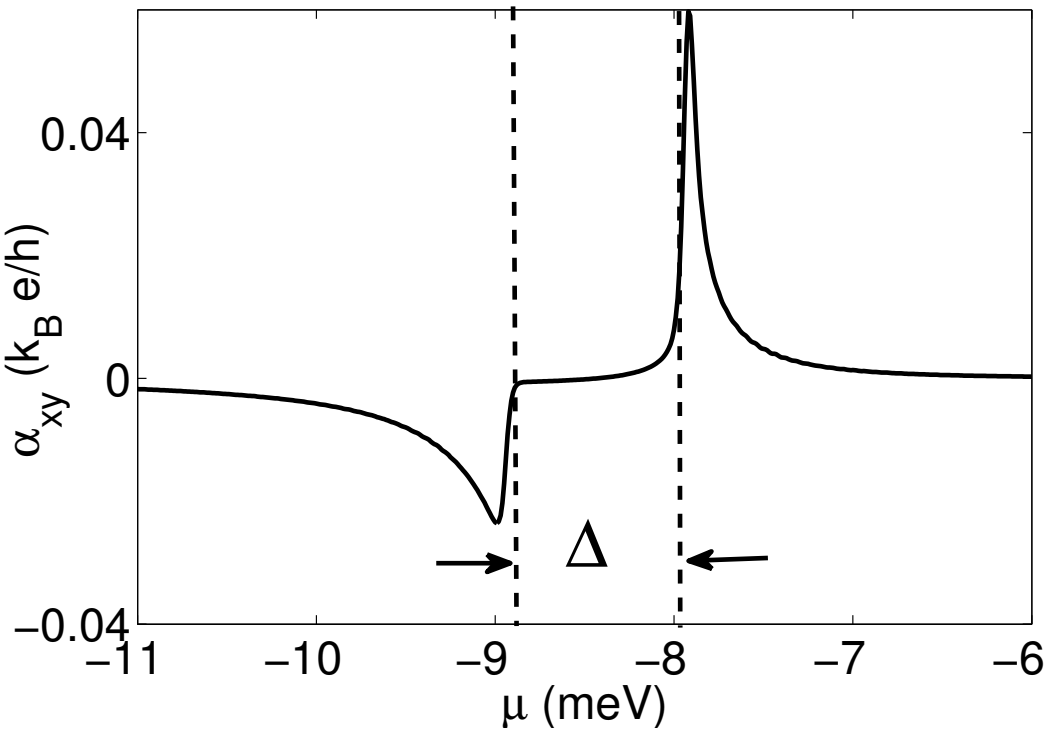

Figure 2.8: Plot of the anomalous Nernst coefficient for the $[110]$ grown hole-doped quantum well near the topological regime of the chemical potential. The topological regime of μ is characterized by a plateau of the anomalous Nernst coefficient (at vanishing values) flanked by two peaks of opposite signs as in the case of the electron-doped semiconductors. The parameters used are the same as in Fig. 2.4 except that $T = 0.1K$.

with Majorana fermions, and the regions in the momentum space (the near-band-degeneracy points) where the topological Berry phase is sharply peaked.

In this chapter we have studied the intrinsic contributions to the anomalous Hall and thermoelectric coefficients for thin film electron- and hole-doped semiconductors with Rashba and Dresselhaus spin orbit couplings and a suitably directed Zeeman field. Due to the presence of the spin orbit interactions and Zeeman field, a gap is induced in both the conduction and valence bands. When the chemical potential is inside the gap, the so called topological regime, it has been proposed that a topological superconducting state with Majorana fermions may be supported in the presence of s-wave superconducting proximity effect. For the study of anomalous Hall and Nernst effects, we require the applied Zeeman field to be parallel to the planes of the semiconductor. To achieve this, we first introduce the Hamiltonian of a $[110]$ grown hole-doped quantum well and show that in the presence of a parallel Zeeman field several topological regimes of chemical potential open up which can potentially support topological superconductivity in the presence of proximity effect. We

then discuss the wave function of the top hole-doped valence band and show that there is a considerable mixing of $m_j = \pm 1/2$ states which is necessary for proximity induced s-wave superconductivity. With the Hamiltonians for the electron- as well as hole-doped systems capable of supporting topological regimes of the chemical potential with only in-plane magnetic fields, we discuss the associated Berry curvatures. Time reversal and spatial inversion symmetry breaking give rise to non-trivial Berry curvatures at the points in k-space corresponding to local minimum gaps between energy bands, the so-called near-band-degeneracy points. We make use of this fact to show that the topological regimes of the chemical potential generically have well-defined plateaus in both anomalous Hall and Nernst effects. While the plateau in the anomalous Hall coefficient is at a non-zero value, the Nernst coefficient saturates in the topological regime at $\alpha_{xy} = 0$. The plateau at $\alpha_{xy} = 0$ is surrounded by well-defined peaks of the anomalous Nernst effect of opposite signs indicating the emergence of the topological regime. The vanishing of the Nernst effect in the topological regime originates from the clear momentum space separation between the single (or odd number of) Fermi surface, a requirement for the topological superconductivity with Majorana fermions, and the regions in the momentum space (the near-band-degeneracy points) where the topological Berry phase is sharply peaked.

Chapter 3

Topological Properties of one-dimensional superconductors

Multiple zero-energy Majorana fermions (MFs) with spatially overlapping wave functions can survive only if their splitting is prevented by an underlying symmetry. In this chapter we systematically analyze the the topological properties for Hamiltonians which describe spinfull p-wave superconductors, as well as s-wave superconductors in the presence of spin-orbit coupling and Zeeman fields, and illustrated that additional symmetries do exist in general. We begin by showing that the pair of Majorana modes at each end of a 1D spin triplet superconductor with total Cooper pair spin $S_x = 0$ (i.e., $\Delta_{\uparrow\uparrow} = -\Delta_{\downarrow\downarrow} = p\Delta_0$; two uncoupled time reversed copies of the Kitaev p-wave chain) are topologically robust to perturbations such as mixing by the $S_z = 0$ component of the order parameter ($\Delta_{\uparrow\downarrow} = \Delta_{\downarrow\uparrow}$), transverse hopping (in quasi-1D systems), non-magnetic disorder, and also, most importantly, to time reversal breaking perturbations such as applied Zeeman fields/magnetic impurities and the mixing by the $S_y = 0$ component of the triplet order parameter ($\Delta_{\uparrow\uparrow} = \Delta_{\downarrow\downarrow}$). We show that the robustness to time reversal breaking results from a hidden chiral symmetry which places the system in the BDI topological class with an integer $\mathbb{Z}$ invariant. This work has important implications for the quasi-1D organic superconductors $(TMTSF)_2X$ (X=PF_6, ClO_4) (Bechgaard salts) which have been proposed as triplet superconductors with equal spin pairing ($\Delta_{\uparrow\uparrow}, \Delta_{\downarrow\downarrow} \neq 0, \Delta_{\uparrow\downarrow} = 0$) in applied magnetic fields.

Turning our attention to systems which obey conventional time-reversal symmetry, we then study the magnetic field response of Majorana Kramers pairs of one-dimensional time-reversal invariant topological

superconductors (class DIII) with or without a coexisting chirality symmetry. We again emphasize how the anomalous magnetic field response of DIII class topological superconducting systems can be explained within the context of a coexisting class BDI chiral symmetry and provide a realistic route to engineer a "true" TR-invariant topological superconductor, i.e. one whose pair of Majorana bound states at each end is split by an applied Zeeman field in arbitrary direction. We also prove that quite generally the splitting of the Majorana bound states in a true time reversal invariant topological superconductor by time reversal breaking fields is highly anisotropic in spin space.

Finally we will show that multiple Majorana-Kramers pairs with strongly overlapping wave functions persist at zero energy even in the absence of an easily identifiable symmetry. We find that similar results hold in the case of quasi-one-dimensional (Q1D) semiconductor-superconductor heterostructures (class D) with $t_\perp \ll t$, where $t_\perp$ and t are the transverse and longitudinal hoppings, respectively. Our results, explained in terms of special properties of the Hamiltonian including spatial reflection symmetries, underscore the importance of hidden accidental symmetries in topological superconductors.

3.1 Topological superconducting platforms

It was shown by Read and Green [31] that 2D spinless p-wave superconductors host zero energy Majorana fermion (MF) excitations (with second quantized operator γ satisfying $\gamma^\dagger = \gamma$) in order parameter defects such as vortices and edges. Kitaev showed [36] that the 1D version of the same system (henceforth referred to as the "Kitaev p-wave chain") can host MFs at the chain ends which can be used for topological quantum computation [10]. Recently, MFs have been proposed to exist in systems closely analogous to the spinless p-wave superconductors/superfluids such as heterostructures of topological insulators and s-wave superconductors [57], cold fermion systems with Rashba spin orbit coupling, Zeeman field, and an attractive s-wave interaction [20, 21], and also, heterostructures of spin-orbit coupled semiconductor thin films [17, 19] or nanowires [19, 24, 25] proximity coupled with s-wave superconductors and a Zeeman field. There have been recent claims of experimental observation of MFs in the semiconductor heterostructure which have attracted considerable attention [58, 59, 60, 61, 62, 63, 64, 65, 16, 66]. In concurrent developments, recent work [67, 67, 68, 69] has established that quadratic Hamiltonians describing gapped topological insulators and superconductors may be classified into 10 distinct topological symmetry classes (the so called "ten-fold way") that can be characterized by certain topological invariants. The symmetry classification of a given system is important as it provides an understanding of the effects of various perturbations on the stability of

the protected surface modes such as the MFs. Generally speaking, if a given perturbation breaks a symmetry, the surface zero energy modes of the corresponding symmetry protected topological state acquire non zero energy and are removed by that perturbation.

Although the 1D spinless Kitaev chain has un unphysical Hamiltonian, quasi-1D spin-triplet superconductivity has been proposed in a class of organic superconductors $(TMTSF)_2X$ (Bechgaard salts, X=PF_6, ClO_4) in the presence of applied magnetic fields [70, 71, 72, 73], as well as in $Li_{0.9}Mo_6O_{17}$ [74]. The Bechagaard salts are quasi-one-dimensional charge transfer salts exhibiting pressure induced superconductivity with abnormally high upper critical fields H_{c2} [71]. The precise form of the order parameter is not completely known, but there is evidence that when in the presence of a magnetic field, the superconducting state is consistent with an equal-spin-pairing (ESP) p-wave phase [70, 71, 72, 73, 75, 76, 77]. Such a phase with $\Delta_{\uparrow\uparrow}, \Delta_{\downarrow\downarrow} \neq 0, \Delta_{\uparrow\downarrow} = 0$ realizes two independent copies of the Kitaev p-wave chain, one for each spin sector. By continuity from Kitaev's argument [36], since the two spin sectors are uncoupled, one expects *a pair* of MFs (one from each spin sector) at *each end* of the chains (the average spin-polarizations of the MFs are zero since they are an equal superposition of particles and holes within a single spin sector). Nevertheless, since for $\Delta_{\uparrow\uparrow} = -\Delta_{\downarrow\downarrow} = p\Delta_0$ (henceforth called the "TR-symmetric Kitaev chain") the Hamiltonian is symmetric under time reversal, it may appear that the pair of MFs at a given end are protected by the TR symmetry. The relevent topological class would be DIII, which is characterized by a $\mathbb{Z}_2$ invariant. A consequence of this would be that the MFs in $(TMTSF)_2X$ (or in $Li_{0.9}Mo_6O_{17}$) would acquire a gap in the presence of Zeeman fields and/or magnetic impurities and would be difficult to observe experimentally.

We now show that the pair of MFs at each end of a TR-symmetric Kitaev chain are in fact topologically robust to a large class of perturbations including mixing by the $S_z = 0$ component of the order parameter ($\Delta_{\uparrow\downarrow} = \Delta_{\downarrow\uparrow}$), transverse hopping (for quasi-1D systems), non-magnetic disorder, and also, importantly, to perturbations that explicitly break the TR symmetry such as Zeeman fields/magnetic impurities (in two orthogonal directions in spin-space) and perturbations rendering $|\Delta_{\uparrow\uparrow}| \neq |\Delta_{\downarrow\downarrow}|$ (i.e., mixing by the $S_y = 0$ component of the order parameter, $\Delta_{\uparrow\uparrow} = \Delta_{\downarrow\downarrow} = p\Delta_1$). Note that such TR-breaking perturbations are likely to be present in the experiments as the evidence for the possible spin-triplet order in Bechgaard salts is found only in the presence of magnetic fields [70, 71, 72]. We show that the topological robustness to the TR-breaking perturbations results from a hidden chiral symmetry that places the TR-symmetric Kitaev chain in the BDI topological class with an integer $\mathbb{Z}$ invariant. The integer invariant is equal to the number of MF modes at each end which are protected by the chiral symmetry. In quasi-1D systems with multiple coupled chains the $\mathbb{Z}$ invariant can take arbitrary integer values given a large number of connected chains. Our work

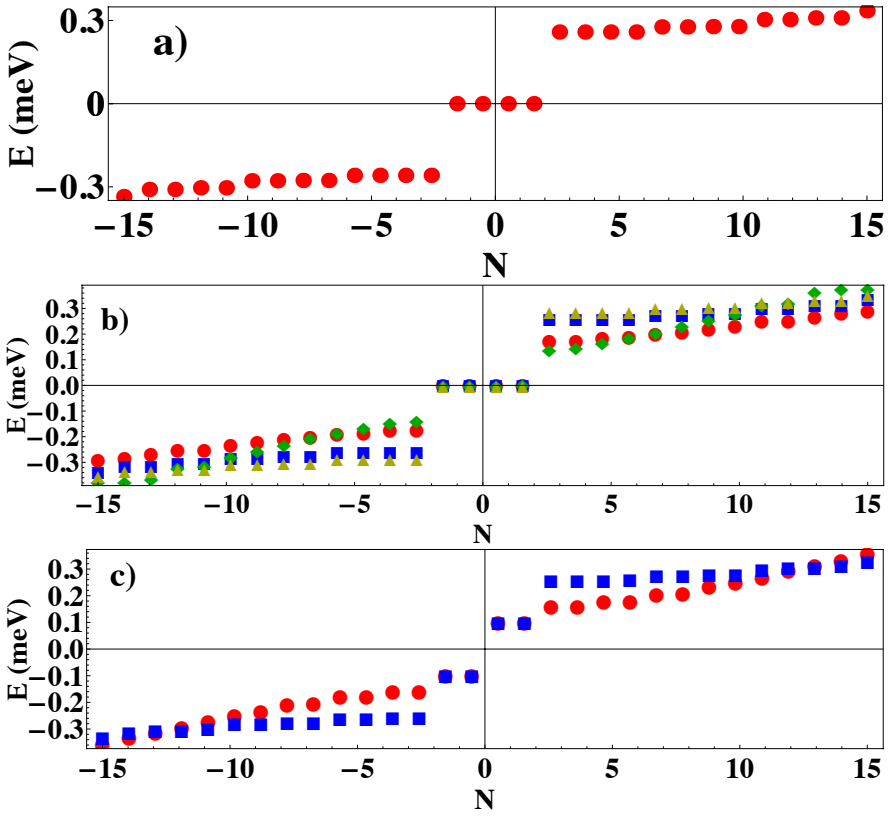

Figure 3.1: (Color online) (a) Low energy BdG quasiparticle spectrum for TR-symmetric Kitaev chain corresponding to Eq. (3.1) which hosts a pair of Majorana Fermions. The parameters used are as follows: $\Delta_0 = 0.5$meV, $\mu = 0.75$ meV, $N = 300$ sites, $a = 15$ nm, corresponding to a wire length of 4.5μm and a hopping amplitude of $t = 11$meV. (b) The response of the low energy spectrum to the TR-breaking perturbations given in Eq. (3.2). We have added bulk Zeeman splitting (red circles, $V_y, V_z = 0.4$ meV), magnetic impurity (blue squares) at wire endpoints of magnitude $J_y, J_z = 1$ meV, and mixing by the $S_y = 0$ ($S_z = 0$) component of the order parameter $\Delta_{\uparrow\uparrow} = \Delta_{\downarrow\downarrow} = 0.5\Delta_0$, green diamonds ($\Delta_{\uparrow\downarrow} = \Delta_{\downarrow\uparrow} = 0.5\Delta_0$, yellow triangles). (c) Zeeman splitting in the $\hat{x}$ direction ($V_x = 0.1$ meV, red circles) and localized at the endpoints ($J_x = 0.5$ meV, blue squares) split the MFs to finite energy

clarifies the topological properties of the doubled Kitaev chains and the related quasi-1D superconductors with a spin-triplet p-wave order parameter. Additionally, we will show that the MFs and the resultant zero bias tunneling peak [78, 79] and the fractional ac Josephson effect [36, 80, 81] should be topologically robust and experimentally observable in $(TMTSF)_2X$ and $Li_{0.9}Mo_6O_{17}$.

3.2 The spinfull Kitaev model and chiral symmetry

We begin with the 1D electronic tight binding Hamiltonian for a pair of Kitaev chains in uncoupled spin sectors,

$$H_1 = \sum_{i,\alpha}(-tc^\dagger_{i\alpha}c_{i+1,\alpha} - \mu c^\dagger_{i\alpha}c_{i\alpha} + \Delta_{\alpha\alpha}c^\dagger_{i\alpha}c^\dagger_{i+1\alpha} + h.c.), \tag{3.1}$$

where $i = 1, ..., N$ represents the lattice sites and $\alpha =\uparrow,\downarrow$ is the spin index. The first term in Eq. (3.1) represents the kinetic energy, μ is the chemical potential and $\Delta_{\alpha\alpha}$ is the ESP p-wave superconducting pair potential. For a finite wire we first solve the BdG equations corresponding to Eq. (3.1) for the TR-symmetric case, $\Delta_{\uparrow\uparrow} = -\Delta_{\downarrow\downarrow} = \Delta_0$ (see below for the TR-invariance of the doubled Kitaev chain) and choose parameters as follows: $\Delta_0 = 0.5$meV, $\mu = 0.75$ meV, $N = 300$ sites, $a = 15$ nm, corresponding to a wire length of 4.5μm and a hopping amplitude of $t = 11$meV. Given this choice of chemical potential the system realizes a non-trivial topological state and as shown in Fig. (3.1a), the low-energy spectrum for this system contains a total of four zero energy modes (two on each end) separated by a finite gap on each side. The wave functions for the pair of zero modes at each end are such that the corresponding second quantized operators satisfy the Majorana condition, $\gamma^\dagger_i = \gamma_i$.

Next, we examine the stability of the MFs against the TR-breaking perturbation Hamiltonian H_2,

$$\begin{aligned} H_2 &= \sum_{i,\alpha,\alpha'}[(\vec{V}\cdot\vec{\sigma})_{\alpha,\alpha'}c^\dagger_{i\alpha}c_{i\alpha'} + J(\vec{S}_i\cdot\vec{\sigma})_{\alpha,\alpha'}c^\dagger_{i\alpha}c_{i\alpha'} \\ &+ \Delta_1(c^\dagger_{i\uparrow}c^\dagger_{i+1\uparrow} + c^\dagger_{i\downarrow}c^\dagger_{i+1\downarrow}) + h.c]. \end{aligned} \tag{3.2}$$

The first term in Eq. (3.2) represents an applied Zeeman field $\vec{V} = (V_x, V_y, V_z)$, the second term represents magnetic impurities localized at site i with spin $\vec{S}_i$ and coupling constant J, and the third term Δ_1 adds an $S_y = 0$ component to the triplet order parameter. All three terms break the TR symmetry (note that the term Δ_1, added to a state with $S_x = 0$, makes the magnitudes of the order parameter in the two spin sectors unequal, $|\Delta_{\uparrow\uparrow}| \neq |\Delta_{\downarrow\downarrow}|$). Additionally, we checked the robustness of the MFs to TR-invariant perturbations such as ($\Delta_{\uparrow\downarrow} = \Delta_{\downarrow\uparrow} = \Delta_2$), non-magnetic disorder, and, for multiple coupled chains, to hopping in the transverse directions. Since the spin-orbit coupling in the organic superconductors is negligible [72] we have not included a Rashba spin-orbit term in the perturbation Hamiltonian.

Fig. (3.1b) shows the low energy BdG spectrum of the full Hamiltonian $H = H_1 + H_2$. The pair of MFs at each end remain protected to perturbations such as Zeeman fields and magnetic impurities along

two transverse directions, and also to mixing by the $S_y = 0$ and $S_z = 0$ components of the triplet order parameter. In addition we have also found (not shown in Fig. 1) that the MFs are robust to non-magnetic disorder and to transverse hopping (i.e. in a quasi-1D system). However we find that a Zeeman field along x (V_x) splits the MFs to finite energy $\pm\epsilon$ as illustrated in Fig. (3.1c). Nevertheless, since the MFs are robust to TR-breaking perturbations such as bulk V_y and V_z as well as magnetic impurities and mixing by the $S_y = 0$ component of the order parameter, the topological robustness of the MFs cannot be explained by the time reversal symmetry.

To understand the topological properties of the TR-symmetric Kitaev chain we take a Fourier transform of H_1 in Eq. (3.1) (for $\Delta_{\uparrow\uparrow} = -\Delta_{\downarrow\downarrow} = \Delta_0$)and write the Hamiltonian as, as $H_1 = \sum_k \Psi_k^\dagger H_1(k)\Psi_k$ where,

$$H_1(k) = (-2t\cos(k) - \mu)\sigma_0\tau_z + \Delta_0 \sin(k)\sigma_z\tau_x. \tag{3.3}$$

Likewise the perturbation Hamiltonian H_2 becomes $H_2 = \sum_k \Psi_k^\dagger H_2(k)\Psi_k$ with,

$$H_2(k) = V_x\sigma_x\tau_z + V_y\sigma_y\tau_0 + V_z\sigma_z\tau_z + \Delta_1 \sin(k)\sigma_0\tau_x, \tag{3.4}$$

where σ_i and τ_i are the Pauli matrices in the spin and the particle-hole spaces, respectively. Here we have used the coupled spin and particle-hole basis, $\Psi_k = (c_{k\uparrow}, c_{k\downarrow}, c^\dagger_{-k\uparrow}, c^\dagger_{-k\downarrow})^T$, and have replaced k_x by k. Using the time reversal operator Θ (Θ=$i\sigma_y\tau_0\mathcal{K}$) and the particle-hole operator Ξ ($\Xi = \sigma_0\tau_x\mathcal{K}$) in this basis, where $\mathcal{K}$ is the complex conjugation operator, it is easy to see that H_1 is TR-invariant ($\Theta H_1(k)\Theta^{-1} = H_1(-k)$) and has the particle-hole symmetry ($\Xi H_1(k)\Xi^{-1} = -H_1(-k)$). To understand the origin of the chiral symmetry, we introduce the operator $\mathcal{O} = -i\sigma_z\tau_z\mathcal{K}$, with $\mathcal{O}^2 = I$, under which the Hamiltonian is invariant ($\mathcal{O}H_1(k)\mathcal{O}^{-1} = H_1(-k)$). The presence of $\mathcal{O}$ and the particle-hole symmetry Ξ implies that H_1 has the chiral symmetry, $\{H, \mathcal{S}\} = 0$, where $\mathcal{S} = \mathcal{O}\cdot\Xi = \sigma_z\tau_y$ is the chirality operator and $\{,\}$ indicates the anti-commutator. The anti-commutation with $\mathcal{S}$ and commutation with $\mathcal{O}$, along with $\mathcal{O}^2 = I$, imply that the TR-symmetric Kitaev model is in the topological class BDI with an integer ($\mathbb{Z}$) winding number invariant W [67, 69, 82, 83]. Note that all the perturbations in Eq. (3.4), including non-magnetic disorder and transverse hopping, except V_x (and a magnetic impurity polarized along x), respect the chiral symmetry $\mathcal{S}$. As shown in Fig. 3.1 a perturbation such as V_x (and J_x) breaks the chiral symmetry, creating a gap and removes the MFs.

In order to calculate the topological winding number W we first off-diagonalize the Hamiltonian in

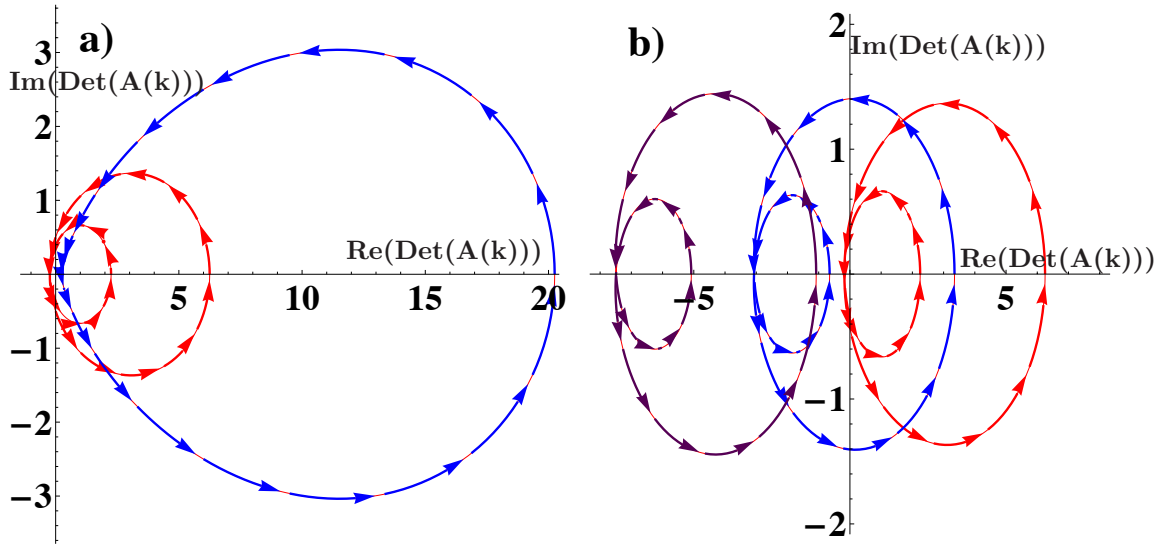

Figure 3.2: (Color online) Parametric plots of Re$(Det(A(k)))$ and Im$(Det(A(k)))$ as the momentum k is varied through the 1D Brillouin zone from $k = -\pi$ and π. (a) The winding of the angle $\theta(k)$ for the TR-symmetric Kitaev chain in the topologically non-trivial (red) and trivial (blue) phases corresponding to $|\mu| < 2t$ and $|\mu| > 2t$, respectively, indicating the existence of 2 and 0 MFs at each end. (b) The winding number in the presence of perturbation ($\Delta_{\uparrow\uparrow} = \Delta_{\downarrow\downarrow} = 0.5\Delta_0$), and 3 values of the Zeeman splitting, $V_y, V_z = 0.5\mu$ (red), 1.5μ (blue), and 3.3μ (purple). With increasing Zeeman fields, the Fermi surfaces disappear in turn and W decreases from 2 (red) to 1 (blue) to 0 (purple) indicating the corresponding disappearance of the MFs.

Eq. (3.3),

$$H^{'} = UHU^{\dagger} = \begin{pmatrix} 0 & A(k) \\ A^{\dagger}(-k) & 0 \end{pmatrix}, \tag{3.5}$$

and write the determinant of $A(k)$ in a complex polar form, $Det(A) = |Det(A)|e^{i\theta(k)}$. The winding number W is then given by [82] $W = 1/(2\pi)\int_{-\pi}^{\pi} d\theta(k)$.

In Fig. (3.2a), we show the winding number in the topologically non-trivial and trivial phases of the TR-symmetric Kitaev chain. The winding number is 2 (0) in the topologically non-trivial (trivial) phases indicating the existence of 2 (0) topologically protected MFs on a given end. In Fig. (3.2b) we show that the winding number is 2 even in the presence of the perturbations V_y, V_z and $\Delta_{\uparrow\uparrow} = \Delta_{\downarrow\downarrow} \neq 0$ (red curve). This explains the topological robustness of the pair of MFs on a given end of the finite wire (Fig. (1)). In Fig. (2b), blue and purple curves indicate the evolution of W with increasing Zeeman fields V_y, V_z. Even though the chiral symmetry is still unbroken, the Zeeman field can change the value of W from $2 \rightarrow 1 \rightarrow 0$, indicating a corresponding decrease of the number of MFs on a given end. Physically, the Zeeman field reduces the number of MFs by 1 by removing the individual Fermi surfaces in turn.

Next we consider the Hamiltonian in Eq. (3.1) with $\Delta_{\uparrow\uparrow} = \Delta_{\downarrow\downarrow}$ (ESP phase with $S_y = 0$). In this phase, as we show in Fig. (3a), the winding number $W = 0$ (red curve). Although $W = 0$, since the two spin sectors are uncoupled and each sector hosts a single MF, the system has a total of 2 MFs on a single end. However, in this case the pair of MFs are *accidental* with respect to the chiral symmetry $\mathcal{S}$, meaning that they are *not* topologically protected by $\mathcal{S}$. We see the absence of the topological protection in Fig. (3b) where a small Zeeman field V_y, even though it respects the symmetry under $\mathcal{S}$ (see Eq. (3.4)), still removes the MFs from the chain ends. Fig. (3c,3d) illustrate the fact that in the $S_y = 0$ phase, a field $V_z > \mu$ can remove one of the Fermi surfaces, resulting in the winding number increasing from 0 to 1 (Fig. (3c)), which is then protected by the chiral symmetry $\mathcal{S}$. We note in passing that the pair of MFs in the $S_y = 0$ phase are also protected to V_x, V_z, but this protection is provided by a different chiral symmetry $\tilde{\mathcal{S}} = \sigma_0\tau_y$.

To illustrate the possibility for higher integer values of W (and, correspondingly, higher number of protected MFs per end) let us now consider multiple chains coupled in the transverse directions by hopping parameters t_y, t_z. Since in the Bechgaard salts the hopping ratios are $t_x : t_y : t_z = 1 : 0.1 : 0.03$ [] we consider only the effects of t_y. In the limiting case $t_y \rightarrow 0$ there exist a set of degenerate 1D chains each hosting 2 MFs at each end and a small hopping between the chains $t_y \ll t_x$ breaks this degeneracy. Despite the degeneracy breaking, the additional terms in the Hamiltonian do not break the chiral symmetry

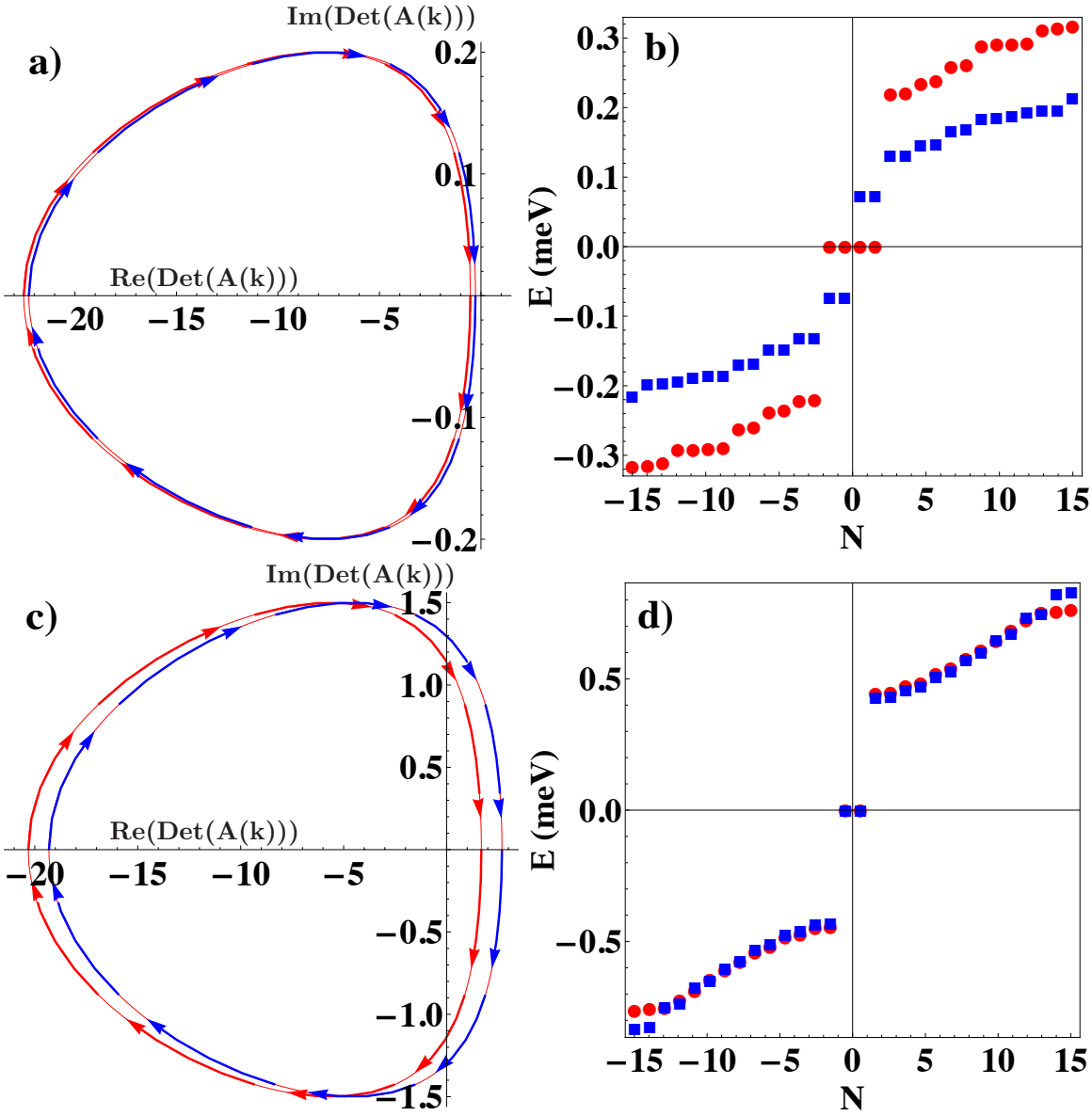

Figure 3.3: (a) The winding of the angle $\theta(k)$ for the ($S_y = 0$) Kitaev chain with $\Delta_{\uparrow\uparrow} = \Delta_{\downarrow\downarrow}$ with the two spin sectors uncoupled (red) and coupled by a Zeeman splitting $V_y = 0.25$ meV (blue). In both cases $W = 0$. (b) Low energy BdG spectrum for the uncoupled spins (red circles) shows 2 *topologically unprotected* MFs at each end. Since the MFs are unprotected (see text), even a chiral symmetric perturbation $V_y = 0.25$ meV splits them to finite energy (blue squares). (c) Increasing the Zeeman splitting in the $\hat{z}$ direction ($V_z > \mu$) drives the system through a topological phase transition into a phase with winding number $W = 1$. We show the winding for uncoupled spins (red) and with additional Zeeman splitting $V_y = 0.25$ meV (blue). (d) Low energy BdG spectrum in the $W = 1$ regime for uncoupled spins (red circles) and in the presence of V_y (blue squares) illustrating the topological protection of the MF.

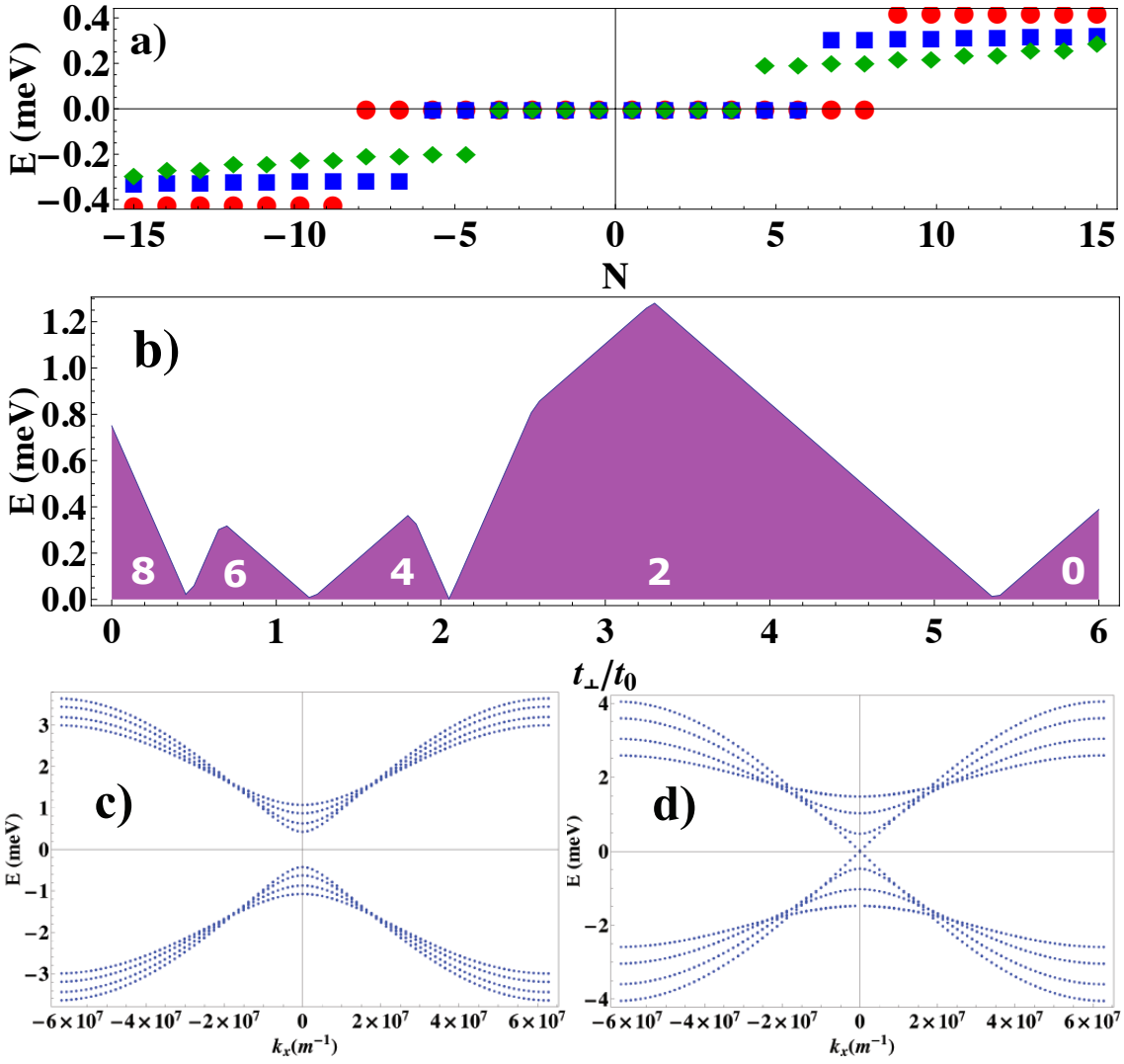

Figure 3.4: (a) Low energy BdG spectrum of four parallel chains coupled by transverse hopping t_y. $t_y/t_x = 0.2, 0.75, 1.5$ correspond to 8 (red circles), 6 (blue circles), and 4 (green diamonds) MFs at each end. (b) Quasiparticle gap closing and TQPT (separating phases with different number of MFs) tuned by the transverse hopping. Panels (c, d) show the bulk energy-momentum dispersion in the gapped regime with 8 MFs and as the bulk gap closes leading to the regime with 6 MFs at each end.

and the multi-chain problem is the winding number W formulation remains valid (suitably defined for a larger dimensional H).

If $t_y \ll t_x$ between N conducting chains, such that the confinement energy is much smaller than the chemical potential, the system will accommodate $2N$ sets of Majorana fermions. As the strength of t_y increases the confinement energy lifts the energy of the bands above μ such that they are no longer occupied. Thus the number of MFs localized at an end (and the value of W) goes down in pairs. As shown in Fig. 3.2, at each jump of the value of W, the superconducting quasiparticle gap closes and the system passes through a topological quantum phase transition (TQPT).

In principle, the MFs in 1D chiral symmetric topological superconductors can be probed by differential tunneling conductance from the ends [84]. Additionally, in a butt-to-butt Josephson set up between two 1D chiral TS there now exists a stable Majorana quartet (two MFs on each side of the junction). The energy levels of the junction plotted as a function of the phase difference ϕ is 4π periodic [80, 81], giving rise to a 4π periodic Josephson effect (see Fig. (3.5a)). As shown in Figs. (3.5b, c), the topological robustness due to chiral symmetry ensures that the single crossing of the E vs. ϕ curves at $\phi = \pi$ is stable to perturbations including those breaking TR symmetry. In Fig. (3.5d) we show that the 4π periodicity of the curves is broken only by adding a Zeeman field V_x that breaks the chiral symmetry $\mathcal{S}$.

3.3 True time-reversal invariance

Recently, one-dimensional (1D) time reversal (TR) invariant topological superconductors (in class DIII) have been proposed where *a pair* of MBSs exist on each end of a quantum wire [85, 86, 87, 88, 89, 90, 91, 92]. Even though a pair of zero energy states are localized at the same end, they are protected against hybridization (and acquiring finite energies) by TR symmetry. These systems are characterized by a DIII class $\mathbb{Z}_2$ invariant which takes a non-trivial value when the pairing potential has a negative sign on an odd number of Fermi surfaces each of which encloses a TR-invariant momenta [93]. In Ref. 88 this is achieved by having a quantum wire with Rashba spin-orbit coupling proximity coupled to an unconventional $s_\pm$ wave superconductor with pair potential Δ_k changing sign between the two Fermi surfaces. A non-trivial $\mathbb{Z}_2$ invariant implies that no perturbation respecting TR symmetry can remove the MBS pair from the wire ends without closing the bulk gap. Conversely, it is expected that perturbations that do break the TR symmetry can split the pair of MBSs to higher energies by hybridization.

In this section we first show that 1D TR-invariant (TRI) TS systems in class DIII which are $s_\pm$ wave

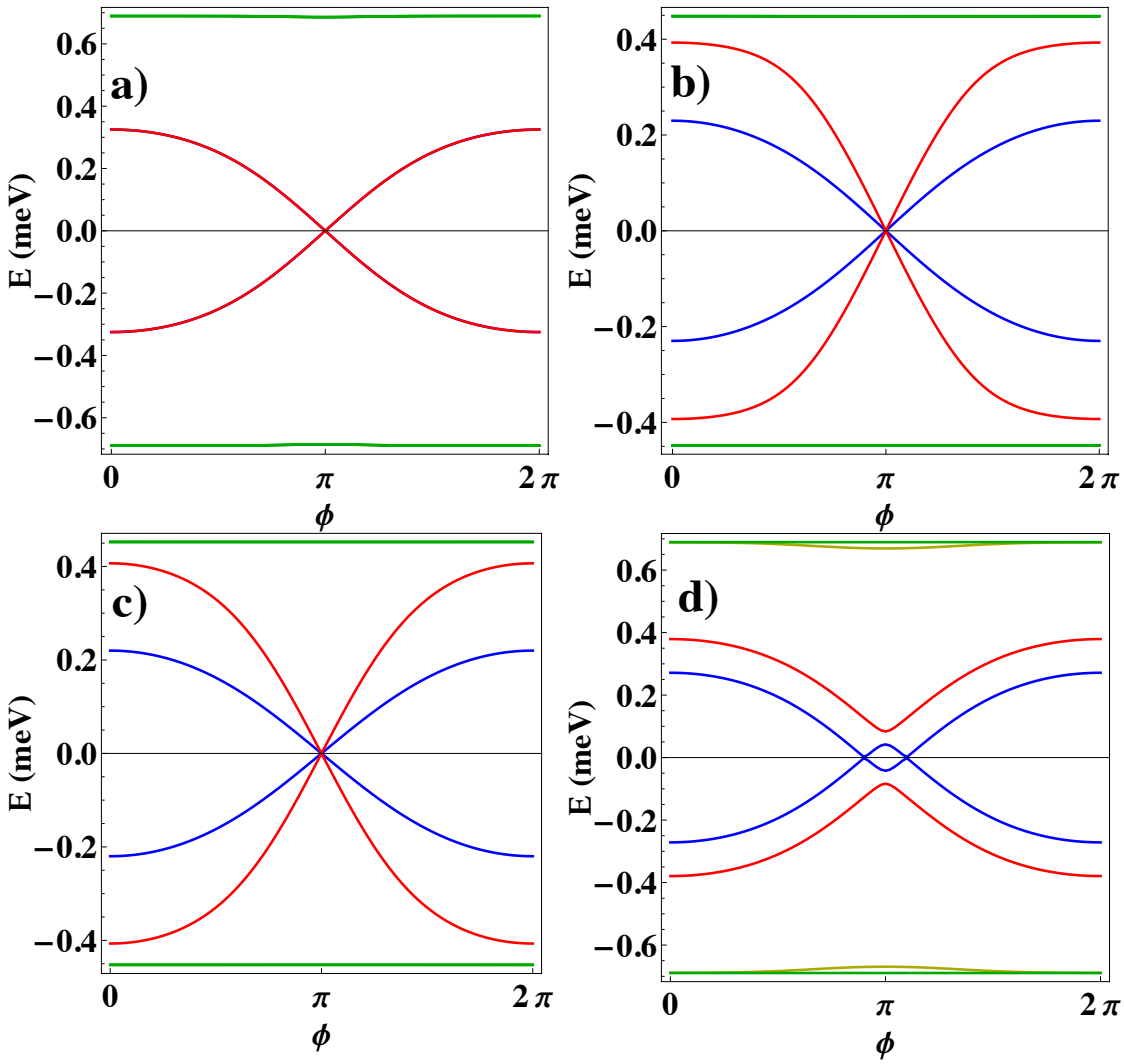

Figure 3.5: (a) Low energy ABS spectrum as a function of ϕ for TR-symmetric Kitaev chain with parameters as in Fig. 1. Each red curve is twofold degenerate. (b) TR-breaking bulk Zeeman fields $V_y, V_z = .25$ meV lift the degeneracy but preserves the 4π periodicity of the spectrum. (c) Adding the order parameter component with $\Delta_{\uparrow\uparrow} = \Delta_{\downarrow\downarrow} = 0.5\Delta_0$, although it breaks the TR symmetry, preserves the 4π periodicity (d) The spectrum with $V_x = 1$ meV added to the junction breaks chiral symmetry and results in a conventional 2π Josephson effect.

superconductor based frequently possess the BDI co-existing chiral symmetry allowing an integer $\mathbb{Z}$ topological invariant. For unbroken TR invariance the parameter regimes for nontrivial values of the $\mathbb{Z}_2$ invariant and the $\mathbb{Z}$ invariant coincide, each indicating the presence of the Kramers pair of MBSs. We emphasize that broken TR may not be accompanied by broken chirality, and if the chiral symmetry is unbroken, the pair of MBSs at a given end can survive the loss of the TR symmetry. We show that the existence of the chiral symmetry explains the persistence of the MBSs even in the presence of magnetic fields in a *plane* perpendicular to the spin-orbit coupling (the chiral symmetry was used earlier to explain the robustness of the zero modes to Zeeman fields in a specific direction in spin space in Rashba-coupled d-wave superconductors [94, 85]). Conversely, we find that broken chirality may also not be accompanied by broken TR symmetry, and in this case also the MBSs remain un-split due to the persistence of the $\mathbb{Z}_2$ TR invariant. By numerically solving the appropriate BdG equations for a $s_\pm$-wave TRI superconductor we find that only those physical perturbations that simultaneously break both TR and chiral symmetries can hybridize the MBSs and split them to finite energies. Additionally, we provide a realistic route to engineer a "true" TRI TS system whose Majorana Kramers pairs are split by an applied Zeeman field in *any* direction. In this case we find that the splitting of the MBSs by TR-breaking Zeeman fields is highly anisotropic in spin space, and this can be taken as a strong signature of TRI superconductivity and Majorana Kramers pairs.

Let us now adopt new notation and consider a TRI TS system given by the following BdG Hamiltonian $H = \sum_k \Psi_k^\dagger \mathcal{H}_k \Psi_k$ where,

$$\mathcal{H}_k = (\epsilon_k - \mu)\sigma_0\tau_z + \alpha_k^R(\hat{a}\cdot\boldsymbol{\sigma})\tau_z + \Delta_k^s\sigma_0\tau_x \tag{3.6}$$

where $\epsilon_k = -2t\cos(k)$ is the single particle kinetic energy, $\alpha_k^R = \alpha_R \sin k$ is the Rashba-type spin orbit interaction, and $\Delta_k^s = \Delta_0 + \Delta_1\cos(k)$ represents the spin-singlet superconducting pair potential with a conventional s-wave order parameter (Δ_0) and a $s_\pm$ [88] or d-wave component ([85]) (Δ_1). σ_i,τ_i are spin $1/2$ Pauli matrices in the spin and the particle-hole spaces respectively, and we have used the Nambu basis, $\Psi_k = (c_{k\uparrow}, c_{k\downarrow}, c_{-k\downarrow}^\dagger, -c_{-k\uparrow}^\dagger)^T$. The vector $\hat{a}$ indicates an arbitrary spin orbit coupling direction in the spin space. Selecting $\hat{a}$ along $\hat{y}$, Eq. (3.6) reduces to the 1D Hamiltonian used in [88]. We solve the corresponding lattice BdG equations for a finite wire setup and find zero energy Majorana quasiparticle modes. The wavefunctions for the zero energy modes are localized at the wire ends, as illustrated in Fig. 3.6 panel (a), subject to the constraint that the chemical potential satisfies $|\mu| < 2\alpha_R$ and the $\mathbb{Z}_2$ TR invariant takes a non-trivial value (see Fig. 3.6 panels (b,c)).

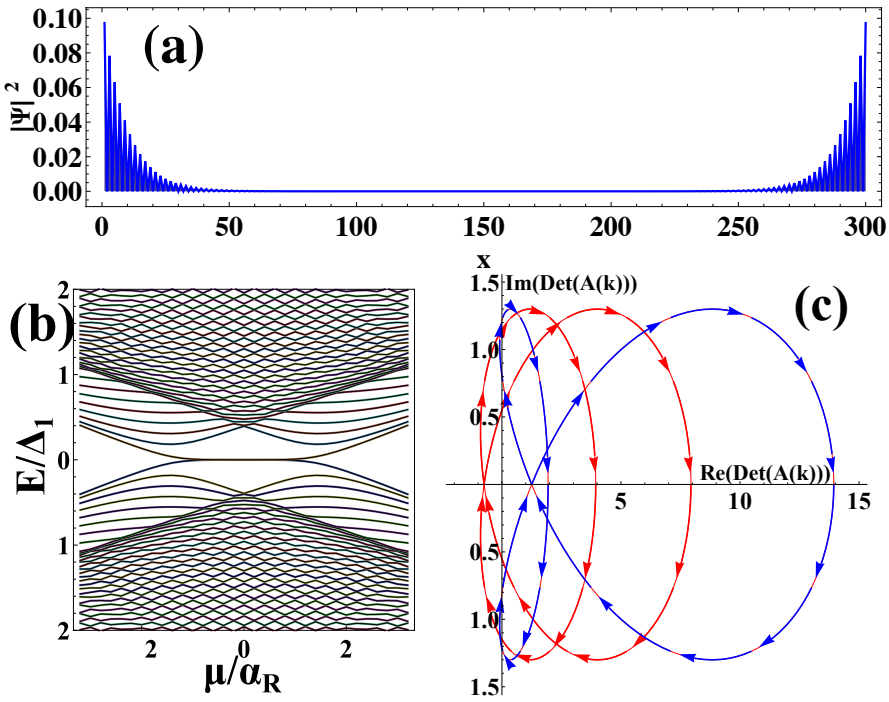

Figure 3.6: (Color online) (a) Probability amplitude $|\Psi(x)|$ of the lowest energy solution to Eq. 3.6 on a finite system with a length of 300 sites. (b) The low energy BdG spectrum as a function of chemical potential μ. Each band is doubly degenerate, with 2 MBSs at each end of the nanowire in the $|\mu| < 2\alpha_R$ topologically non-trivial regime. (c) Parametric plot of Re$(Det(A(k)))$ and Im$(Det(A(k)))$ as the quasi-momentum k is varied through the 1D Brillouin zone ($k \in [-\pi, \pi]$). The red curve ($|\mu| < 2\alpha_R$, non-trivial regime) winds about the origin twice as k is varied through the Brillouin zone yielding a chiral invariant $W = 2$. Upon increasing the chemical potential, the blue curve ($|\mu| > 2\alpha_R$ topologically trivial regime) winds about the origin 0 times indicating a decrease in the chiral invariant from $W = 2$ to $W = 0$.

Due to the fact that we have written Eq.3.6 in a modified basis with respect to Eq.3.3, we review the symmetric properties of Eq.3.6 within the new basis. In addition to the particle-hole symmetry ($\Xi\mathcal{H}_k\Xi^{-1} = -\mathcal{H}_{-k}$ with the operator $\Xi = \sigma_y\tau_y\mathcal{K}$) the above Hamiltonian (i.e.Eq. 3.6) satisfies the TR condition $\Theta\mathcal{H}_k\Theta^{-1} = \mathcal{H}_{-k}$ with $\Theta = i\sigma_y\tau_0\mathcal{K}$ where $\mathcal{K}$ is the complex conjugation operator. For the parameter range $|\mu| < 2\alpha_R$ the TR $\mathbb{Z}_2$ topological invariant has a non-trivial value and a pair of MBSs localized at each end of the nanowire. Note however, that there exists an operator $\mathcal{O} = (\hat{a}\cdot\hat{y} + i(\hat{a}\times\hat{y})\cdot\boldsymbol{\sigma})\mathcal{K}$ with $\mathcal{O}^2 = 1$ which acts on the Hamiltonian similarly to the TR operator, $\mathcal{O}\mathcal{H}_k\mathcal{O}^{-1} = \mathcal{H}_{-k}$. Due to the existence of $\mathcal{O}$ and the presence of Ξ, there exists a chiral operator $S_2 = \mathcal{O}\cdot\Xi = (\hat{a}\cdot\boldsymbol{\sigma})\tau_y$ which anti-commutes with the Hamiltonian. Note that it is trivial to show that the operator $S_1 = \sigma_0\tau_y$ also anti-commutes with the BdG Hamiltonian as σ_0 (τ_y) commutes (anti-commutes) with each term in Eq. (3.6). However, invariants calculated with this operator (see below) are inconsistent with the behavior of the BdG spectrum and we note

that S_1, S_2 form a two dimensional vector space of chiral operators anti-commuting with $\mathcal{H}_k$.

The existence of the S_2 symmetry allows us to compute an $\mathbb{Z}$ invariant counting the number of topologically protected MBSs at each end of the wire. In the eigenbasis of S_2 the BdG Hamiltonian still takes the off-diagonal form

$$\mathcal{H}_k^{'} = U\mathcal{H}_k U^{\dagger} = \begin{pmatrix} 0 & A_k \\ A_{-k}^{\dagger} & 0 \end{pmatrix} \tag{3.7}$$

where U is the unitary transformation matrix between the two eigenbasis. Again writing the determinant of A_k, a complex quantity, in its polar form, $Det(A_k) = |Det(A_k)| \exp[i\theta(k)]$. For a gapped system, the topological invariant is given by the winding number W [82, 83],

$$W = \frac{1}{2\pi i} \int_{-\pi}^{\pi} \frac{dz(k)}{z(k)}. \tag{3.8}$$

with $z(k) = \exp[i\theta(k)]$. W counts the number of times $\theta(k)$ winds about the origin in the complex plane. Note that this quantity is invariant under smooth deformations and cannot change without $|Det(A_k)|$ going to zero, indicating a gap closing and topological phase transition. As shown in Fig. 3.6 panel (b) the winding number in the regime ($|\mu| < 2\alpha_R$) is 2, while in the topologically trivial regime the winding number is 0. This corresponds exactly with the parameter regime for which the DIII class $\mathbb{Z}_2$ invariant takes a non-trivial value [85, 88]. Thus in the non-trivial topological regime the Hamiltonian given by Eq. (3.6) is characterized by the coexistence of TR *and* chiral symmetries. Next we investigate the behavior of the Majorana Kramers pair in the presence of terms which break one symmetry while maintaining the other, and finally when both symmetries are destroyed.

3.3.1 TR-breaking perturbations maintaining chiral invariance

In order to illustrate the dual protection afforded by both time-reversal symmetry and chiral symmetry, let us now consider the effect of TR-breaking perturbations such as Zeeman splitting in an arbitrary direction on the low energy BdG spectrum for a finite wire. A spatially uniform Zeeman splitting, due to a uniform magnetic field for example, is written as

$$\mathcal{H}^Z = V(\boldsymbol{b} \cdot \boldsymbol{\sigma})\tau_0. \tag{3.9}$$

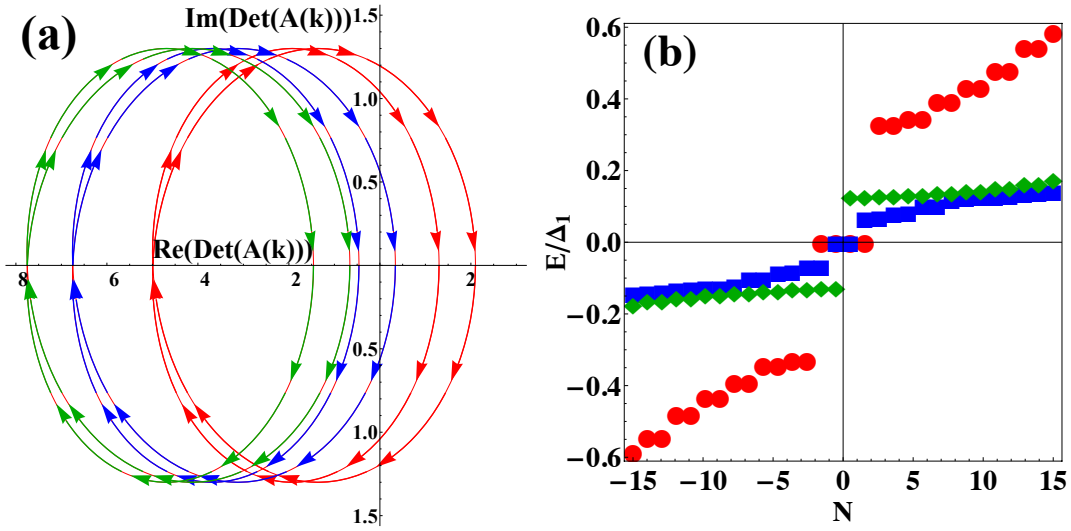

Figure 3.7: (Color online) (a) Winding curves for the bulk BdG Hamiltonian given by Eqs. (3.6,3.9) which preserves the chiral symmetry ($\boldsymbol{b} \perp \hat{a}$). The red, blue, and green curves yield chiral invariants $W = 2, 1, 0$ connected by gap closures and topological phase transitions. (b) Low energy BdG quasiparticle spectrum corresponding to the winding curves in panel (a). Here N counts the number of positive (negative) energy eigenvalues above (below) the Fermi energy. The chiral invariant counts the number of topologically protected modes at each end of the nanowire.

The total BdG Hamiltonian is a sum of Eq. (3.6) and this term as $\mathcal{H}_{tot} = \mathcal{H}_k + \mathcal{H}^Z$. Note that for $\boldsymbol{b} \perp \hat{a}$ this term anti-commutes with S_2, preserving the chiral symmetry of the system. The MBSs are topologically protected and immune to splitting by Zeeman fields in the two directions (and on the entire plane formed by them) perpendicular to the spin-orbit field. Increasing the magnitude of the splitting may however remove one Fermi surface driving the system through a topological quantum phase transition into a state which is effectively a spinless p-wave superconductor, and hence supports a single MBS at each edge. Further increasing the Zeeman splitting removes the second Fermi surface driving the system into a trivial phase as seen in Fig. 3.7. Thus, in the presence Zeeman splitting discussed above, it is appropriate to classify the system as a chiral topological superconductor with an $\mathbb{Z}$ invariant. Note that a Zeeman splitting $\boldsymbol{b} \parallel \hat{a}$ commutes with S_2, breaking both TR and chiral symmetries. In this case the MBSs do in fact couple as a result of the broken symmetries and the zero energy modes are split to finite energy (Fig. [3], panel (a)).

3.3.2 Chirality breaking perturbations maintaining TR-invariance

Conversely, we wish to consider terms in the BdG Hamiltonian which break the chiral symmetry while preserving TR-symmetry. For example, one may examine the response of the zero energy modes to the

inclusion of a TR-invariant next nearest neighbor spin-orbit coupling. In the absence of Zeeman splitting the total Hamiltonian is written as a sum of Eq. (3.6) and

$$\mathcal{H}_k^{SO'} = \alpha' \sin(2k)(\boldsymbol{c} \cdot \boldsymbol{\sigma})\tau_z. \tag{3.10}$$

Here the vector $\boldsymbol{c}$ indicates the axis of the next-nearest neighbor spin-orbit coupling. Regardless of this direction, Eq. 3.10 always respects the TR condition, $\Theta\mathcal{H}_k\Theta^{-1} = \mathcal{H}_{-k}$. If $\boldsymbol{c} \parallel \hat{a}$ the spin-orbit coupling has a fixed axis and the chiral S_2 symmetry is maintained. In this case, the results of the preceding section are applicable and the MBSs are robust to the application of magnetic fields in the plane perpendicular to $\hat{a}$. However, for $\boldsymbol{c} \perp \boldsymbol{a}$, the extra spin-orbit coupling commutes with S_2, breaking the chiral symmetry. Physically, the next-nearest neighbor spin-orbit coupling corresponds to the spin quantization axis being different at the different spin-split Fermi points. Such a difference in spin-polarizations between the two Fermi points is natural in the limit where the Fermi points are sufficiently separated to allow a different sign of the pairing potential. Since such a difference in sign in the pair potential between the two spin-split Fermi points is achieved in the topological regime ($|\mu| < 2\alpha_R$) [88] the next-nearest neighbor spin-orbit coupling is expected in this regime. Because the perturbation $\mathcal{H}^{SO'}$ does not break time-reversal symmetry, Kramers theorem dictates that Majorana fermions can only occur in pairs and a single Kramers pair of Majorana modes at either of the ends of the nanowire cannot be split by $\mathcal{H}^{SO'}$.

3.3.3 Zeeman splitting in a spin-nonconserving Hamiltonian – signature of a "true" TR-protected topological superconductor

An $\mathcal{H}^{SO'}$ which breaks the chiral symmetry leads to a topological state in which spin is not conserved and Kramers pairs of MBSs are hybridized by Zeeman splitting in all directions. Note that, in the absence of such a term the spin operator $\hat{a} \cdot \sigma$ commutes with the Hamiltonian whereby this component of spin is conserved. However, as argued below, even in this general time-reversal invariant case, where no chiral symmetry is present, the splitting of the MBSs at small Zeeman fields is still highly anisotropic in spin space, and this property can be used as a diagnostic signature of Majorana-Kramers pairs in experiments.

To understand the splitting in more detail, we consider the response of the MBSs on the right end of the wire to an applied magnetic field. We assume that the MBSs on the left end have been gapped out by a localized magnetic field, which does not affect the right end of the wire. The splitting and crossing of the MBSs on the right end as a function of the magnetic field $V = \sum_{a=x,y,z} B_a\sigma_a$ can be analyzed by studying

Table 3.1: Possible 1D topological invariants in the presence of Zeeman fields (Eq. 3.9) and second nearest neighbor spin-orbit coupling (Eq. 3.10). Here $\hat{a}$ is the direction of the nearest neighbor spin orbit field and $\boldsymbol{b} = 0$ indicates no Zeeman splitting.

	$\boldsymbol{b} = 0$	$\boldsymbol{b} \parallel \hat{a}$	$\boldsymbol{b} \perp \hat{a}$
$\boldsymbol{c} \parallel \hat{a}$	$\mathbb{Z}, \mathbb{Z}_2$	0	$\mathbb{Z}$
$\boldsymbol{c} \perp \hat{a}$	$\mathbb{Z}_2$	0	0

the Pfaffian of the BdG Hamiltonian

$$Q(\boldsymbol{B}) = Pf(\sigma_y \tau_y H_{BdG}(\boldsymbol{B})), \tag{3.11}$$

where we have taken advantage of the fact that $\sigma_y \tau_y H_{BdG}$ is anti-symmetric and allows the definition of a Pfaffian. The Pfaffian Q defined here is related to the Majorana number defined by Kitaev [36], and corresponds to the fermion parity of the ground state. More importantly, the Hermiticity of H_{BdG} dictates that $Q(\boldsymbol{B})$ is real and since $Q(\boldsymbol{B})^2 = Det(H_{BdG})$, $Q(\boldsymbol{B})$ can only change sign when an odd number of pairs of energy levels cross zero-energy. Therefore, in our system, where only the energy levels on the right side can cross zero-energy when a small $\boldsymbol{B}$ is applied, the splitting and crossing of MBSs is determined by $Q(\boldsymbol{B})$. The MBSs are unsplit only when $Q(\boldsymbol{B}) = 0$. Since the MBSs are unsplit at $\boldsymbol{B} = 0$, $Q(\boldsymbol{B} = 0) = 0$. Applying the time-reversal operator $i\sigma_y K$ to Eq. (3.11) we observe that $Q(\boldsymbol{B})^2 = Q(-\boldsymbol{B})^2$. This allows two choices $Q(\boldsymbol{B}) = \pm Q(-\boldsymbol{B})$ where only the case with the $-$ sign corresponds to having an odd number of MBSs that are split by the Zeeman field. This case corresponds to the $\mathbb{Z}_2$ non-trivial TRI superconductor such that Q satisfies

$$Q(\boldsymbol{B}) = -Q(-\boldsymbol{B}). \tag{3.12}$$

At small $\boldsymbol{B}$, one can expand $Q(\boldsymbol{B})$ as

$$\begin{aligned} Q(\boldsymbol{B}) &= \sum_a [\rho_a B_a \{1 + \sum_{b,c} \rho_{abc} B_b B_c (1 + \sum_{d,f} (\rho_{abcdf} B_d B_f \\ &+ \ \ldots)\}], \end{aligned} \tag{3.13}$$

where ρ_a, ρ_{abc}, and ρ_{abcdf} are coefficients that in principle can be determined in perturbation theory.

Using Eq. 3.13, we note that there is a unique direction $\boldsymbol{b}_1$ parallel to $\boldsymbol{\rho}$, where the MBSs split linearly as long as $\boldsymbol{B}$ is not in the plane perpendicular to $\boldsymbol{b}_1$. This is similar to the chiral case where the Zeeman potential is applied along the axis of the spin-orbit field. The existence of a unique axis with such

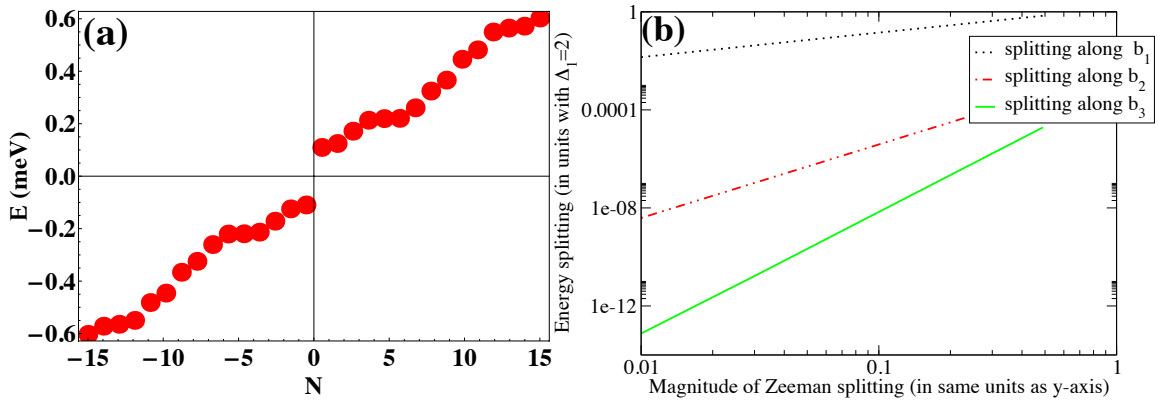

Figure 3.8: (Color online) (a) Energy splitting of the MBSs in the presence of Zeeman splitting V along $\hat{y}$ (along the direction of spin orbit direction) as described in Eq. (3.9). (b) Energy splitting as a function of Zeeman field along three orthogonal directions $\boldsymbol{b}_{1,2,3}$ described in the text on a log-log scale are found (from the slope) to split as V,V^3 and V^5, where V is the magnitude of the Zeeman field. Thus, in the presence of next-nearest neighbor spin-orbit coupling described by Eq. 3.10, the MBSs split in every direction. Both axes are in units where the pairing potential $\Delta_1 = 2$.

a strong splitting of MBSs is a general feature of the TR-invariant state. In general the MBS splitting when $\boldsymbol{B}$ is in the plane perpendicular to $\boldsymbol{\rho}$ is of order B^3. However, varying $\boldsymbol{B}$ along the circle with $\boldsymbol{B} \cdot \boldsymbol{\rho} = 0$ and $|\boldsymbol{B}|$ held fixed we conclude that since $Q(\boldsymbol{B})$ is odd in $\boldsymbol{B}$, the splitting must vanish at some point on the circle. Along this direction $\boldsymbol{b}_3$, the cubic coefficient also vanishes and the splitting of the MBSs is expected to be even slower, i.e. of order B^5. The splitting in the perpendicular direction $\boldsymbol{b}_2 = \boldsymbol{b}_1 \times \boldsymbol{b}_3$ is of order B^3. By considering the nanowire with a next-nearest neighbor spin-orbit coupling with strength $\alpha' = \alpha$, and calculating numerically the MBS energies in the plane perpendicular to the direction where the MBSs split linearly, we see in Fig. 3.8 that the MBSs in this model split in all directions.

3.4 Spatial reflection symmetry

In Q1D multi-chain systems multiple Majorana fermions with spatially overlapping wave functions can remain at zero energy only if their splitting is forbidden by an underlying symmetry. In this work we show that, in Q1D TR-invariant topological superconductors, multiple Majorana-Kramers pairs (MKPs) with strongly overlapping wave functions persist at zero energy even in the absence of an identifiable physical symmetry. We find similar results also for Q1D semiconductor-superconductor heterostructures with spin-orbit (SO) coupling and Zeeman field (class D with $\mathbb{Z}_2$ invariant) with $t_\perp \ll t$, pointing to the existence of a hidden symmetry decoupling of the MFs.

To demonstrate this result we start with a strictly 1D (single chain) TR-invariant Kitaev model superconductor (Eq. (3.14)), modeling the ESP spin-triplet p-wave state proposed to be realized in LiMO. Remember tha in addition to TR-invariance, the model has a chiral as well as a mirror symmetry both of which allow an integer ($\mathbb{Z}$) invariant. In the physically realistic Q1D generalization of this model (with $t_\perp \ll t_x$) the $\mathbb{Z}$ invariant takes arbitrary integer values, allowing multiple MKPs localized at the same end despite wave-function overlap. We show that, even in the absence of such symmetries, multiple MFs can still be protected by symmetries such as spatial reflection. In realistic materials, however, reflection symmetry is expected to be broken by disorder. Remarkably, we find that disorder induced breakdown of reflection symmetry fails to lift the degeneracy of the zero energy modes even with strong wave function overlap. We find very similar results also for Q1D systems in class D. These results, which we explain in terms of special properties of the Hamiltonians and wave functions, underscore the importance of hidden symmetry decoupling of MFs in topological superconductors.

We model a one dimensional spin-triplet topological superconductor by a lattice Hamiltonian which includes nearest neighbor hopping, on-site chemical potential and a general p-wave superconducting order parameter which reads,

$$H^{\text{1D}} = \sum_{i,\sigma,\sigma'} [-tc^\dagger_{i+1\sigma}c_{i,\sigma} - \mu c^\dagger_{i\sigma}c_{i\sigma} + \Delta_{\sigma\sigma'}c^\dagger_{i+1\sigma}c^\dagger_{i\sigma'} + H.c.]. \tag{3.14}$$

Here $t = t_x$ is the hopping integral between nearest neighbor sites, $i \in [1, N_x]$ is the lattice index and $\sigma = \uparrow, \downarrow$ represents the spin index. Next, we Fourier transform Eq. (3.14) to study the 1D bulk topological properties. In momentum space, the superconducting gap function which describes correlations between electrons is written $\Delta_{\alpha\beta}(\mathbf{k}) = \langle c_\alpha(\mathbf{k})c_\beta(-\mathbf{k})\rangle$, where $c_\alpha(\mathbf{k})$ is the destruction operator of a single electron with spin α and momentum $\mathbf{k}$. The spin symmetry of Cooper pairing may be classified by the total spin as either singlet ($S = 0$) or triplet ($S = 1$). A general pair potential is expressed compactly in terms of a d-vector as $\Delta_{\alpha\beta}(\mathbf{k}) = [\Delta_s(\mathbf{k}) + \mathbf{d}(\mathbf{k}) \cdot \boldsymbol{\sigma}]\,(i\sigma_y)_{\alpha\beta}$ with a symmetric singlet component $\Delta_s(\mathbf{k}) = \Delta_s(-\mathbf{k})$, and an antisymmetric triplet d-vector $\mathbf{d}(\mathbf{k}) = -\mathbf{d}(-\mathbf{k})$. In this work we will consider a pure triplet order parameter with $\Delta_s(\mathbf{k}) = 0$, however the following analysis is general and applicable in the presence of a singlet term. As an example, consider a Cooper pair in a state with zero spin projection along $\hat{z}$, that is $S_z = 0$. This is in fact a Cooper pair described by the familiar triplet state $|\uparrow\downarrow\rangle + |\downarrow\uparrow\rangle$ and corresponds to a pairing potential in Eq. 3.14 with $\Delta_{\uparrow,\downarrow} = \Delta_{\downarrow,\uparrow}$.

We now write the bulk Hamiltonian corresponding to Eq. (3.14) as a momentum space Bogoliubov-

de Gennes (BdG) Hamiltonian, $H^{1\mathrm{D}} = \sum_k \Psi_k^\dagger \mathcal{H}_k \Psi_k$. With the Nambu basis $\Psi_k = (c_{k\uparrow}, c_{k\downarrow}, c_{-k\downarrow}^\dagger, -c_{-k\uparrow}^\dagger)^T$ which absorbs the factor $i\sigma_y$ associated with the d-vector, the matrix $\mathcal{H}_k$ then takes the form

$$\mathcal{H}_k^{1D} \quad = \quad (\epsilon(k) - \mu)\sigma_0\tau_z + \mathbf{d}(k)\cdot\boldsymbol{\sigma}\tau_x. \tag{3.15}$$

Here $k = k_x$ is the 1D crystal-momentum, $\epsilon(k) = -2t(\cos(k) - 1)$ is the single particle kinetic energy, $\mathbf{d}(k) = \hat{d}|\mathbf{d}(k)| = (d_x, d_y, d_z)\Delta\sin(k)$ is the p-wave order parameter and σ_i,τ_i indicate spin $1/2$ Pauli matrices in the spin and the particle-hole spaces respectively. The bulk spectrum consists of two doubly degenerate bands given by the dispersion relation $E_\pm = \pm\sqrt{(\epsilon_k - \mu)^2 + |\mathbf{d}(k)|^2}$.

Superconducting Hamiltonians observe an intrinsic particle-hole symmetry (PHS) which emerges from the structure of the BdG equations. The BdG Hamiltonian in Eq. (3.15) satisfies $\Xi\mathcal{H}_k\Xi^{-1} = -\mathcal{H}_{-k}$, where, in this basis the anti-unitary PHS operator reads $\Xi = \sigma_y\tau_y\mathcal{K}$ where $\mathcal{K}$ is the anti-unitary complex conjugation operator. Ξ anti-commutes with the real space representation of $\mathcal{H}_k^{1D}$ and obeys $\Xi^2 = 1$. PHS which relates quasiparticle excitations at $\pm E$ through $\Gamma_E^\dagger = \Gamma_{-E}$ is fundamentally important for the formation of Majorana modes which are a special case satisfying $E = 0$. Additionally, $\mathcal{H}_k^{1D}$ obeys the time-reversal symmetry (TRS) relation $\Theta\mathcal{H}_k\Theta^{-1} = \mathcal{H}_{-k}$ with the TR operator $\Theta = \sigma_y\tau_0\mathcal{K}$. The presence of PHS and TRS leads to a unitary chiral symmetry which is simply the product $\Pi = \Xi\cdot\Theta = \sigma_0\tau_y$. When $|\mu| < 2t$ the system is in the topologically non-trivial phase, characterized by a DIII class $\mathbb{Z}_2$ invariant which takes a value $\nu = -1$. This invariant may be viewed as a Kramers polarization and reduces to Kitaev's Pfaffian invariant for one spin block in the presence of spin rotation symmetry [95]. When $\nu = -1$ unpaired MFs at each end of the wire form topologically protected MKP's. This explains the robustness of the four zero energy modes in the presence of TR-invariant perturbations, for example spin-orbit coupling terms such as $\mathcal{H}^{SO} = \alpha_R\sin(k)\sigma_y\tau_z$ added to Eq. (3.15). Additionally, the BdG Hamiltonian Eq. (3.15) belongs to the topological class BDI, due to a co-existing chiral symmetry given by $\mathcal{S}^{BDI} = \mathcal{O}\cdot\Xi = (\hat{d}\cdot\boldsymbol{\sigma})\tau_y$, which is the product of a TR-like operator $\mathcal{O} = (\hat{d}\cdot\hat{y} + i(\hat{d}\times\hat{y})\cdot\boldsymbol{\sigma})\mathcal{K}$ with $\mathcal{O}^2 = 1$, and the particle-hole operator Ξ. In $d = 1$ BDI Hamiltonians are classified by a bulk $\mathbb{Z}$ topological winding number invariant W. To calculate the invariant we off-diagonalize the Hamiltonian from Eq. (3.15) in the basis which diagonalizes $\mathcal{S}^{BDI}$. Writing the determinant of the off-diagonal part in a complex polar form, $D_k = |Det(D_k)|e^{i\theta(k)}$, W is given by [82, 83] the number of times $\theta(k)$ winds about the origin as k varies through the 1D Brillouin zone. As can be seen from Fig. [3.9], panel (a), the invariant takes the value $W = 2$ in the topological phase of Eq. (3.15) while $W = 0$ in the trivial phase. This chiral symmetry explains the persistence of the zero

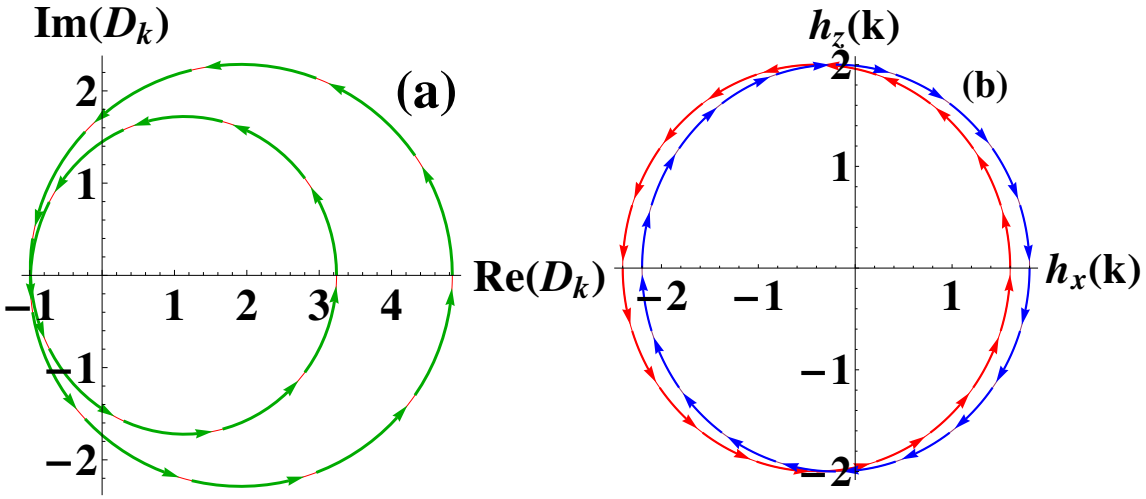

Figure 3.9: (Color online) (a) Chiral topological invariant $W = 2$ indicating two topologically protected MFs at each end of a single chain described by Eq. (3.15) (b) Mirror topological invariant $\gamma_M = 2$ (difference of the winding numbers in the two mirror subsectors) also indicating two MFs at each end of a single chain in Eq. (3.15).

modes to TR-breaking terms including stray Zeeman fields ($\mathcal{H}^Z = \boldsymbol{V} \cdot \boldsymbol{\sigma}\tau_0$) perpendicular to the d-vector. A generic SO coupling term aligned in an arbitrary direction in spin space is written $\mathcal{H}^{SO} = \alpha_R \sin(k)\boldsymbol{a} \cdot \boldsymbol{\sigma}\tau_z$ meaning that $\boldsymbol{a} \parallel \boldsymbol{d}_k$ preserves chiral symmetry while a SO term in the plane perpendicular to the d-vector does not respect chiral symmetry.

Recently, mirror symmetry has also been a proposed as a topological protection mechanism for MFs [96]. The one-dimensional Hamiltonian Eq. (3.15) is invariant ($[\mathcal{M}, \mathcal{H}_k] = 0$) under the mirror symmetry operator $\mathcal{M} = i\hat{d}\cdot\boldsymbol{\sigma}\tau_0$. Because $\mathcal{M}$ and $\mathcal{H}_k$ commute, the Hamiltonian may be expressed in a block diagonal form where each block corresponds to a mirror eigenspace subsector. Each block is written $\boldsymbol{h}^{\pm} \cdot \boldsymbol{\sigma}$ where the $\pm$ is the mirror eigenspace index. Explicitly choosing $\hat{d}$ along $\hat{x}$ we find $\boldsymbol{h}^{\pm} = (\pm\Delta\sin(k), 0, \epsilon_k - \mu)$ such that the mirror winding number invariant in each subsector $C^{\pm}$ is defined in the $(\sigma_x - \sigma_z)$ plane. Each mirror winding curve encloses the origin once, but with opposite helicity, leading to a mirror invariant $\gamma_M = C^+ - C^- = 2$, which is illustrated in Fig. 3.9.

A realistic quasi-1D spin triplet superconductor such as LiMO (or quasi-1D TRI systems in cold fermions) may first be modeled as an array of 1D chains coupled by a weak hopping amplitude $t_y \ll t_x$. One may further consider a truly 3D system by stacking 2D arrays and coupling them through a third hopping integral $t_z \ll t_y \ll t_x$. We consider a system which consists of N_y parallel chains, indexed by $l \in [1, N_y]$,

coupled only by transverse hopping t_y. The quasi-1D Hamiltonian is a generalization of Eq. (3.15) given by

$$H^{Q1D} = \sum_{kll'} \Psi^\dagger_{kl}(\mathcal{H}^{1\mathrm{D}}_k \delta_{l,l'} + \mathcal{H}^\perp_{l,l'})\Psi_{kl'}, \tag{3.16}$$

where we have used the basis $\Psi_{kl} = (c_{kl\uparrow}, c_{kl\downarrow}, c^\dagger_{-kl\downarrow}, -c^\dagger_{-kl\uparrow})^T$, and $\mathcal{H}^\perp_{l,l'} = -t_\perp \sigma_0 \tau_z (\delta_{l,l'+1} + \delta_{l,l'-1})$.

We proceed by first examining a double chain setup with $l = 1, 2$ as an illustrative example. For a two-chain system the Hamiltonian is expressed as 2×2 matrix where every entry is itself a 4×4 matrix (see Eq. 3.15). This reads,

$$H^{\mathrm{Q1D}} = \sum_k (\Psi^\dagger_{k,1}, \Psi^\dagger_{k,2}) \begin{pmatrix} \mathcal{H}^{1D}_k & -t_\perp \sigma_0 \tau_z \\ -t_\perp \sigma_0 \tau_z & \mathcal{H}^{1D}_k \end{pmatrix} \begin{pmatrix} \Psi_{k,1} \\ \Psi_{k,2} \end{pmatrix} \tag{3.17}$$

Introducing a new Pauli matrix (ρ) in the double chain Hilbert space allows us to write Eq. (3.17) compactly as $\mathcal{H}^{1D}_k \rho_0 + t_\perp \sigma_0 \tau_z \rho_x$. Using this, we may generalize the chiral operator to the double chain space as $\mathcal{S}^{BDI} = \sigma_x \tau_y \rho_0$. We are now able to calculate a generalized multi-chain winding number W counting the number of MFs at each edge which are now localized across both chains. Just as in the single chain case, the magnitude of the chiral invariant $|W|$ is equal to the number of topologically protected MFs present at each end. This is illustrated by the phase diagram presented in Fig. 3.10 which shows that for small transverse hopping $2 \times N_y = 4$ Majorana modes are present. In general, as long as one can define a chiral and/or mirror invariant, and the transverse hopping is small enough, the number of MFs at each end grows with the size of the sample ($|W| = 2 \times N_y$).

Let us now investigate the fate of Majorana multiplets in the event of broken chiral and mirror symmetries, which may occur due to intra-chain spin-orbit coupling perpendicular to the d-vector. This modifies the Hamiltonian in Eq. (3.15) to, $\mathcal{H}^{1D}_k \mapsto \mathcal{H}^{1D}_k + \alpha_R \sin(k) \sigma_y \tau_z$ altering Eq. (3.17) accordingly. Note that while in the previous section, where we studied the topological properties of a true TR-invariant topological superconductor, spin orbit coupling did not destroy the chiral symmetry. However, we are now considering a p-wave superconductor in which the chiral symmetry is broken by any spin orbit coupling unless its orientation in spin space is parallel with the d-vector. In the two-chain problem, the two distinct sets of MKPs may interact, each hybridizing to finite energies. We note however, that the Hamiltonian (Eq. 3.17) commutes with the spatial reflection operator $\mathcal{R} = \sigma_0 \tau_0 \rho_x$ which interchanges the chain index, i.e. $\hat{c}_{k_x,1(2)} \mapsto \hat{c}_{k_x,2(1)}$. Writing Eq. (3.17) in the eigenbasis of $\mathcal{R}$ results in a block-diagonalized form which reads $\mathcal{H}^{1D}_k \rho_0 + t_\perp \sigma_0 \tau_z \rho_z$. In this form it is clear that transverse hopping only serves to modify the

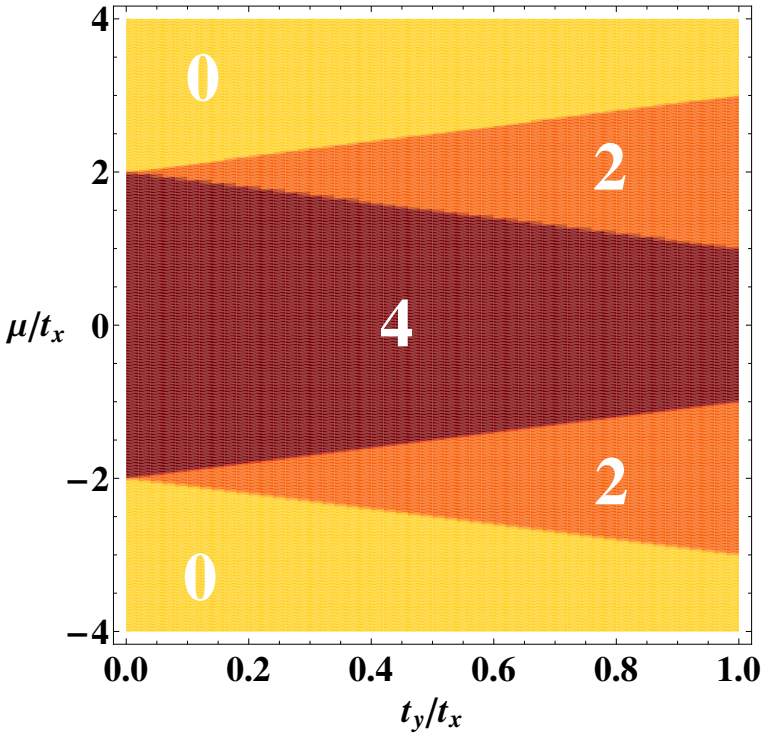

Figure 3.10: (Color online) Phase diagram for a double chain set-up of TR-invariant Kitaev system (or generic class DIII superconductors) coupled by weak transverse hopping $t_y \ll t_x$. A large range of μ accommodates the topological phase indexed by the topological invariant $|W| = 4$ which counts the number of localized Majorana modes at each end.

effective chemical potential in the two non-interacting bands. Notice also that $[\Theta, \mathcal{R}] = [\Xi, \mathcal{R}] = 0$, so that every diagonal block in the eigenbasis of $\mathcal{R}$ is particle-hole and time-reversal invariant. Because of this invariance each independent, non-interacting block constitutes a DIII topological superconductor hosting a zero energy MKP at each end. The extension of this argument to decouple N_y chains is straightforward. A generalized ρ_x is a totally symmetric $N_y \times N_y$ dimensional matrix given by $\rho_x = (\delta_{l,l'+1} + \delta_{l,l'-1})$ with $l, l' \in (1, 2, ..., N_y)$, that is, the super-diagonal and sub-diagonal elements connect nearest neighbor sites are $+1$ and all other matrix elements are zero. The eigenvalues of ρ_x come in pairs of equal magnitude and opposite sign $(\pm\lambda_1, \pm\lambda_2, \pm\lambda_3, ...)$ for N_y even and $(0, \pm\lambda_1, \pm\lambda_2, \pm\lambda_3, ...)$ when N_y is odd. In this case the rotated N_y chain Hamiltonian involves a generalized ρ_z. Because ρ_z and ρ_x have the same eigenvalue spectrum, the block diagonal Hamiltonian consists of non-interacting sectors where the chemical potential in sector is modified by $\pm\lambda_i$.

However, reflection symmetry is only approximate since some disorder will always be present in any realistic system. Therefore we add an onsite term $\delta\mu_i$, with a random magnitude within a normal distribution,

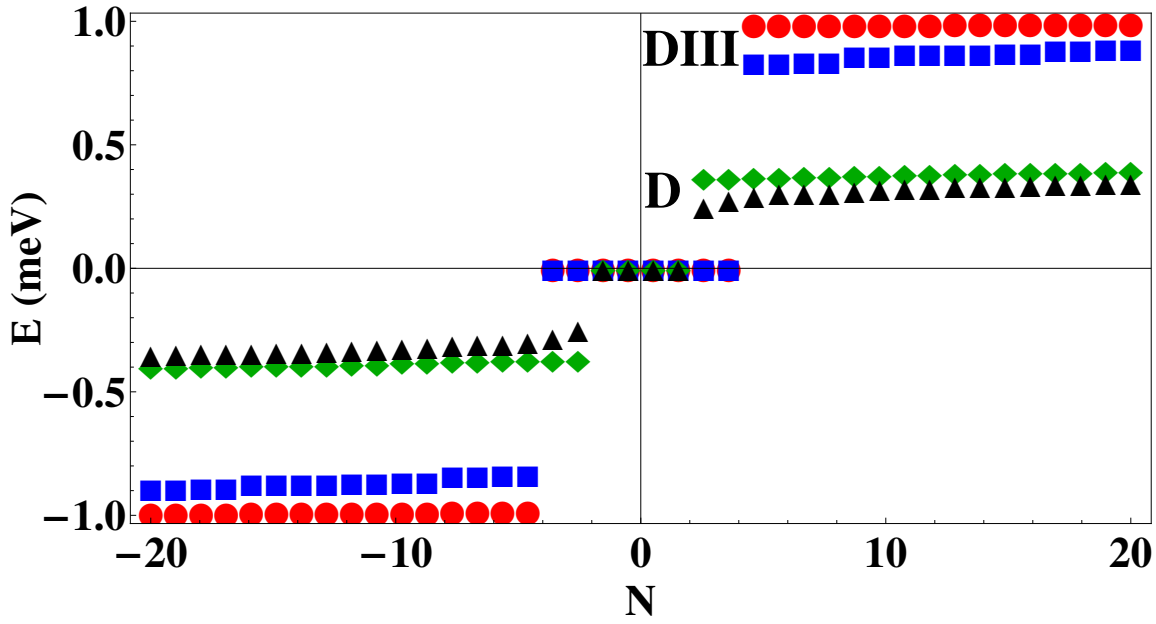

Figure 3.11: (Color online) Low energy BdG quasiparticle spectrum for TR-symmetric Kitaev system (class DIII superconductor) for $N_y = 2$ (red circles) in the absence of chiral and mirror symmetries. The eight MFs (four on each end) are protected from splitting by spatial reflection. Blue squares show same number of protected zero modes in the presence of local chemical potential disorder which breaks spatial reflection. Green diamonds and black triangles show two MFs at each end for class D, $N_y = 2$, systems with or without spatial reflection, respectively.

to the tight-binding Hamiltonian in Eq.3.14 in order to effectively model local disorder. As illustrated in Fig. 3.12, by numerically solving the BdG equations on a double chain system, we find that the presence of on-site disorder minimally affects the bulk band-structure, while the zero-energy modes are insensitive to this perturbation. Note that the Majorana multiplets persist even in the absence of chiral, mirror, and reflection symmetries, all of which are now explicitly broken. We get similar results even for $N_y > 2$, and the number of Majorana multiplets scale with the number of chains in the transverse direction.

In order to understand the response of the MFs to reflection breaking perturbations we consider first the two-chain Hamiltonian describing the chemical potential imbalance written as,

$$H_k^{Q1D} = \begin{pmatrix} \mathcal{H}_k^{1D} + \delta & -t_\perp \\ -t_\perp & \mathcal{H}_k^{1D} - \delta \end{pmatrix} \tag{3.18}$$

where $t_\perp$ is understood to be $t_\perp \sigma_0 \tau_z$, $\delta = \delta\mu\sigma_0\tau_z$, and we continue to work in the $(\Psi_{k,1}^\dagger, \Psi_{k,2}^\dagger)$ basis. Note that we still consider $k = k_x$ to be a good quantum number and break reflection symmetry only by introducing

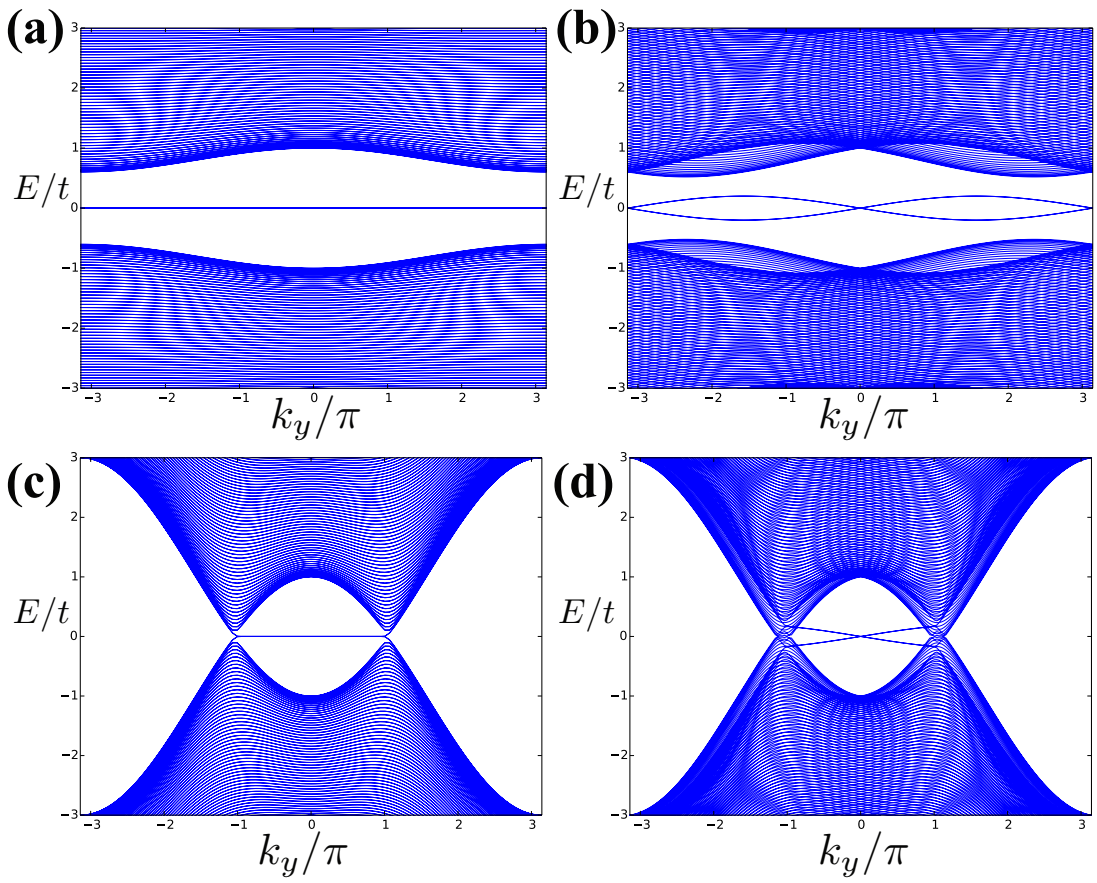

Figure 3.12: (Color online) Effects of reflection symmetry breaking on the two dimensional band-structure. We have taken periodic boundary conditions along the y-direction and open boundary conditions along x. (a) In the presence of reflection symmetry, and one of chiral or time-reversal symmetries, a highly degenerate Majorana flat-band emerges if the transverse hopping is small (i.e. $t_y \ll t_x$). (b) Reflection symmetry breaking by the addition of a transverse ($\alpha \sin(k_y)$) Rashba type spin-orbit coupling term splits the Majorana band at all k_y except the TR-invariant momenta $k_y = 0, \pi$. (c) Uniform hopping $t_y = t_x$ gaps out most of the flat-band except for the states near the origin in momentum space. (d) A single degenerate point remains in the presence of uniform hopping and transverse spin-orbit coupling.

a chemical potential imbalance among the chains. The question is now the following: Can we systematically block-diagonalize this Hamiltonian with a unitary eigenvalue-conserving transformation that commutes with time reversal and particle-hole symmetries? If yes, MFs will persist in each block due to a 'hidden symmetry' associated with this transformation. Since ${\mathcal{H}_k}^{1D}$ appears with an identity matrix in chain space, this problem amounts to finding a matrix which diagonalizes the remaining terms leaving ${\mathcal{H}_k}^{1D}$ invariant.

We search for a hidden unitary transformation in a systematic way by first considering the eigen-decomposed form of the non-diagonal terms in Eq. (3.18), which we call $A = \delta\rho_z - t_\perp\rho_x$. This is expressed

as $A = Q\Lambda Q^{-1}$, where Q is a matrix whose columns are the eigenvectors of A,

$$\boldsymbol{v}_{\pm} = 1/(\sqrt{2}N_{\pm}) \left(-(\delta \pm \sqrt{t_{\perp}^2 + \delta^2})/t_{\perp}, 1 \right)^T$$

and $N_{\pm} = \sqrt{1 + \frac{\delta^2}{t^2} \pm \frac{\delta\sqrt{t^2+\delta^2}}{t^2}}$ is the normalization constant. Also remember that each entry in Q involves an identity in spin and particle-hole spaces. The unitarity of Q is a direct consequence of the Hermiticity of A. Note that in the limit $\delta \to 0$, this reduces to the eigenbasis of $\mathcal{R}$ which was the reflection transformation operator used in the presence of $\mathcal{R}$. Rotating the full 8×8 Hamiltonian in Eq. (3.18) by the Q operator we see $Q^{-1}H_k^{Q1D}Q = [-(\epsilon_k - \mu)\sigma_0\tau_x + \alpha_k^R\sigma_y\tau_z + \Delta\sigma_x\tau_x]\rho_0 - \sqrt{t_{\perp}^2 + \delta\mu^2}\sigma_0\tau_z\rho_z$. The transformed Hamiltonian consists of two non-interacting topological DIII sectors, each block respecting both particle-hole and time reversal symmetries, subject to a modified chemical potential of magnitude $\sqrt{t_{\perp}^2 + \delta^2}$ and a sign change for the single particle kinetic energy. The commuting hidden symmetry operator associated with the Q transformation is $R^{'} = \left(1 + \frac{\delta\mu^2}{t_{\perp}{}^2}\right)^{-1/2} \left(\rho_x - \frac{\delta\mu}{t}\rho_z\right)$. This explains why the multiple MKPs with spatially overlapping wave functions persist even with broken reflection symmetry, as shown in Fig. 3.12 (but only as long as k_x is a good quantum

3.5 Conclusion

In summary we show that the pair of MFs at each end of a 1D TR symmetric Kitaev p-wave chain are topologically robust to a large number of perturbations including those breaking TR symmetry. We identify the appropriate topological class to be BDI with an integer ($\mathbb{Z}$) invariant the value of which gives the number of topologically protected MFs at each end. In addition to the topological properties of the TR-symmetric Kitaev chains, our results establish the organic superconductors $(TMTSF)_2X$ (X=PF_6, ClO_4) and $Li_{0.9}Mo_6O_{17}$, which have been proposed [70, 71, 72] to be quasi-1D equal-spin-pairing p-wave superconductors, as suitable platforms for experimental studies of MFs. Apart from explaining the anomalous magnetic field response of all the DIII class systems proposed in the literature [85, 86, 87, 89, 88, 90, 91] we provide a realistic route to engineer a "true" TRI TS system whose Majorana Kramers pairs are split by a Zeeman field applied in *any* direction. In this system, and quite generally in TRI superconductors, we prove that the splitting of the MKPs is highly anisotropic in spin space. Furthermore, we show that spatial reflection symmetry further protects the Majorana modes from hybridizing which can even lead to a highly degenerate Majorana flat-band in certain circumstances. Differential conductance experiments in the presence of a variable magnetic field,

as seen in Ref. 58, could directly probe this remarkable phenomena. Platforms potentially exhibiting TRI topological superconductivity, with or without chiral symmetry, include pnictide based $s_{\pm}$-wave nanowire heterostructures [88] and some naturally occurring quasi-1D organic superconductors [97].

Chapter 4

Majorana Bound States in Chiral Ferromagnetic Nanowires

In the previous chapter we analyzed the conditions under which Majorana bound states (MBSs) cab exist in topological superconductors in the presence of magnetic fields. In this chapter we will analyze the differential conductance signatures of a new experimental system to which our model is directly applicable. In this recent experiment zero-bias peaks have been observed in scanning tunneling microscopy (STM) experiments performed on chains of magnetic atoms on a superconductor, we show that a multichannel ferromagnetic wire deposited on a spin-orbit coupled superconducting substrate can realize a non-trivial chiral topological superconducting state with Majorana bound states localized at the wire ends. The non-trivial topological state occurs for generic parameters requiring no fine tuning. We theoretically obtain the signatures which appear in the presence of an arbitrary number of Majorana modes in multi-wire systems incorporating the role of finite temperature, finite potential barrier at the STM tip, and finite wire length. These signatures are presented in terms of spatial profiles of STM differential conductance which clearly reveal zero energy Majorana end modes and the prediction of a multiple Majorana based fractional Josephson effect. A critical comparison of our results with the experimental data shows a basic inconsistency in the interpretation of the Fe nanowire STM experiment in terms of Majorana zero modes– in particular, the observation of the precise localization of the Majorana zero modes at the wire ends cannot be reconciled with the extremely small topological superconducting gap (and the associated extremely weak Majorana tunneling peak) observed simultaneously. Other than this incompatibility most other aspects of the experimental phenomenology are

reasonably well explained by our theory.

4.1 Introduction

Very recent experimental work [98] suggests that atomic scale ferromagnetic Fe nanowires on the [110] surface of superconducting Pb may support Majorana modes and topological superconductivity. Extensive earlier theoretical work suggested several different mechanisms which could lead to MBS-carrying TS in magnetic nanowires placed on superconducting substrates. The earliest such mechanisms [99, 100, 101] modeled the nanowire as a chain of magnetic impurities in a spin-spiral phase. The spin-spiral, following previous work [102], is used to mimic an effective spin-orbit coupling that would in turn lead to an effective triplet pairing superconducting proximity effect from the singlet superconducting substrate, exactly as in the existing semiconductor nanowire models of topological superconductivity [19, 24, 25]. The magnetic impurities were suggested to generate an array of Yu-Shiba-Rusinov (YSR) [103, 104, 105] bound states in the superconductor. The combined effect of the superconductivity and spin-texture leads to an effective Kitaev nanowire model [36] that can support Majorana bound states under appropriate conditions [99, 100, 101]. However, the theoretical plausibility of creating such a spin-spiral phase[106, 107] was debated, and it was shown that such spin spirals are unstable toward the formation of purely ferromagnetic or antiferromagnetic phases [108].

The absence of a spin-spiral in the experimental system has led to the conjecture of an alternative mechanism involving the strong spin-orbit coupling of the Pb superconducting substrate itself contributing to topological superconductivity in the magnetic nanowire [108]. The basic model, which has been studied in this context by several authors [98, 109], proposes that only the spin-triplet component of Cooper pairing, *if any*, may be proximity-induced in a ferromagnetic wire from a spin-orbit coupled superconductor. This mechanism has previously been proposed as an approach to topological superconductivity [110] and also been invoked [111] to explain the long-range proximity-effect observed through ferromagnetic nanowires [112]. The mechanism of triplet proximity effect on a ferromagnetic wire arising from a spin-orbit coupled superconducting substrate has been studied in detail by three of us recently and shown to potentially support MBS-carrying topological superconductivity in the BDI chiral symmetry class [113]. Such a symmetry would suggest unsplit Majorana modes whenever the effective chemical potential in the ferromagnetic wire is positive.

In this context, it may be useful, particularly for later discussion of the experimental results [98], to

distinguish two complementary and distinct theoretical models for topological superconductivity and Majorana bound states in a one-dimensional (or quasi-one-dimensional) ferromagnetic nanowire (Fe in Ref. 98) lying on a two-dimensional surface of an underlying superconductor (Pb in Ref. 98). One model, which we refer to as the Shiba model (or Shiba chain model), discussed in Refs. 100 and 109 respectively for the helical and the ferromagnetic magnetic order in the wire, describes the magnetic atoms (Fe in Ref. 98) as essentially independent quenched classical magnetic impurities with little direct inter-atomic hopping along the chain, i.e. the one-dimensional band width of the chain is basically zero (or equivalently, vanishing inter-atomic hopping amplitude t). The other model, which we refer to as the nanowire (or simply, the wire) model, introduced in Ref. 113 for the ferromagnetic order in the magnetic chain, describes the ferromagnetic chain as strongly directly tunnel-coupled along the chain with considerable inter-atom hopping leading to one-dimensional bands of fairly large band-widths (or equivalently, large inter-atomic hopping amplitude t). These two models have been recently introduced and studied in the context of a ferromagnetic chain on a superconductor (i.e. the experimental system of Ref. 98) in Refs. 109 and 113 respectively, where it has been explicitly pointed out that the models are complementary, and depending on the nature of the ferromagnetic chain (i.e. whether there is or is not considerable hopping which is defined simply by whether the inter-atomic hopping energy along the chain is smaller or larger than the superconducting gap in the substrate superconductor) one or the other model will apply, and by definition, there cannot be a situation where both models apply simultaneously. The accompanying band structure calculations for the Fe chain on Pb presented in the experimental work [98] clearly show that the hoping term on the chain t is of the order of eV whereas the superconducting gap in Pb is of course of the order of meV. Therefore, the system studied in Ref. 98 is deep inside the nanowire regime very far from the Shiba model. To apply the Shiba model to the experimental situation of Ref. 98, one will have to assume absurd superconducting gaps of eV size (with superconducting critical temperatures which would be $> 10^4$ Kelvins!). Thus, we present all our results using the nanowire model introduced in Ref. 113, and not the Shiba chain model discussed in Refs. 100 and 109. The reason we are emphasizing this seemingly simple conceptual point is that Ref. 98 has a confusing interpretation of the experimental data presented therein, where depending on different aspects of the data, the theory used in Ref. 98 has randomly varied between the Shiba model and the nanowire model, which are, as described above, completely incompatible with each other. This is the same incompatibility alluded to in the abstract of our paper– in particular, we find that there is simply no way one can understand and interpret all aspects of the observations presented in Ref. 98 using one coherent theoretical approach. Obviously, the Shiba model has no place in the analysis of the experiment in Ref. 98 since the inter-atomic hopping energy along the Fe

chain is thousands of times larger than the superconducting gap of Pb. As we discuss later in this work, this fundamental inconsistency between different aspects of the results presented in Ref. 98 remains unresolved with the reported induced topological gap being $10^{-4}eV$ and the observed strong lattice-level, $< 5\ nm$, localization of the Majorana mode requiring an estimated superconducting gap of $\sim 1eV$. This basic incompatible dichotomy must be resolved before the observations of Ref. 98 can be considered to be evidence for the existence of localized MBS in the Fe/Pb hybrid system.

The current work is an extension of Ref. 113 carried out in the context of the putative experimental MBS observation claimed in Ref. 98 in order to provide a detailed critical comparison between theory and experiment, which is necessary since the rather strong claim of a direct observation of Majorana modes must be thoroughly validated from all possible perspectives. It may be useful in this context to emphasize that the recent spurt in the experimental MBS activity, including both the earlier work on semiconductor (InSb and InAs) nanowires [58, 60, 61, 59, 62, 63] and the very recent work on Fe nanowires[98], is completely dependent on theoretical predictions and analyses for its validation since the observations themselves involving tiny zero-bias tunneling conductance peaks at low temperatures in rather complex hybrid systems are remarkably unremarkable, becoming noteworthy only because theories specifically predicted that such zero-bias tunneling peaks should exist in these specific hybrid structures as MBS signatures. In particular, Ref. 19 not only predicted the existence of the Majorana bound states in semiconductor-superconductor hybrid structures, specifically laying out the type of structures (and the materials) experiments should use, but also carried out realistic calculations showing that the resulting MBS-induced zero-bias tunneling peaks should have a small height (because of finite temperatures, tunnel barrier heights, and wire lengths) compared to the expected quantized value [114] associated with the perfect Andreev reflection anticipated for MBSs. This early paper[19] also specifically suggested the use of STM in order to look for topological zero energy Majorana excitations in hybrid systems as has eventually been accomplished in Ref. 98.

While topological superconductivity in the chiral symmetry class has been established for ferromagnetic wires with a single spatial orbital per atom, the number of Majorana modes arising from such a model is limited to two. On the other hand, the band-structure calculation for the experimentally realistic system [98] suggests that the number of channels in the wire can be significantly enhanced by the presence of multiple orbitals per atom and multiple atoms along the diameter of the chain. In this work, we consider a multichannel generalization of the FM heterostructure and its topological properties starting from the nanowire model of Ref. 113. Non-trivial zero-bias phenomena appear across a broad range of parameters in contrast to the fine tuning necessary for a non-trivial topological phase in class D [17, 115, 19, 24, 25] or

DIII systems [94, 85, 86, 87, 88, 89, 90, 91, 92, 116]. Within this framework, manipulating the system width (i.e. coupling parallel magnetic chains) enhances or reduces the zero-bias conductance peak (ZBCP) height accordingly. Manipulation of the zero-bias conductivity tuned by the width of the magnetic chain would be a direct signature of the chiral class BDI topological superconductors. Additionally, we calculate spatially resolved scanning tunneling conductance profiles including effects of finite temperature and finite size of the wire (as well as the finite tunnel barrier effects) which are experimentally accessible by scanning tunneling microscopy (STM). Finally, we show that the fractional Josephson effect maintains its 4π periodicity in phases supporting multiple spatially overlapping MBSs and comment on how the Josephson current may be enhanced in the presence of Majorana multiplets [36, 24].

It may be useful to point out the connection between MBS in much-studied semiconductor nanowire systems with that in the new platform of interest in Ref. 98 involving ferromagnetic nanowires. Although it may appear at first sight that the two systems are completely distinct, from a theoretical perspective the MBS in the ferromagnetic wires are described by essentially the same theory as developed earlier for the semiconductor nanowires in Refs.19, 24, 25, provided that one is in the nanowire limit of large inter-atomic hopping along the chain (and not in the Shiba limit), and that one is in the limit of the spin splitting (induced in the semiconductor case by an external magnetic field or by a proximate exchange splitting) being very large (much larger than the other energy scales in the problem including the spin-orbit coupling energy, the Fermi energy, and the superconducting gap in the ferromagnetic wire case). In this large spin-splitting limit, the semiconductor system is also essentially an effective "half-metallic ferromagnet" exactly as the Fe wire studied in Ref. 98 is claimed to be. In the semiconductor nanowire case also, the topological superconducting phase will be generic in this very large spin-splitting limit since the chemical potential would by definition be in the single spin polarized subband, with the superconducting gap being smaller than the spin splitting. Thus, the distinction made between semiconductor nanowires and magnetic nanowires with respect to topological superconductivity is a distinction without much difference, since one can take the existing theory for the semiconductor nanowire and obtain all the necessary formula for the ferromagnetic wire case by assuming the spin-splitting to be by far the largest energy scale.

We emphasize that the precise theoretical analogy between the semiconductor nanowire and the ferromagnetic nanowire applies only in the case of large hopping between the magnetic atoms along the chain. In the opposite case of a Shiba chain with essentially vanishing hopping, the ferromagnetic system is qualitatively different from the semiconductor system, requiring extreme fine-tuning to obtain the topological superconductivity as studied in Refs. 100, 113. This is not studied at all in the current work since it is clear

based on band structure calculations that the system of Ref. 98 is in the nanowire (and not the Shiba) regime.

4.2 Experimental Setup and Theoretical Model

Taken very close to a sample surface, an STM can be used as an electrode to measure transport properties. A movable scanning point contact tunneling experiment is potentially very useful in investigating the edge character of Majorana zero modes since the STM is particularly well-suited in measuring the local density of states. This idea, originally proposed in Ref.19, is rather impressively implemented in the highly demanding measurements presented in Ref. 98. Provided the electrical contact is good between the ferromagnet (Fe nanowire) and the superconducting substrate (Pb), Cooper pairs will leak into the ferromagnet, thereby proximity inducing superconductivity in the nanowire. We model a finite quantum wire with dimensions $L_y \ll L_x \equiv L$ by considering a $N_x \times N_y$ site square lattice with unit spacing. The effective Hamiltonian for the topological superconductor is $H_{TS} = H_t + H_\Delta^{S=0} + H_\Delta^{S=1} + H_Z$ where

$$\begin{aligned} H_t &= \sum_{\langle ij\rangle\sigma} t\left[c_{i\sigma}^\dagger c_{j\sigma} + \text{H.c.}\right] - \sum_{j\sigma}\mu_j c_{j\sigma}^\dagger c_{j\sigma} \\ H_\Delta^{S=0} &= \sum_j \Delta_s c_{j\uparrow}^\dagger c_{j\downarrow}^\dagger + \text{H.c} \\ H_\Delta^{S=1} &= \sum_{j\sigma} i\Delta_p (c_{j\uparrow}^\dagger c_{j+1\uparrow}^\dagger - c_{j\downarrow}^\dagger c_{j+1\downarrow}^\dagger) + \text{H.c} \\ H_Z &= \sum_{j\sigma\sigma'} c_{j\sigma}^\dagger (\boldsymbol{V}\cdot\boldsymbol{\sigma})_{\sigma\sigma'} c_{j\sigma'} \end{aligned} \tag{4.1}$$

Here $c_j^\dagger$ is the electronic creation operator for site j, $\langle ij\rangle$ indicates nearest neighbor sites, $\boldsymbol{\sigma} = (\sigma_x, \sigma_y, \sigma_z)$ is the vector of Pauli matrices, t is the hopping amplitude in the nanowire, and μ is the chemical potential. The superconducting pairing is a mixture of singlet and triplet terms. For the triplet pair potential term we have taken a Cooper pairing with spin projection $S_x = 0$, which is the familiar equal-spin-pairing $\Delta_{\downarrow\downarrow} = -\Delta_{\uparrow\uparrow}$. The Zeeman spin-splitting due to an internal magnetization in the ferromagnet is $\boldsymbol{M}$ is $\boldsymbol{V} = g\mu_B \boldsymbol{M} = (V_x, V_y, V_z)$ where g and μ_B are the Lande g-factor and Bohr magneton respectively. We note that our effective Hamiltonian, as given in Eq. 4.1, describes the TS phase of the ferromagnetic nanowire assuming that the degrees of freedom of the underlying superconducting substrate (Pb in Ref. 98) have been integrated away with Eq. 4.1 now describing only the electrons in the Fe magnetic wire. We refer to Ref. 113 for the details on how to obtain Eq. 4.1 which is our starting point in the current work. We note that in this

context our effective model, derived from Ref. 113 which should be consulted for the details, describes only the ferromagnetic nanowire, hiding all information about the underlying superconducting substrate with the parameters for the spin-orbit coupling, the bulk superconducting gap of the substrate, the hopping amplitude of Cooper pairs between the substrate and the nanowire inducing the singlet and triplet proximity effect, etc. being implicitly contained in the induced superconducting pair potentials Δ_s and Δ_p, which we use as phenomenological parameters to be obtained from the experimental measurements themselves. Our goal here is to obtain the phenomenological consequences of the minimal topological nanowire model (i.e. Eq. 4.1) for the ferromagnet/superconductor hybrid system to make observable predictions and to carry out comparison with the existing data. We also ignore all nonessential complications such as the number of orbitals per Fe atom and the effective width of the wire, and so on which can be absorbed in the multichannel generalization we consider below (i.e. the W-parameter denoting the number of active wire channels as described below). Our goal here is to utilize the minimal model and work out its implications in great details. Our Eq. 4.1 serves as the minimal model for the experimental system of Ref. 98 in the current work.

Throughout this work we fix all of our parameters relative to the hopping integral t in the nanowire. To begin and to establish our general results, we use $\Delta_s = \Delta_p = t/10$, $\boldsymbol{V} = V_z = 2.0t, L = 100$ while W (the number of transverse channels) and the chemical potential μ are allowed to vary. For simplicity and numerical convenience, we will choose $\Delta_s = \Delta_p$. Choosing two such values $\Delta_s = \Delta_p = 0.1t$ and $\Delta_s = \Delta_p = 0.01t$ (both of which are several orders of magnitude larger than reported in Ref. 98) will allow us to estimate the order of magnitude of parameters such as the Majorana decay length (see Fig. 4.5). A discussion concerning experimentally realistic parameters and their effect on the measured tunneling conductance is left to a later section. We note that this choice of generic parameters incorporates the half-metallic character of the ferromagnetic wire since only one spin subband is occupied for a large range of chemical potential values keeping the system in the topological phase without any additional fine-tuning of parameters. Solving Eq. 4.1 directly numerically we find zero energy Majorana states which are localized at each end of the wire. The evolution of the low energy spectrum as a function of the chemical potential, as well as a function of the number of zero energy modes, is presented in the bottom panel of Fig. 4.2. To understand how Eq. 4.1 realizes an integer number of Majorana zero modes we analyze the topological properties of this model.

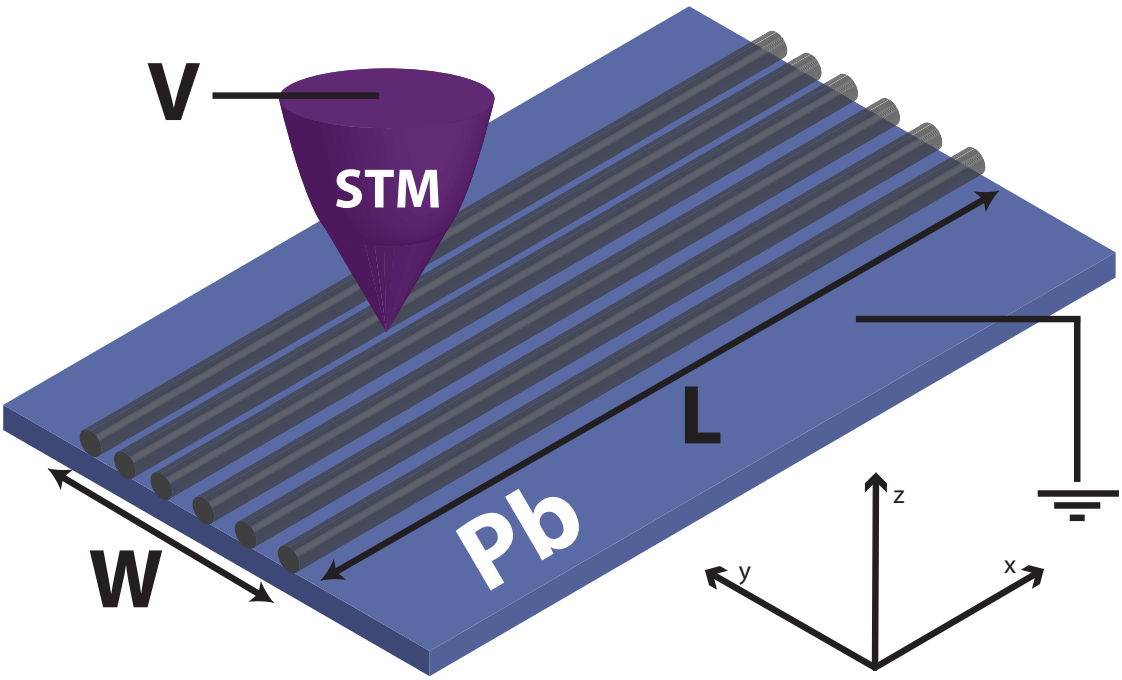

Figure 4.1: (Color online) a) Schematic diagram of the proposed heterostructure involving a series of ferromagnetic quantum wires (gray), with large intrinsic magnetization M, deposited on top of a spin-orbit coupled s-wave superconductor such as lead (blue substrate). Spin singlet and triplet pairing potentials are proximity induced in the FM wires due to the strong spin orbit coupling and inter-orbital mixing in the superconductor. A STM probe, at coordinate x, measures the spatial dependence of the differential conductance along the longitudinal axis.

4.3 Topological Properties and Quantum Phase Transitions

According to the Altland-Zirnbauer classification scheme[117], free fermion systems are characterized by their dimensionality as well as by the presence and the sign of anti-unitary symmetries. There are ten topological classes in total and five of them are non-trivial (i.e. a non-trivial topological invariant can be defined) for a given dimension. The two anti-unitary symmetries used are time-reversal symmetry (TRS) and particle-hole symmetry (PHS), with the latter often being referred to as charge conjugation symmetry. Denoting the TRS and the PHS operators by Θ and Ξ respectively, the anti-unitary symmetries are present when the following reality conditions are satisfied: $\Theta H \Theta^{-1} = U_\Theta H^* U_\Theta^\dagger = +H$ and $\Xi H \Xi^{-1} = U_\Xi H^* U_\Xi^\dagger = -H$. Here $U_{\Theta,\Xi}$ denote the unitary part of the TR and PH operators. A system is chiral invariant (or sublattice symmetric) when both TR and PH are present and is given by the unitary operator $\mathcal{S} = \Theta \cdot \Xi$. The classification triplet $(T, C, S) = (\Theta^2, \Xi^2, \mathcal{S}^2)$ is used to index each symmetry class, where the TR and PH operators can square to ± 1 and the chiral operators is restricted to $\mathcal{S}^2 = +1$. We write $\mathcal{O}^2 = 0$ if an operator is not

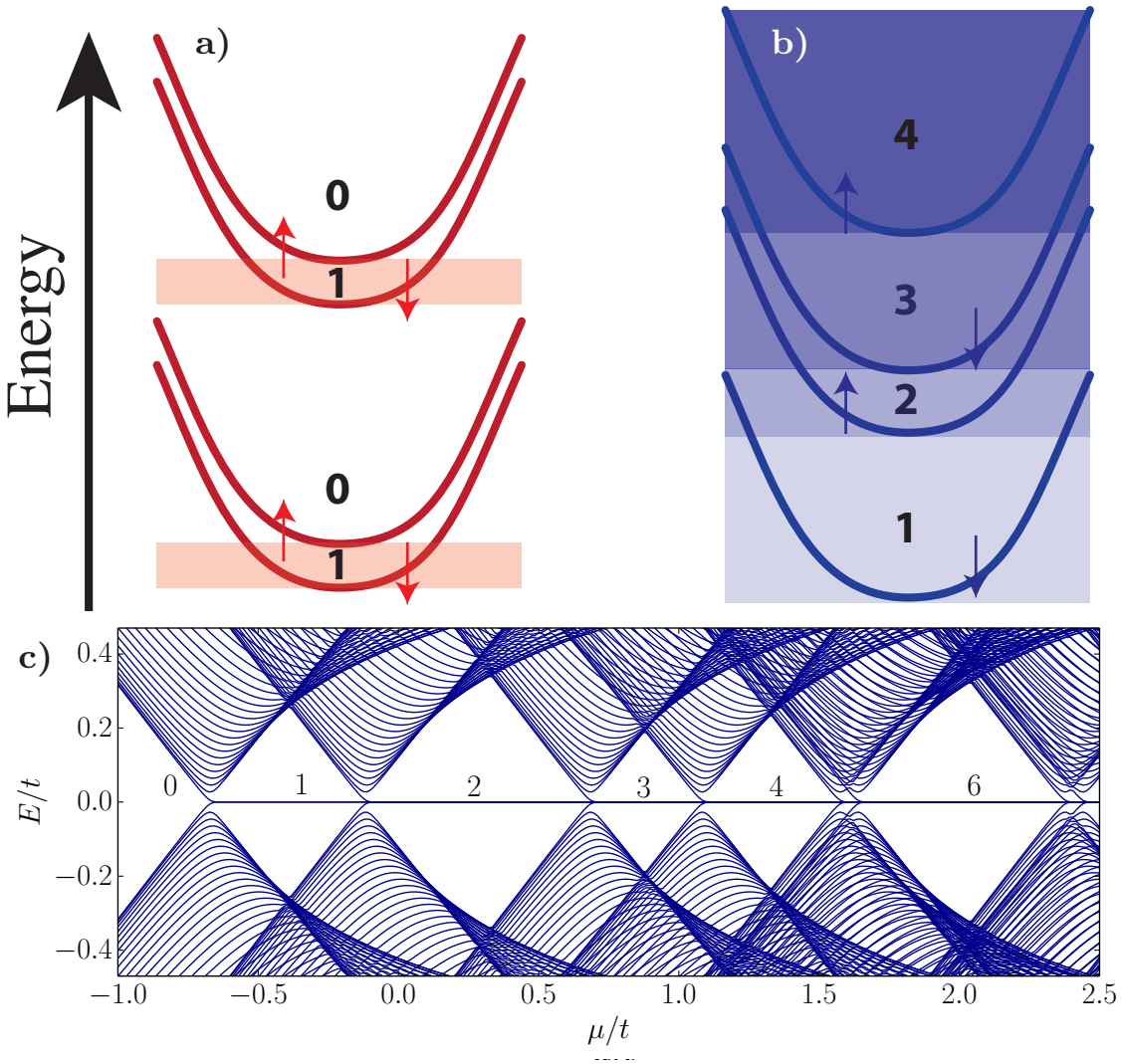

Figure 4.2: (Color online) Comparison of the topological properties of the class D spin-orbit coupled semiconducting nanowire (red) and our ferromagnetic system (blue). In panel (a) an externally applied magnetic field induces a Zeeman splitting between the originally degenerate spin bands. This system is topological non-trivial if an odd number of bands is occupied and Cooper pairs are supplied by a nearby superconductor. When the Fermi energy lies in the shaded region, the class D $\mathbb{Z}_2$ invariant non-trivial and a single Majorana bound state emerges at each end. b) Normal state band structure for a multichannel ferromagnetic wire (see Fig. 4.1). In the presence of proximity induced p-wave pairing, the FM is promoted to the topological class BDI, which is characterized by a non-trivial $\mathbb{Z}$ invariant for generic band occupancy. Additionally, the large intrinsic magnetization provides a broad non-trivial parameter regime in which a non-trivial topological state persists even if the chiral symmetry is broken, say, by a second Zeeman field perpendicular to the magnetization (BDI $\rightarrow$ D). In this case, the shaded regions with an odd $\mathbb{Z}$ invariant remain non-trivial while the others become trivial. (c) Low energy quasiparticle spectrum as a function of the chemical potential in the ferromagnetic wire. As μ increases, the number of Majorana zero modes at each end of the FM wire increases by one following each gap closing.

present.

Invariants are generally formulated in terms of the bulk Hamiltonian's topology, so we now look at a strictly 1D version of H_{TS}. Fourier transforming Eq. 4.1 with a single spatial channel (i.e. no transverse hopping), the momentum space Bogoliubov-de Gennes (BdG) Hamiltonian becomes $H = \sum_k \Psi_k^\dagger H(k) \Psi_k$ where

$$\begin{aligned} H(k) &= (-2t\cos(k) - \mu)\sigma_0\tau_z \\ &+ [\Delta_s\sigma_0 + \Delta_p \sin(k)\boldsymbol{d}\cdot\boldsymbol{\sigma}]\,\tau_x \\ &+ \boldsymbol{V}\cdot\boldsymbol{\sigma}\tau_0. \end{aligned} \tag{4.2}$$

Here $k \equiv k_x$ is the one-dimensional crystal momentum and $\Psi_k = (c_{k\uparrow}, c_{k\downarrow}, c^\dagger_{-k\downarrow}, -c^\dagger_{-k\uparrow})^T$ is our four component Nambu spinor which acts on the particle-hole ($\boldsymbol{\tau}$) and spin spaces ($\boldsymbol{\sigma}$). In our calculations we use $\boldsymbol{d} = (1,0,0), \boldsymbol{V} = (0,1,0)$ but leave $\boldsymbol{d}, \boldsymbol{V}$ in Eq. 4.3 to highlight the generic properties of the various symmetry classes. Given our choice of basis, the anti-unitary TR and PH operators have the matrix structure $\Theta = i\sigma_y\tau_0\mathcal{K}$ and $\Xi = \sigma_y\tau_y\mathcal{K}$ where $\mathcal{K}$ is the complex conjugation operator.

In momentum space, the reality conditions for Bloch Hamiltonians are [118]

$$\begin{aligned} \Theta H(k)\Theta^{-1} &= +H(-k) \\ \Xi H(k)\Xi^{-1} &= -H(-k). \end{aligned} \tag{4.3}$$

PH symmetry emerges from the BCS mean-field theory and is intrinsic to all BdG Hamiltonians, so in the absence of any additional symmetries $(T, C, S) = (0, 1, 0)$. This triplet corresponds to the topological class D, which is characterized by a $\mathbb{Z}_2$ topological invariant in $d = 1$. Recall, $\mathbb{Z}_2 \equiv \mathbb{Z}/2\mathbb{Z}$ is the cyclic quotient group with two elements $\{0, 1\}$. The topological invariant for class D systems is given by Kitaev's Majorana number, which is defined as [36] $\mathcal{M} = \text{sgn}\left[Pf(\widetilde{A}(0))Pf(\widetilde{A}(\pi))\right]$ where $\widetilde{A}$ is the momentum space Hamiltonian written in a skew symmetric form, determines when the system is topologically non-trivial. The spin-orbit coupled semiconductor-superconductor heterostructure proposal[17, 115, 19, 24, 25], which aims to replicate the physics of Kitaev's spinless superconductor belongs to the topological class D for the most general types of spin-orbit coupling. However, the specific models studied in the original proposals[17, 115, 19, 24, 25], assumed that the spin-orbit direction was perpendicular to the Zeeman coupling. These models are in a more restricted BDI class that will be discussed further at the end of this section because of its relevance to the

ferromagnetic wire model. In this system, a Zeeman field splits degenerate spin-orbit coupled bands. The goal of this splitting is to remove a single Fermi surface thus rendering the system effectively spinless. Typically, the Zeeman splitting is small compared to the bandwidth, resulting in a small non-trivial topological parameter range (see Fig. 4.2). In this case, the difficult task of fine tuning the chemical potential, by using gate electrodes for example [58, 60, 61, 59, 62, 63], may be necessary to achieve a non-trivial topological state if the chemical potential lies near half filling for a subband. As emphasized at the end of the Introduction, however, we are free to take the very large spin-splitting (i.e. very large V_z) limit of the semiconductor model (although this would not be a particularly physically relevant model for semiconductors per se, it is a perfectly allowed theoretical limit), which then coincides with the current ferromagnetic wire situation of interest to the experimental system in Ref. 98.

If Zeeman splitting is absent in Eq. 4.3, then the first reality condition from Eq. 4.3 is satisfied. Using $\Theta = i\sigma_y\tau_0\mathcal{K}$ we see that $T = -1$ so a class DIII TR invariant system is characterized by the triplet $(T, C, S) = (-1, 1, 1)$. Class DIII is characterized by a $\mathbb{Z}_2$ topological index which is related to a Kramers polarization [119] similar to the way the class D invariant is related to the electric polarization of the wire [118]. If H belongs to this class hybridization between time-reversed Majorana zero modes is forbidden by Kramers degeneracy and each end of the wire hosts a perfectly degenerate Majorana Kramers pair.

In addition to the two classes discussed above, superconducting systems can belong to the topological class BDI. Note that there exists the chiral operator $\mathcal{S} = \hat{d} \cdot \boldsymbol{\sigma}\tau_y$ which anti-commutes with the Hamiltonian in Eq. 4.3; note in the TR invariant case the chiral operator is $\mathcal{S}_{DIII} = \sigma_0\tau_y$. This unitary chiral operator must be a product of two anti-unitary operators, one of which is Ξ. By simple algebra, one can show that our missing operator is $\mathcal{O} = (\hat{d} \cdot \hat{y} + i(\hat{d} \times \hat{y}) \cdot \boldsymbol{\sigma})\mathcal{K}$ so that $\mathcal{O}^2 = 1$ (i.e. $T = +1$) and that $H(k)$ satisfies $\mathcal{O}H(k)\mathcal{O}^{-1} = +H(-k)$. We continue to call this operator $\mathcal{O}$, even though it leads to the same reality condition as Θ, in order to distinguish it from the usual time reversal symmetry. A crucial difference between classes BDI and D/DIII is that the former is characterized by an integer $\mathbb{Z}$ invariant. Because the invariant can take any integer value, multiple spatially overlapping MBSs can coexist in contrast to class D systems where localized zero-energy anyonic MBSs hybridize into conventional finite-energy fermionic quasiparticle states. As illustrated in Fig.4.2 panel (b), a BDI chiral system is non-trivial for a generic parameter range. We numerically diagonalize and plot the low energy quasiparticle spectrum for H_{TS} as a function chemical potential in Fig4.2 panel (c). The Majorana occupancy grows when μ increases and successive higher energy bands are occupied. Therefore for any generic chemical potential one expects a non-trivial topological state with end-localized zero energy MBSs.

Composing the two reality conditions in Eq. 4.3 we see that the chiral operator satisfies $\{\mathcal{S}, H(k)\} = 0$. This anti-commutation relation implies that in the eigenbasis of $\mathcal{S}$ the Hamiltonian is off-diagonal,

$$H'(k) = \begin{pmatrix} 0 & A(k) \\ A^{\dagger}(k) & 0 \end{pmatrix} \tag{4.4}$$

Here we have used U to represent the unitary transformation matrix between the original and the chiral basis. For a single channel $A(k)$ is a 2×2 complex Hermitian matrix whose determinant $D(k) \equiv Det(A(k))$ is generally complex. Obviously the complex phase $\exp[i\theta(k)] = D(k)/|D(k)|$ lies on the unit circle and we have established a mapping from the Brillouin zone (S^1 in 1D) to $U(1)$. The fundamental group $\pi_1(U(1)) = \mathbb{Z}$ is well defined here so that we may write the topological winding invariant as [120],

$$\mathcal{W} = \frac{1}{2\pi} \int_0^{2\pi} \arg D(k) dk. \tag{4.5}$$

The integer $\mathcal{W}$ counts the number of times the complex argument $\theta(k)$ winds about the origin in the complex plane and is invariant under smooth deformations. In other words, $\mathcal{W}$ can change only if the winding curve $D(k)$ passes through the origin. However, by looking at the from of Eq. 4.4 we know that the k-point where $D(k)$ vanishes constitutes a gap closing and a concomitant topological quantum phase transition. Note that the DIII chiral operator is odd under time-reversal symmetry, $\{\mathcal{S}_{DIII}, \Theta\} = 0$ which implies that the end modes with chiral charge $+1$ are compensated for by an equal number of modes with charge -1. Therefore, while this procedure may be mathematically well defined, it is trivial in the sense that the net DIII chiral topological charge always vanishes.

The winding number defined in Eq. 4.5 can also be used to calculate the chiral topological invariant for multichannel wires [121]. The quasi-one-dimensional Hamiltonian used in this procedure is one in which a Fourier transform has been performed along the longitudinal x-direction, but not along the y-direction. Using $l, l' \in [0, W]$ to indicate the y-coordinate, we write $H_{TS} = \sum_{kll'} \Psi^{\dagger}_{kl}(H(k)\delta_{l,l'} + H^{\perp}_{l,l'})\Psi_{kl'}$ where $H^{\perp}_{l,l'} = -t\sigma_0\tau_z(\delta_{l,l'+1} + \delta_{l,l'-1})$. We use the procedure outlined above, where $A(k)$ is now a $2W \times 2W$ dimensional matrix and multiple Bloch bands can now be mapped to $U(1)$ by the determinant function. The result is sketched in Fig. 4.2 panel (b). As the chemical potential increases and higher bands are filled the gap closing occurs in the spectrum of H_{TS} and the corresponding topological invariant $\mathcal{W}$ increases by unity. We emphasize that when the chemical potential is in the lowest spin-split band (Fig. 4.2), the topological phase is generically present in this half-metallic FM situation since the spin-splitting is much larger than the

induced superconducting gap. We shall now discuss the experimental signatures which are a consequence of our model.

4.4 Scanning Tunneling Differential Conductance

Consider an STM brought close to the surface of the multichannel FM wire described by Eq. 4.1 (see Fig. 4.1) . The STM tip weakly couples to FM wire orbitals through a small hopping integral $H_{STM} = \sum_\sigma t'(c^\dagger_{s\sigma} d_{s\sigma} + \text{H.c.})$. Here d annihilates electrons at the STM tip which we take to be three sites wide and centered the x-coordinate $s = (x-1, x, x+1)$. We will parametrize the tunneling barrier at the STM tip (which determines the size of the zero bias tunneling peak at finite temperatures [114, 19]) by the single parameter t' for simplicity– typically $t' \ll t$ in the STM set up of Ref. 98. A potential difference V is now applied between STM and drain (i.e. the grounded superconductor on which the FM has been deposited). We will now set up a scattering matrix formalism to calculate the differential conductance through the FM wire, in order to experimentally detect the MBSs. Within this approach we model the STM, which is the first scattering lead, as a normal metal electron reservoir biased at a variable electrochemical potential $\mu_N + eV$ measured relative to the superconducting Fermi energy. Our quasi-one-dimensional FM wire (Eq. 4.1) acts as the scattering region and the second lead is the grounded electron drain which is held at chemical potential μ_N. We adopt a BTK perspective [122] in assuming that equilibrium Fermi distribution functions determine the incoming quasiparticle occupancy levels. Here, $\psi_{in} = (\psi^S_{in}, \psi^D_{in})^T$ are plane waves originating deep within the semi-infinite lead STM and drain leads which are described by the Fermi functions $f(E-eV)$ and $f(E)$ respectively. Note, in general $\psi^{S,(D)}$ is an $N(M)$ component spinor given $N(M)$ occupied channels in the STM (drain) lead. For a quantum coherent process we can relate the outgoing modes to the incoming modes by the scattering matrix $\psi_{out} = \hat{S}\psi_{in}$ where

$$\hat{S} = \begin{pmatrix} r & t' \\ t & r' \end{pmatrix}. \tag{4.6}$$

Here r is a $4N \times 4N$ matrix consisting of complex reflection coefficients between all the occupied incoming STM channels. Likewise r' is the reflection matrix for the drain and t, t' are the transmission coefficient matrices connecting the two leads. (Note that we use the same notations t, t' to denote the transmission matrix elements for the leads as what were used to define the tunneling amplitudes in defining the basic Hamiltonian, but there is no scope for any confusion here since the transmission matrix elements t, t' only

appear in Eq. 4.6 above in defining the $\hat{S}$-matrix and in our numerical work and nowhere else in the text below.)

In the presence of a proximity induced superconducting gap, single electrons cannot tunnel from the STM to the FM for low bias-voltages $V \ll \Delta$. As a result, all of the flowing current in the subgap regime is generated through the Andreev reflection process in which excess Cooper pairs are created and simultaneously the incident electrons are converted into holes. The reflection matrix can be written as

$$r = \begin{pmatrix} r_{ee} & r_{eh} \\ r_{he} & r_{hh} \end{pmatrix}. \tag{4.7}$$

where r_{ee} (r_{eh}) refers to the normal (Andreev) reflection submatrix. At low bias voltages the differential conductance, proportional to the transmission probability at a given energy E, is expressed in terms of the STM reflection matrices as [123]

$$\frac{dI(V)}{dV} = \frac{e^2}{h}\left[N - Tr(r_{ee}^{\dagger} r_{ee}) + Tr(r_{eh}^{\dagger} r_{eh})\right]_{E=V}. \tag{4.8}$$

We generate the scattering coefficients numerically using the Kwant [124] numerical package.

4.4.1 Results

We know from the topological properties discussion in Sec. 4.3 that MBSs appear as soon as any FM bands, within a normal state picture, become occupied. Setting $V = 0$ and using Eq. 4.8 we see a peak in the zero-bias conductance,quantized in units of $2e^2/h$, abruptly appear at the critical value of the chemical potential when the first band becomes occupied ($\mu \approx -0.7t$) as shown in panel (a) of Fig. 4.3. As μ increases, higher sub-bands are filled while the Majorana occupancy increases, and each MBS contributes its own factor of $2e^2/h$ to the total zero-bias differential conductance. The zero-bias peak is a direct probe of the Majorana occupancy as the plot for $W = 6$ in Fig. 4.3 (a) clearly mirrors the the zero-energy excitation spectrum given in Fig. 4.2. In realistic experiments, because of disorder and electrical contact complications, it is difficult to increase the chemical potential uniformly across an entire sample in order to induce a topological phase transition. It is for this reason that we instead propose manipulating the system width, i.e. tightly packing parallel magnetic atomic chains, as an experimental test of the chiral topological state. Fig. 4.3 panel (a) illustrates the zero-bias signal behavior for various values of W. Samples with different widths are expected to have a similar chemical potential, but the strength of the zero-bias peak at that μ should increase (red

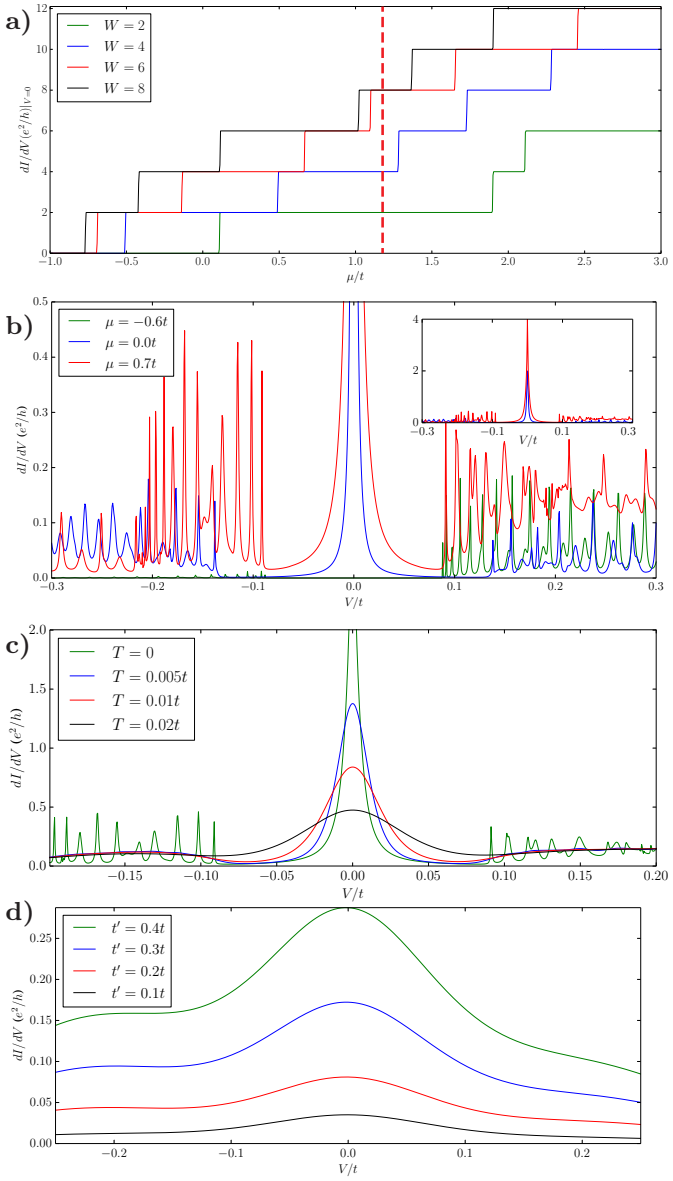

Figure 4.3: (Color online) (a) The zero-bias differential conductance as a function of chemical potential μ for various wire widths W. Since each Majorana modes contributes a factor of $2e^2/h$ to the zero-bias signal, this measurement directly probes the number of Majorana states present. For a given geometry the maximum possible conductance is $G_{max} = 4We^2/h$ (not shown here). (b) Representative dI/dV curves from parameter regimes with an integer topological invariant $|W| = (0, 1, 2)$ are given by the green, blue and red curves respectively. Inset shows the quantized peak height for the blue ($2e^2/h$) and red ($4e^2/h$) curves. (c) Finite temperature thermally broadens the zero-bias conductance peak width as well as reducing the height to well below the quantized value of $2e^2/h$. (d) Weak STM - FM nanowire coupling, i.e. small t', in conjunction with finite temperature ($T = 0.05t$) further reduces the peak height.

dashed line for example) as a function of W. It is also important to note that while finite temperature effects generally suppress the ZBCP height (as seen below), this effect is uniform and transitioning from $W = 2$ to $W = 4$ at μ corresponding to the dashed line, would still double the zero-bias signal. The observation of such jumps in the ZBCP height with increasing the number of wires or channels will be a strong indication that the ZBCP is indeed arising from the localized MBSs in the ferromagnetic wires in the BDI class.

Typical differential conductance profiles over finite voltage range are presented in Fig. 4.3 panel (b). The green, red and blue lines are dI/dV profiles generated for μ values corresponding to topologically distinct phases indexed by an integer winding invariant $|W| = (0, 1, 2)$. A superconducting gap devoid of subgap states ($V \leq .1t$) is characteristic of the trivial regime (green curve) while a quantized zero-bias signal appears in the non-trivial regimes.

The conductance at finite temperature T is given by

$$\frac{dI(V,T)}{dV} = \int_{-\infty}^{\infty} dV' \frac{dI(V', T = 0)}{dV'} \frac{d}{dV} f(V, T), \tag{4.9}$$

where $f(E, V, T) = (\exp[(E - \mu - eV)/T] + 1)^{-1}$ is the fermi function. In this paper all zero temperature results will be assumed to be smeared by an infinitesimal temperature $T = 10^{-5}t$. The finite temperature is crucial to avoid anomalies that depend on exponentially small coupling between Majorana modes which must exist in any finite length system no matter how long the wire is. As seen from previous calculations [125] the zero-bias conductance vanishes at strictly zero temperature even for a topological system. However, this anomaly reduces to the usual result of a quantized conductance at temperature T larger than the exponentially small Majorana splitting energy, but smaller than the tunneling energy between the Majorana mode and the lead. Strictly speaking, the tunnel coupling t' between the STM tip and the Fe nanowire is unknown in the experiment of Ref. 98 except that it is known to be very small. On the other hand, the experimental temperature in Ref. 98 is pretty high, $> 1K$, so the condition $t' > T$ is probably only marginally satisfied in Ref. 98. Fortunately, this does not cause any qualitative problem in the theoretical analyses where most of the experimental parameters, except for the temperature, are not precisely known any way. Thermally smeared differential conductance curves are plotted in Fig. 4.3 panel (c) for various temperatures. Similar to the zero-bias phenomena observed in recent semiconductor experiments, where the peaks are generally an order of magnitude smaller than $2e^2/h$[58, 60, 61, 62, 63], thermal effects smear our zero-bias peaks to well below its quantized value as was already pointed out in Ref. 19. Furthermore, the very weak coupling between the STM and the ferromagnetic nanowire, i.e. $t' \ll t$, in conjunction with finite temperature further

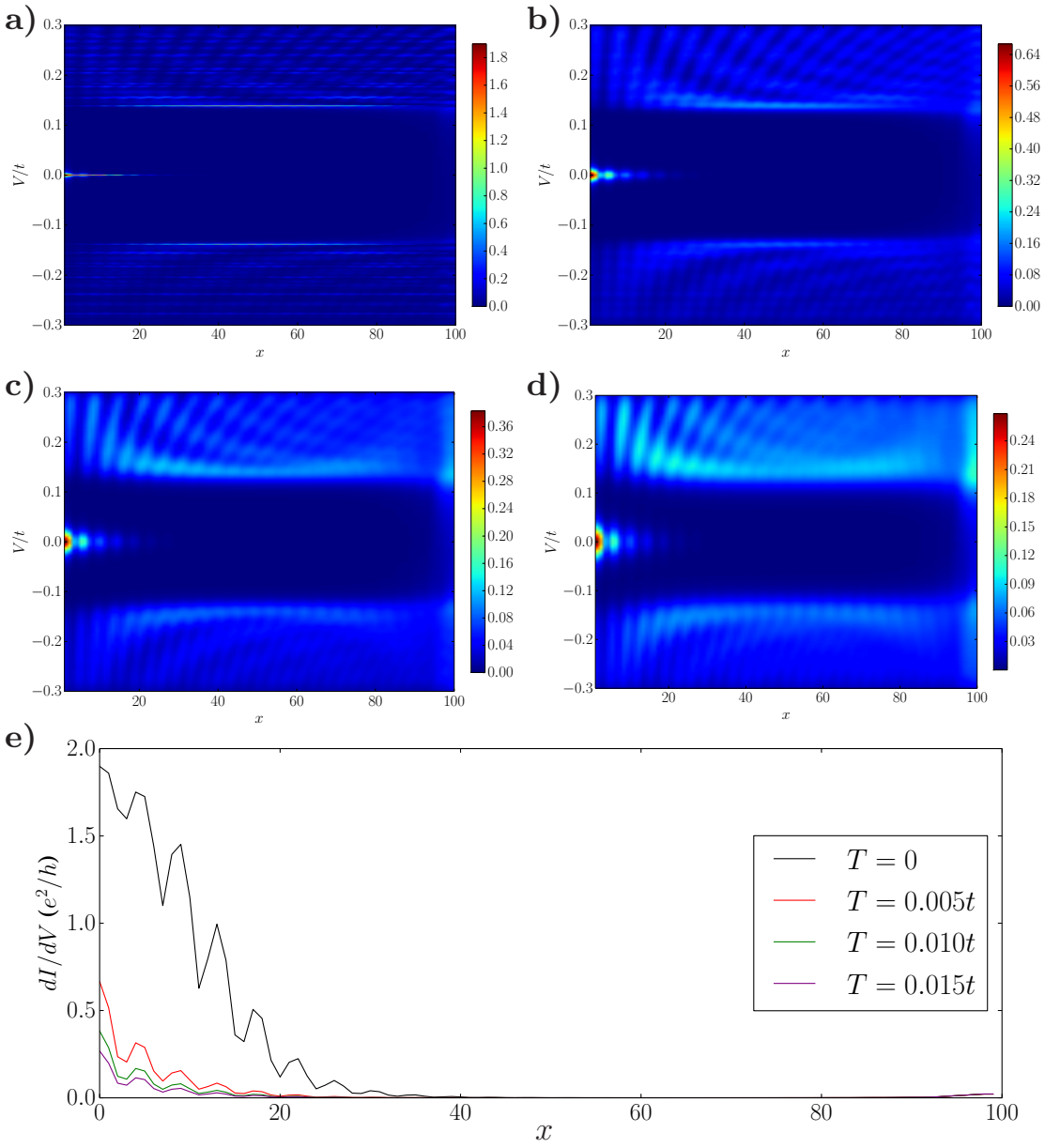

Figure 4.4: (Color online) Spatially resolved differential conductance profiles from the left edge to the middle of a wire with $L = 200$. Panels a)-d) are broadened by temperatures $T = (0, 0.005, 0.010, 0.015)t$. Note the color scales are different in each panel and we present the the zero-bias signal in panel e) for clarity. See discussion below Eq. 4.9 for a note on the $T = 0$ result.

reduces the ZBCP height. Choosing a temperature of $T = 0.02t$ we illustrate this phenomena in Fig. 4.3.

By varying the STM coordinate x, we now simulate the tunneling spectra which would result from spatially sweeping the STM probe across the length of the sample, which has recently been experimentally

achieved[98]. MBSs are localized at each end of the wire, and we expect the ZBCP to vanish as the STM reaches the wire midpoint. Fig. 4.4 a (b,c,d) shows the zero (finite) temperature differential conductance spatial profile. The signal due to tunneling into quasiparticle states above the superconducting gap remains approximately constant as the probe position varies, in contrast to the zero-bias signal which disappears in the bulk. A zero-bias spatial profile displayed in Fig. 4.4 (e) illustrates the exponential decay of the zero modes away from the edges as well as the end localization scaling with the characteristic length ξ (see discussion in next section, Fig. 4.5). The features shown in Figs. 4.3 and 4.4 are generally consistent with the experimental findings in Ref. 98, providing some level of confidence that the experimentally observed ZBCP may indeed be arising from MBS-related physics (although the model parameters used in these figures are not realistic representations of the Fe/Pb system used in Ref. 98).

4.5 Experimental Implications

Having established generic features of our model, we now turn our attention to a comprehensive comparison with a recent experiment[98] which shares many, *but unfortunately not all*, features with our theoretical results. Our focus here is mainly on comparing the qualitative phenomenological properties of the experimentally observed ZBCP and our theoretical results. In addition to analyzing the height and width of the ZBCP as a function of temperature, wire length, and the STM tunnel barrier, we will also closely examine the spatial structure of the differential conductance profile, which can be directly calculated from our STM simulation (see Fig. 4.4). To begin with, we first recapitulate the system parameters as quoted in Ref. 98 and then set up our numerical parameters accordingly for comparison. The ferromagnetic splitting is estimated to be $J = 2.4\ eV$, which is much greater than the estimated hopping parameter $t = 1\ eV$ (which in turn is much larger than the superconducting gap $\sim 1\ meV$ in the substrate, thus allowing us to use the half-metallic ferromagnetic nanowire model for the theoretical description). Additionally, the superconducting gap in the underlying substrate is $\Delta_s = 1.36\ meV$ while the induced p-wave gap is estimated to be $\Delta_p = 100\ \mu eV$ [98]. Measurements were made on atomic chains between $100 - 150\ nm$ in length at a temperature $T = 1.4K$ which corresponds to 100 μeV in energy (roughly equal to the topological gap). This experimentally used parameter regime is obviously a non-ideal regime for studying topological superconductivity since the lowest energy scale is the topological gap in the system, which is the same as the temperature of the system. Temperature would therefore be expected to suppress any signatures of the topological gap, including the Majorana zero-mode, which would merge with the bulk states. As already discussed in earlier sections of

this paper, this estimated parameter regime for Ref. 98, particularly the hopping along the chain ($t \sim eV$) being much larger than the superconducting gap ($\sim 1meV$), implies the applicability (non-applicability) of the nanowire (Shiba) model to the experimental situation.

To compare our results with the experiment we introduce two parameter regimes, each characterized by different Majorana decay length scales, and then compare the results between the two regimes. In the *large pairing* regime we take the magnitude of the superconducting pair potential to be $\Delta_p = 0.1t$ while in the *small pairing* regime we use $\Delta_p = 0.01t$. (To be clear, the system is always in a topological state and this is not to be confused with the weak/strong pairing regimes of Ref 31 which describe topologically non-trivial and trivial phases.) In both cases we choose $\Delta_s = \Delta_p$ and simplify our notation by referring to this quantity simply as Δ (keeping in mind that Δ_p is responsible for the topological properties). In both parameter sets we use $\mu = -.65t$, $W = 2$ and $V_y = 2t$. We also typically choose very small values of $t'(\ll t)$ to simulate the very large tunnel barriers occurring at the STM tip contact with the nanowire. (Very small values of t' are essential for obtaining extremely weak zero-bias signals for the Majorana modes as observed experimentally.)

In a finite system, the localized MBS wavefunctions exponentially decay into the bulk with the characteristic superconducting coherence length $\xi \propto v_F/\Delta$, thus acquiring a finite energy due to wavefunction overlap from the two end MBS on two sides (true zero modes only occur in the $L \to \infty$ limit). Fig. 4.5 panels (a,b) show the Majorana amplitude $|\Psi|^2$ on systems composed of $L = 700, 100$ sites in the large pairing regime. The Majorana decay length is clearly much shorter than the wire length for both cases, so zero-energy Majorana bound states are localized at each end of the wire and with $|\Psi|^2$ being negligible near the midpoint. Panels (c,d) illustrate the wavefunction amplitude in the small pairing regime, in which the Majorana decay length is comparable to the system size for the $L = 100$ case. The end modes appear unaffected in the $L = 700$ wire, however, the wavefunctions for Majorana modes bound to opposite ends of the wire overlap significantly in the $L = 100$ case, and as we discuss later, this has important ramifications for the zero-bias signal. Note that the small gap used in the small pairing regime ($\Delta = 0.01t$) is closer to the experimentally quoted parameters which would indicate a minuscule value of $\Delta = 10^{-4}t$ (since the experimental system has $t \sim 1eV$ and $\Delta \sim 100\mu eV$). We do not use even smaller Δ due to the prohibitive computational resources which would be required; however, the physics is generic and the topological pair potentials we have chosen are already sufficiently small, albeit still two orders of magnitude larger than the experimental values, to illustrate our point. In fact, our theory is strongly over-emphasizing the topological aspects of the experimental systems– all topological signatures will be much weaker in the experiment compared with our results since the induced gap is much smaller in Ref. 98 than our chosen theoretical value.

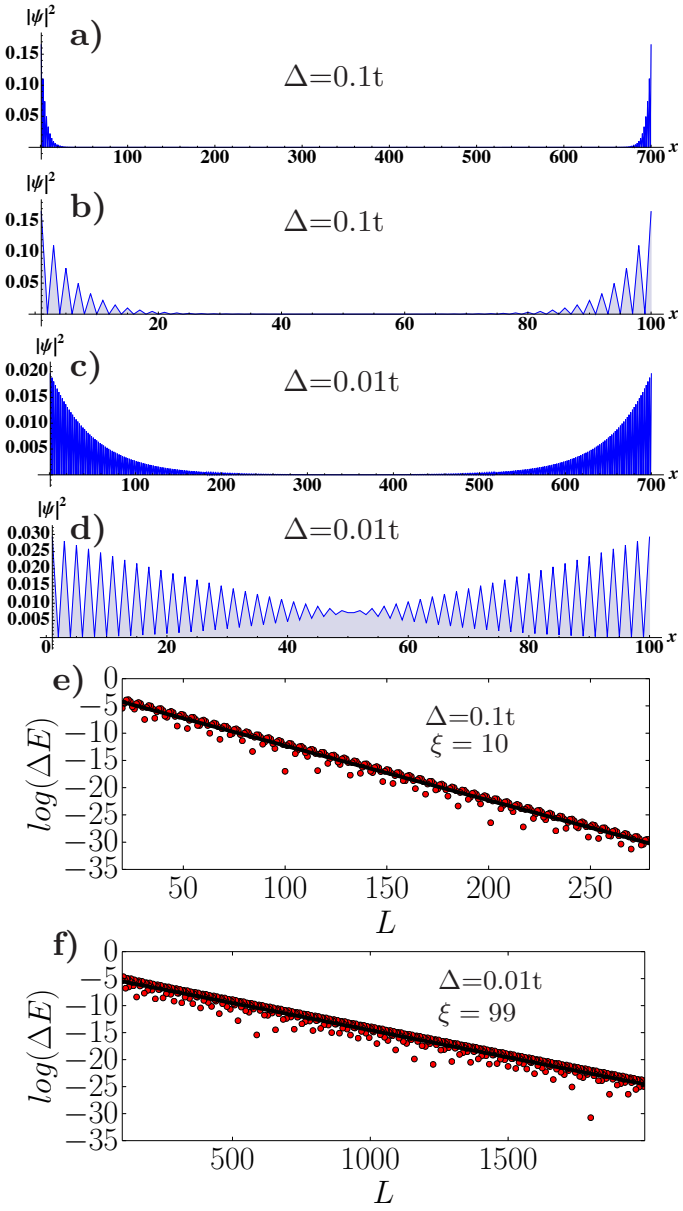

Figure 4.5: (Color online) Majorana wavefunctions for small ($\Delta = 0.01t$), and large ($\Delta = 0.1t$), pairing regimes as calculated for short ($L = 100$) and long ($L = 700$) systems. For both lengths considered in the large pairing regime, panels a,b), the Majorana decay length is much smaller than the system length ($\xi \ll L$), so the zero energy excitations are heavily localized to the FM wire endpoints. Panels c,d) illustrate how reducing the pair potential to $\Delta = 0.01t$ substantially increases the Majorana decay length and while a 700 site system still hosts Majorana states, considerable wavefunction overlap in the 100 site system hybridizes the end modes into conventional, delocalized quasiparticle states. Panels e,f) show the logarithm of the energy splitting ΔE between the two Majorana modes. As the wire length L increases ΔE falls off exponentially. Majorana decay lengths of of $\xi \sim 10$ sites, in the large pairing regime, and $\xi \sim 99$ sites, for the small pairing regime, are extracted from the black linear fits in panels e,f) respectively.

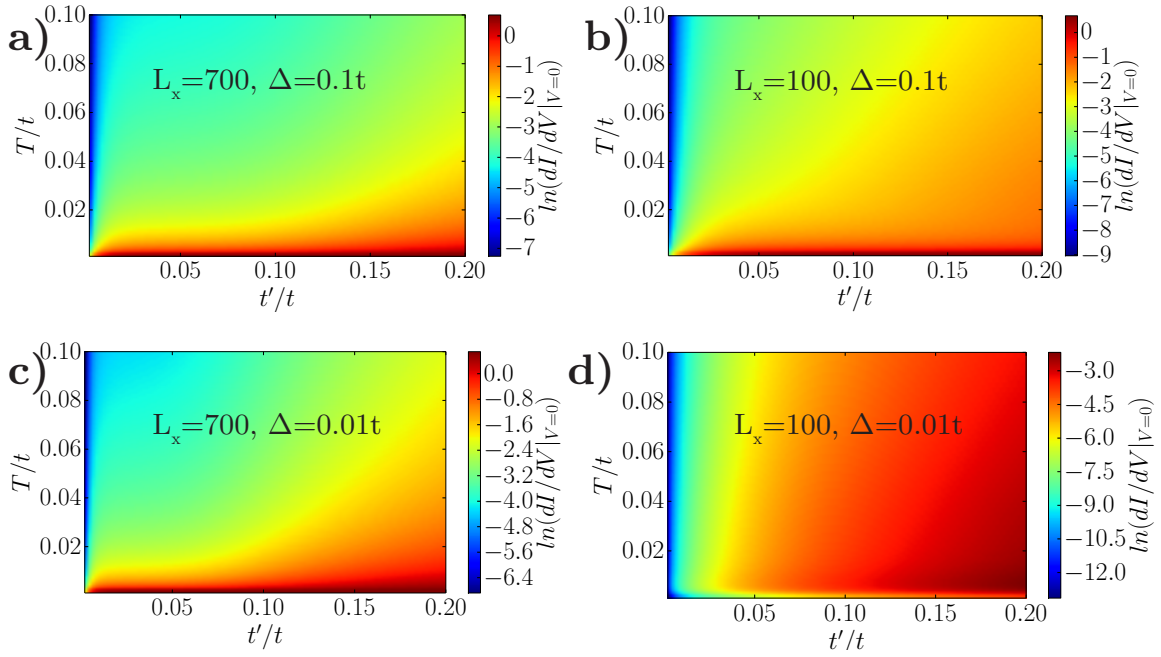

Figure 4.6: (Color online) Zero-bias differential conductance peak height, panels correspond to same parameter values as used in Fig. 4.5 panels a-d), at one end of the wire ($x = 0$) as a function of STM-FM coupling t' and temperature T. Panels a-c) When the Majorana decay length is significantly shorter than L a quantized zero-bias signal of $2e^2/h$ is seen at zero temperature and $t' > 0.03t$ (dark red on logarithmic color scale). The quantized signal decays rapidly by introducing finite temperature or decreasing t'. Panel d) No zero-bias signal is present near zero temperature (see below Eq. 9 for details) due to Majorana hybridization which splits the zero-bias peak into two separate finite bias signals. The cause of this effect is finite temperature, which smears two finite-bias peaks together for an effective zero bias signal (see to Fig. 4.9 for details).

ΔE, the MBS splitting, can be directly captured using an effective Hamiltonian spanning the zero-energy Majorana subspace, $H_{eff} = i(f/2)\gamma_L\gamma_R$ where $f \propto exp(-L/\xi)$. In Fig. 4.5 panels (e,f) we numerically calculate ΔE as a function of length in order to determine the decay length. Plotted on a logarithmic scale, the red circles represent the raw data while the black linear regression has been fit to the data. Taking $f = exp(-L/\xi)$ we extract coherence (or equivalently, MBS localization) lengths of $\xi = 10, 100$ sites in the large and small pairing regimes respectively. Note that the 'beading' on top of the exponential decay is due to constructive and destructive interference between the MBSs, and the length scale of these oscillations go as $1/k_F$ [126]. Note that our estimated Majorana localization length is likely to be an underestimate, i.e. the real localization length is likely to be larger, since the actual MBS localization, depending on some technical details, may have an algebraic fall off in some situations, and because the actual reported topological gap in Ref. 98 is two orders of magnitude smaller than our choice.

Next, we consider the roles of STM-FM coupling t' and finite temperature T in the quantitative

suppression of the ZBCP strength in both parameter regimes. As we have already noted in Fig.4.3 a small t' reduces the ZBCP, which in conjunction with thermal smearing effects, significantly reduces the zero-bias signal. As seen in Fig. 4.6 panels (a,b), the $T = 0$ zero-bias signal in the large pair potential regime, where both wire lengths support MBSs, saturates to the quantized value of $2e^2/h$ as t' becomes large. Increasing temperature or decreasing t' both monotonically reduces the magnitude of the zero-bias signal, and similar behavior is found in panel (d) (long wire in small pairing regime), which also hosts well defined Majorana excitations. Interestingly, as seen in panel (b), the short wire in the small pairing regime, i.e. one in which MBSs have hybridized due to the small wire length ($\xi \sim L$), displays a finite temperature zero-bias signal comparable in magnitude to the finite temperature signal seen in the other panels. Moving upward from the zero-temperature x-axis towards large temperature, this signal grows until some critical value, after which the zero-bias signal decays like in the other panels. As discussed later in this section, the source of this unusual zero-bias peak behavior increasing with temperature is thermal smearing between a pair of split Majorana states near zero energy.

Having established that a strongly suppressed ZBCP is a generic feature of the experimental parameter regime (i.e. small t', large T, and small topological gap), observable with or without the existence of zero energy Majorana excitations, we now analyze the spatial profile of the ZBCP, which can in principle be used to distinguish between a signal originating from zero energy or finite-energy split quasi-MBSs. Focusing on the small pairing parameter regime first, i.e., the parameters which are closer to those reported in Ref. 98, we plot the differential conductance measured at three STM positions $x = 0, L/4, L/2$ along a wire of length 700 sites (see Fig. 4.7). In panel (a) the conductance is measured from the wire endpoint (i.e. $x = 0$) and we observe that finite bias quasiparticle states are separated from the Majorana signal by a gap which is comparable in magnitude to the pair potential (recall, $\Delta = 0.01t$). Note the zero-bias Majorana signal (green and red solid lines are almost completely superimposed and therefore not discernible) is delta function shaped as a consequence of the small coupling parameter t'. The dashed lines indicate the signal at a finite temperature of $T = \Delta = 0.01t$, which is the case in Ref. 98. The thermally broadened peak height for the green dashed line is $10^{-3}e^2/h \approx 40nS$ which is comparable to that reported in the experiment. Additionally, the peak width at half maxima is Δ, which is also consistent with experimental results. Panel (b) shows how by moving the STM tip into the bulk of the wire ($x = L/4$) the zero-bias signal drastically falls off, to the point where it is of the same order of magnitude as the conventional background thermal quasiparticle signal. Due to the large separation between the zero- and finite-bias signals, a valley, centered around $V = 0$, appears in the thermally broadened conductance profile (dashed line). Lastly, in panel (c) we see that, as expected, the Majorana peak

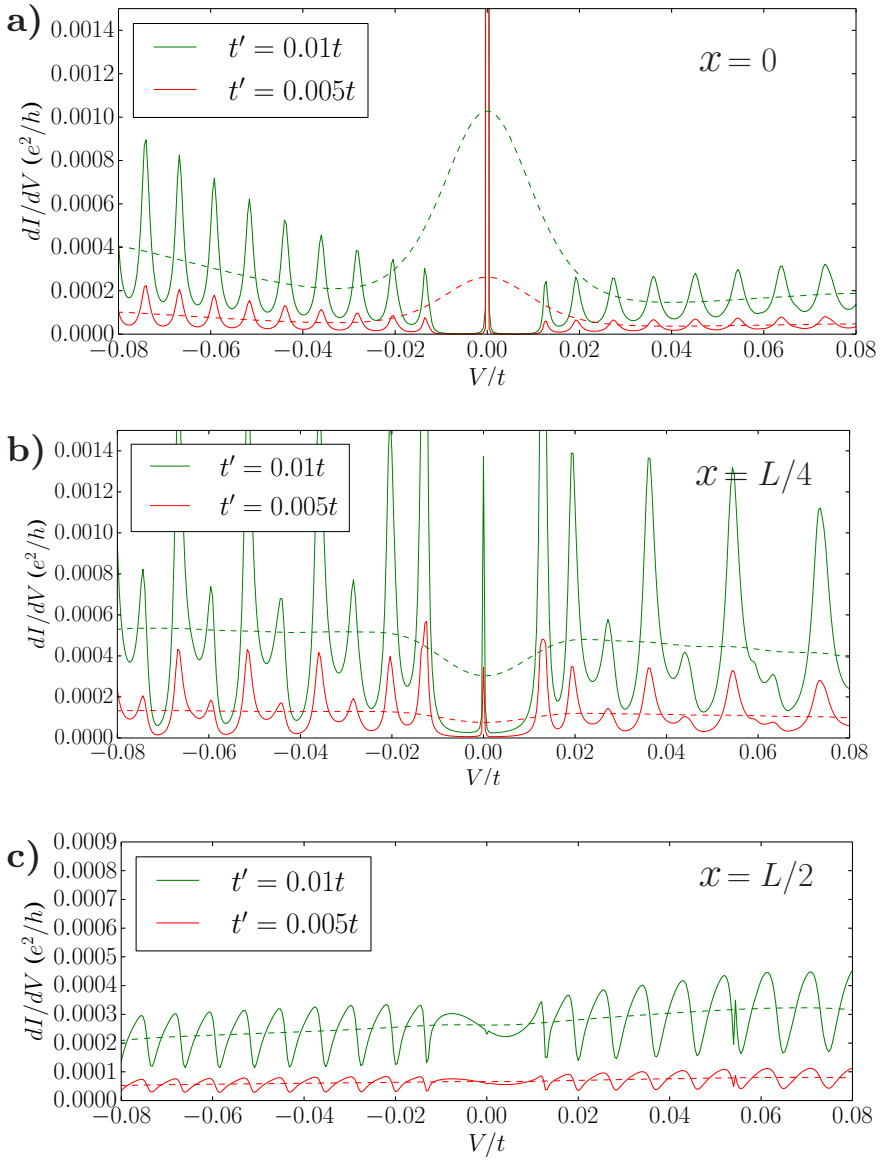

Figure 4.7: (Color online) Differential conductance calculated using an STM coordinate $x = 0, L/4, , L/2$ for a long wire $L = 700$ in the small pairing regime. Solid and dashed lines are at temperature $T = 0, 0.01t$ respectively, and green (red) lines correspond to a STM-FM coupling of $t' = 0.01t$ $(0.005t)$. Panel a) shows a clear zero-bias signature which is visible at the wire endpoints for both zero and finite temperature. The green dashed line ($T = \Delta$) displays a peak height ($10^-3e^2/h \sim 40nS$) and width ($\sim \Delta$) which are comparable to the experimentally reported values. Panels b,c) The zero temperature Majorana peak decays as the STM moves into the FM nanowire bulk. The peak completely vanishes at the midpoint, and is not visible at zero or finite temperature signal.

is completely absent at the wire midpoint $x = L/2$. All these features appear to be qualitatively consistent with the experimental data reported in Ref. 98.

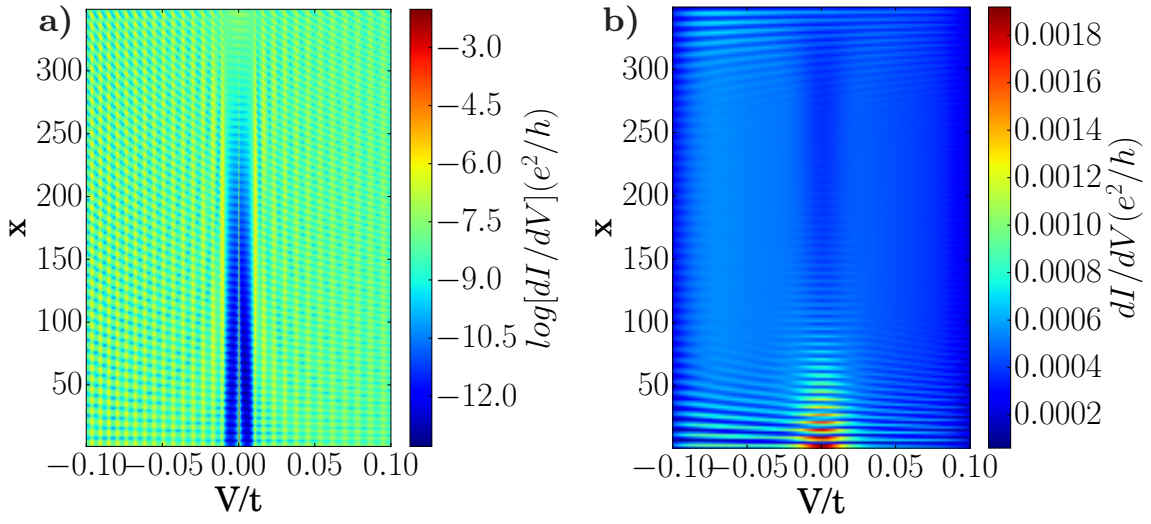

Figure 4.8: (Color online) Differential conductance spatial profile as a function of the STM coordinate x. Panels a) b) correspond to temperature $T = 0, 0.01t$ respectively, and we present the zero temperature data on a logarithmic scale for improved visibility. At zero temperature, the spatially localized Majorana mode resides within a well defined superconducting gap which not visible at finite temperature due to thermal smearing effects. Note that the true spatial extent of the Majorana mode is revealed by the finite temperature result, i.e. on a linear scale.

A detailed spatial profile of the differential conductance should reveal the highly localized Majorana wavefunction from Fig. 4.5. In order to numerically reveal the localized nature of these Majorana wavefunctions, we smoothly vary the STM tip position x and plot the zero temperature differential conductance at each point in Fig. 4.8 panel (a). Along most of the wire, the spatially resolved dI/dV indicates a well formed superconducting gap separating the single Majorana peak at zero energy from the finite energy quasiparticles. Note that, in this plot, the spatial extension of the Majorana wavefunction is exaggerated due to the logarithmic scale which has been used to increase the visibility of the data. Panel (b) shows the spatially resolved conductance at finite temperature ($T = \Delta$), which reveals the true spatial extent of the Majorana mode. We pause to note that while the model parameters used here are similar those quoted in the experiment, the localization length seen in panel (b) is significantly larger than reported in Ref. 98. This much longer MBS localization length in the theory is the most important unresolved discrepancy between theory and experiment. The MBS localization length could be substantially reduced by increasing the induced gap energy Δ, but to obtain an MBS localization length as short as the ones reported in Ref. 98 one would have to use completely ludicrous values of the proximity-induced pairing gap around $1000K$ implying a bulk superconducting gap of $10,000K$ (or higher) for Pb. We see absolutely no way out of this incompatibility between theory and ex-

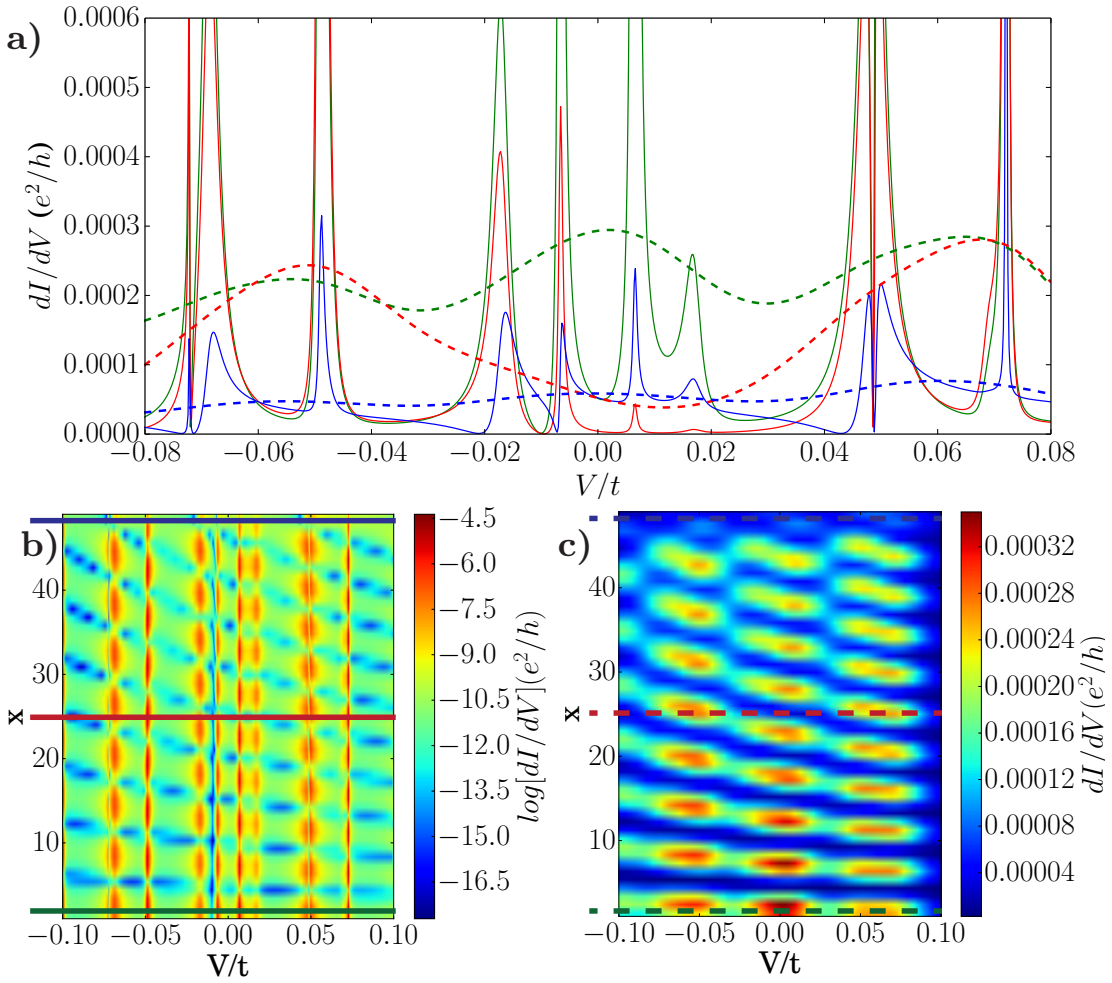

Figure 4.9: (Color online) When the ferromagnetic nanowire is short (i.e. $L \sim \xi$) Majorana bounds states at opposite ends hybridize as their wavefunctions overlap significantly in the bulk. Panel a) Using the same parameters from the Fig. 4.8 except $L = 100$, we see that the zero-bias Majorana signature splits into two distinct peaks centered near $V = \pm 0.01t$. The green, red, and blue curves correspond to the differential conductance calculated at $x = 0, L/4, L/2$ respectively, and the solid (dashed) lines denote the zero (finite $T = \Delta = 0.01t$) temperature. Panels b,c) Spatially resolved differential conductance along the longitudinal axis for zero (on a log scale) and finite temperature. Solid and dashed lines indicate the position of the dI/dV curves presented in panel a).

periment at this stage. To put it simply, one cannot have a tiny topological gap as well as a strongly localized end Majorana mode as seems to have been observed in Ref. 98 – these two are fundamentally incompatible.

Since small pair potentials and short wire lengths are quoted in Ref. 98, we now investigate the small pair potential regime ($\Delta = 0.01t, \xi = 99$) on the $L = 100$ system, i.e. parameters which should be most applicable to the experiment. Remember that for these parameters the Majorana modes generally hybridize

(see Fig. 4.5) and therefore the Majorana splitting should be visible. Using an STM-FM coupling strength $t' = 0.01t$, the green, red and blue solid lines in Fig. 4.9 panel (a) show the differential conductance calculated at STM positions $x = 0, L/4, L/2$. We immediately note that, due to finite size effects, the zero-bias signal has split into two peaks centered around $V = 0$, with an estimated energy splitting comparable to the gap energy ($\Delta E = 0.01t$). Also note, that while the tunneling signal into these two finite energy quasiparticle states may be the largest at $x = 0$, the signal persists well into the bulk of the wire ($x = L/4, L/2$). At finite temperature $T = \Delta$, the splitting between the peaks is no longer visually resolvable since temperature has thermally broadened the signal across a range greater than the original Majorana splitting ΔE (dashed green line). Panels (b,c) illustrate the differential conductance spatial profile for temperatures $T = 0, 0.01t$, where again we have presented the zero temperature data on a logarithmic plot. In these bottom panels we see that the split quasi-Majorana modes are spatially extended across the entire length of the wire. Green, red and dark blue solid and dashed lines superimposed on the spatial profiles correspond to the dI/dV curves presented in panel (a). Thus, in the context of a small pairing potential present in a short wire, we see a finite temperate zero-bias signal extending into the bulk of the wire, with no measurable decay. For reasons which remain unclear at this stage, this theoretically expected splitting of the Majorana mode and the associated spatial delocalization of quasi-Majorana modes are again not observed in the experiment, casting serious doubts on the whole theoretical interpretation.

In light of the above results, it seems intrinsically inconsistent that Ref. 98 reports a proximity induced p-wave pair potential orders of magnitude smaller than ours (i.e. $10^{-4}t$ in the experiment rather than $10^{-2}t$ as in our numerics– this should make the incompatibility and the inconsistency discussed here far worse quantitatively), while at the same time claiming to observe a very short Majorana decay length. For the Majorana decay length to match the experimental value ($\xi \sim 5nm$) an extremely strong proximity effect would be needed to induce much larger p-wave superconducting gap than reported in the experiment. Therefore, we have every reason to believe that either the zero bias peak is not topological in origin or some other physics, not captured by our model, drastically and unexpectedly reduces the Majorana decay length for reasons completely unknown at this stage. Our conclusion is that while we can explain either the observed ZBCP and its spatial dependence very well in both long and short wires or we can explain the observed strong MBS localization and the lack of MBS splitting (simply by assuming large ad hoc numbers for the topological gap, thus suppressing the Majorana localization length), but there is no consistent model to explain both behaviors together since they are fundamentally incompatible with each other– a small gap automatically implies a long MBS localization length. In the experimental reference[98], this serious incompatibility is

not mentioned at all, with the authors 'explaining' the strong MBS localization by a completely different (and highly simplistic) Shiba chain model (whereas everything else in the experiment is described using a ferromagnetic wire model) which as already emphasized in the Introduction of our paper, does not apply at all to the experimental system of Ref. 98 since the inter-atomic hopping parameter t is much larger than the bulk superconducting gap. The use of a fine-tuned Shiba chain model to explain the strong MBS localization and the ferromagnetic wire model to describe the ZBCP physics of course makes no sense at all, since the two models apply in very different regimes of parameters, and obviously the experimental system belongs to the nanowire model and not the Shiba model. The other option of obtaining compatibility between the ZBCP observations and the strong MBS localization would be to assume absurd superconducting gaps of many thousands of K. A consistent (even qualitative) understanding of all aspects of the experimental data presented in Ref. 98 remains a completely open question at this stage.

An additional problem in the interpretation of the experimental data of Ref. 98 is the issue of disorder which should very strongly suppress the induced p-wave superconductivity. Given that the induced gap is $0.1\ meV$ and the typical electronic energy scales in the ferromagnetic chain (i.e. hopping energy, chemical potential, exchange energy) are all in the eV range, one expects the slightest static fluctuations in the system (e.g. $0.1\ \%$ variation in the locations of the Fe atoms or the presence of any neighboring random impurities near the chain) to completely destroy the topological superconductivity in the system since the p-wave pairing is not protected against disorder by Anderson's theorem [127]. One simple and approximate way to estimate disorder effects here is to ask about the amount of elastic scattering which would be necessary to completely suppress the reported $100\ \mu eV$ topological gap in Ref. 98. Equating the reported p-wave gap to a disorder induced collisional level broadening of $100\ \mu eV$ in the Fe chain and using the band parameters estimated in Ref. 98 for the system, it is easy to conclude that the electronic mean free path along the Fe chain must be longer than $100nm$ for the disordered system to manifest any topological gap (assuming the clean system gap to be $100\ \mu eV$). This is of course inconsistent with the observation of a topological gap in chains of variable lengths between 5 nm and 15 nm as reported [98] since the wire length serves as a cut off for the maximum possible mean free path in the system. One could of course assume that the measured gap already incorporates the disorder effect (starting from a much larger clean topological gap), but this would imply very strong dependence of the measured topological gap on the wire length, not reported in Ref. 98.

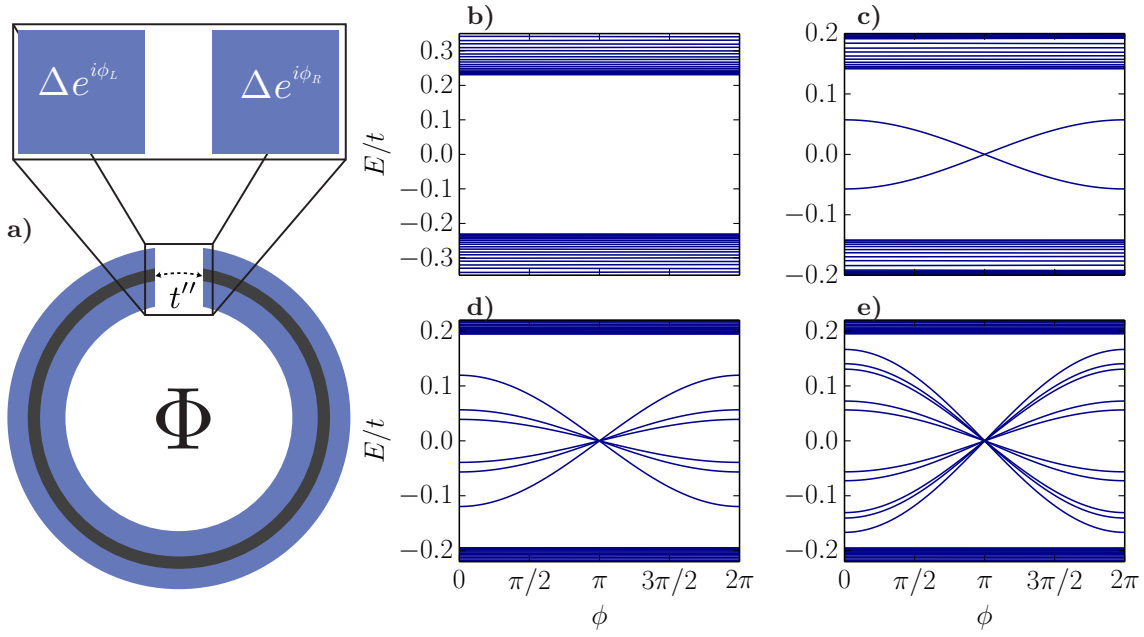

Figure 4.10: a) Top view of ring geometry JJ formed by weakly coupling ($t'' = t/10$) the two ends of a nanowire. The phase difference across the junction is controlled by the magnetic flux, Φ, threading the ring. b) Evolution of subgap Andreev bound states as a function of the phase difference between two superconductors in a Josephson junction setup. Zero energy crossings are absent in the ABS spectrum in the topologically trivial regime. c) In the $|\mathcal{W}| = 1$ phase, the ABS spectrum crosses zero energy for the single value $\phi = \pi$. Transitions between the subgap branches are forbidden by particle-hole symmetry so that Fermion parity flips as ϕ evolves by 2π. d,e) Spectra in a system indexed by topological invariant $|\mathcal{W}| = 3, 5$. There are $|\mathcal{W}|$ protected zero energy crossings and chiral symmetry forbids transitions between different sets of subgap branches.

4.6 Chiral Fractional Josephson Effect

We now turn our attention to another important signature which would definitively confirm the presence of the topological superconducting state, the fractional Josephson effect. A Josephson junction (JJ) consists of two superconductors connected by a weak link, normal metal or insulator for example. Conventionally, the current passing through a JJ obeys the 2π periodic current-phase Josephson relation, $I_J = I_c \sin(\Delta\phi)$, where $\Delta\phi = \phi_L - \phi_R$ is the phase difference across the junction and I_c is the critical supercurrent. It has been predicted [80, 36] that spinless p-wave superconductors, when in a topologically non-trivial phase, obey a 4π periodic current-phase relation $I_J \propto \sin(\phi/2)$. Even if quasiparticle relaxation times are shorter than the phase adjustment time, one expects to see a peak in the current noise spectrum at half the Josephson frequency[128]. The difference in periodicity is rooted in the fact that only Cooper pairs can tunnel between conventional superconductors, while single electron tunneling is enabled by MBSs, thus

doubling the Josephson period from 2π to 4π in the process.

Weakly coupling the two ends of a finite wire by a hopping integral t'' allows us to model a Josephson junction (see Fig. 4.10). The Hamiltonian for our ring geometry is $H = H_{TS} + H_J$ where $H_J = \sum_\sigma t''(c^\dagger_{N\sigma}c_{1\sigma} + \text{H.c.})$. Hybridizing the two Majorana states by t'' results in the formation of Andreev bound states (ABS) in the weak link junction.

Next, we wish to control the superconducting phase difference across our junction by penetrating the ring with a magnetic flux Φ. Since we introduce a flux we must use the phase which is invariant under a gauge transformations $\boldsymbol{A} \mapsto \boldsymbol{A} + \nabla\chi$ (χ is an arbitrary scalar function). This is given by [129] $\phi = \Delta\phi - \frac{2\pi}{\Phi_0}\int \boldsymbol{A}\cdot d\boldsymbol{l}$ where the integration is performed across the junction. The magnetic vector potential couples to the momentum by $\boldsymbol{p} \mapsto \boldsymbol{p} - e\boldsymbol{A}/c$ and we model this on a lattice with the Peierls substitution $t \mapsto te^{ie\int \boldsymbol{A}.d\boldsymbol{l}/\hbar}$ where the integral is taken along the two sites which t connects. The Peierls phase factor is exactly half the gauge invariant phase and the matrix elements connecting the ring junction become $t''e^{\pm i\phi/2}$ (Fig. 4.10) where the $\pm$ corresponds to counter- or clockwise hopping across the junction.

At zero temperature the Josephson quasiparticle current is $I_J = \sum_n \partial E_n(\phi)/\partial\phi$, where n indicates the nth excited Bogoliubov state [80] and the summation is taken over all states up to the Fermi energy. Using this and the Josephson current-phase relation, it is clear that the relevant quasiparticle energies obey a cosine like behavior with the same periodicity as the current. Andreev bound states (ABS) are quasiparticles bound to the junction and are responsible for the Josephson current, in contrast with ϕ independent bulk states which do not contribute to the Josephson current. Therefore, one can deduce the periodicity of the Josephson current just by looking at the ϕ dependence of the ABS spectrum (Fig. 4.10). A topologically trivial junction is marked by an absence (generically any even number) of zero energy crossings as seen in panel (b). In this regime each quasiparticle's energy is 2π periodic, the fermion parity is conserved, and the Josephson relation is a conventional 2π periodic one. Upon entering the topologically non-trivial regime, a single protected crossing emerges at $\phi = \pi$ (an odd number of crossings will generally flip Fermion parity). Transitions between the positive and negative energy subgap branches are forbidden by particle-hole symmetry so that Fermion parity flips as ϕ evolves by 2π. During this process, a single electron is transferred across the junction which is forbidden in parity conserving topologically trivial superconductors. Winding ϕ by another factor of 2π recovers the spectrum and fermion parity, leading to a 4π Josephson effect. Further increasing the chemical potential causes more energetic sub-bands to become occupied and the system transitions into topological phases characterized by topological index $\mathcal{W} > 1$. The ABS spectrum in this regime contains $|\mathcal{W}|$ sets of protected zero energy crossings at $\phi = \pi$. In addition to PH symmetry, chiral symmetry now

forbids transitions between the different sets of ABS leading to a robust 4π Josephson effect. The basic idea here is that non-trivial JJ physics, indicating the existence of the fractional Josephson effect associated with the existence of the MBS in the system, can be tuned by varying W rather than μ. W should in principle be easier to tune in the current system, due to the experimental challenges associated with manipulating chemical potential via an electrostatic gate potentials.

4.7 Summary

In this work, motivated by a recent experiment[98] in which STM zero-bias peaks have been observed from the edges of chains of magnetic atoms deposited on superconducting Pb substrates, we show that a multichannel ferromagnetic wire deposited on a spin-orbit coupled superconducting substrate can realize a non-trivial topological superconducting state with one or more Majorana bound states localized at the wire ends. We explain how the persistence of the zero-bias phenomena for generic parameters [98] as observed in the experiments can be understood if the induced topological superconductivity is chiral in nature. To test this hypothesis, we develop several experimental signatures which may verify the existence of a topological superconducting state. When several chains of magnetic atoms (such as Fe), or a multichannel FM nanowire, are deposited onto a spin-orbit coupled superconductor such as Pb, a mixture of spin-singlet and triplet components are expected to be proximity induced [99, 100, 109, 110, 111, 113]. The induced topological superconductivity may generically belong to the topological class BDI, which is characterized by a $\mathbb{Z}$ topological invariant. In this case, by varying the wire width – or equivalently by coupling parallel chains of magnetic atoms – one can increase or decrease the strength of the zero-bias signal in a controlled manner. The width dependence of the peak height is robust against finite temperature effects, which reduce the peak height from the zero-temperature quantized value. Observing this width dependence of the ZBCP would establish the presence of a chiral topological superconducting state. We also show that the 4π fractional Josephson effect remains, even in the presence of multiple spatially overlapping MBSs, and can be used to reveal the Majorana occupation number by tuning the width parameter of the coupled chains.

This work has been motivated by recent experiments [98] studying the conductance spectrum of a ferromagnetic wire on a spin-orbit coupled superconductor. Our calculations reproduce the qualitative features of the position and voltage dependence (Fig. 4) of the conductance experiments. The low value of the measured conductance in experiment can be attributed to the small topological gap, the high tunnel barrier at the STM-wire contact, and the large temperature. In spite of this success in our reproducing the qualitative

behavior of the observed ZBCP in the experiment of Ref. 98, we conclude that the current experiment is internally inconsistent and cannot be even qualitatively explained by our theory since we have no explanations whatsoever for the experimentally observed strong localization of the Majorana bound states near the wire ends and for the lack of observation of the Majorana splitting in the experiment. Since the topological gap needed for explaining the observed zero bias peak is very small, the corresponding Majorana localization length must be very large in the system, leading to the Majorana wavefunction having considerable weight very far from the wire ends as well as considerable Majorana energy splitting due to the overlap between Majorana modes from the two ends. Since the latter two predictions of the theory are incompatible with the experimental observations, we conclude that the current data cannot be explained by the standard model of Majorana fermions in magnetic nanowires coupled to superconducting substrates. The extreme Majorana localization observed in the experiment necessitates superconducting gap energy which are thousands of kelvins, obviously a ridiculous proposition, and at this stage we have no consistent explanation for the observed $100\ \mu eV$ topological gap along with $< 5nm$ Majorana localization length in Ref. 98.

The most important conclusion of our work with respect to the recent experiment [98] is that we find a fundamental qualitative *inconsistency* between having a very small topological gap and very strongly localized Majorana zero mode in the reported data. We do not see how this basic inconsistency can be resolved since the Majorana localization length is inversely proportional to the gap. A related problem is the non-observation of either the Majorana mode or any Majorana splitting in short wires where theory predicts the existence of observable quasi-Majorana signal as well as the presence of observable Majorana splitting.

Chapter 5

Conclusions and Summary

In this thesis we have theoretically analyzed the signatures associated with, and the robustness of, condensed matter analogues of Majorana fermions in a variety of condensed matter platforms. A comprehensive review of our results is first presented in this. last chapter. Afterwards, we comment on a few open questions, which have arisen during the course of this work, as well as on possible future directions.

5.1 Summary of results

In chapter 2 we calculated Berry phase mediated thermoelectric coefficients for electron- and hole-doped semiconductor thin films with Rashba and Dresselhaus spin-orbit coupling. Under the appropriate parameter conditions, i.e. application of a finite in plane magnetic field, we find that a gap appears in the conduction (electron-doped) or valence (hole-doped) semiconductor bands. A necessary condition for the realization of a two dimensional $\mathbb{Z}_2$ topological superconducting phase is that the chemical potential lies within 'non-trivial' gap. For both carrier types, the intrinsic contribution to the anomalous Hall coefficient saturates to a fixed value when the chemical potential satisfies the non-trivial condition and vanishes otherwise. We found an even more striking signature provided by the anomalous Nernst coefficient which shows that the non-trivial regime is marked two sharp peaks of opposite sign, separated by a region with a vanishing Nernst coefficient . In order to ensure robust proximity induced s-wave superconductivity, we took special care to ensure considerable mixing of $m_j = \pm 1/2$ states in the top hole-doped valence band. These results provide generic thermoelectric signatures useful in experimentally identifying the range of chemical potential, or doping levels, which can support a topological superconducting state[130].

We began chapter 3 by considering Majorana modes at the end of a one-dimensional spin-triplet superconductor with total Cooper pair spin projection $S_x = 0$ ($\Delta_{\uparrow\uparrow} = -\Delta_{\downarrow\downarrow} = p\Delta_0$). Surprisingly, we found that the spatially localized zero-modes are robust to many perturbations including mixing by the $S_z = 0$ component of the order parameter, transverse hopping (in quasi-1D systems) and non-magnetic disorder. While these perturbations can be explained by the presence of time reversal symmetry, we also found that the Majorana modes are robust to time reversal *breaking* perturbations including applied Zeeman fields, magnetic impurities, and other superconducting order parameters. By analyzing the topological properties of this model, we proved that the robustness to time reversal breaking stems from a hidden chiral symmetry, thus places the system in the BDI topological class with an integer $\mathbb{Z}$ invariant. BDI chiral symmetry forbids matrix elements between pairs of zero-energy modes bound to the same ends, in stark contrast with the previously held belief that any spatially localized Majorana modes must hybridize into conventional quasiparticle states. Given this result, we re-established the quasi-one-dimensional superconductors $(TMTSF)_2PF_6$ (a possible triplet superconductors with equal spin pairing, $\Delta_{\uparrow\uparrow}, \Delta_{\downarrow\downarrow} \neq 0, \Delta_{\uparrow\downarrow} = 0$, in applied magnetic fields) and $Li_{0.9}\ Mo_6\ O_{17}$ as natural hosts for Majorana fermions[97].

In addition to the spin-triplet p-wave superconducting systems described earlier, BDI chiral symmetry is also present in other systems. For example,a spin-orbit coupled nanowire or thin film deposited onto a $s_{\pm}$-wave superconductor falls into this category. Indeed, chiral symmetry explains the anomalous magnetic field response of all the DIII class topological superconducting systems proposed in the literature [96, 116]. This is because, in the example given chiral symmetry coexists with time-reversal symmetry which leads to doubly robust edge modes. By doubly robust we mean that a given perturbation may break one symmetry but not the other, and in this case zero-energy Majorana edge modes are protected by the remaining symmetry. In addition we provided a realistic route to engineer a "true" TR-invariant topological superconductor, i.e. one whose pair of Majorana bound states at each end is split by an applied Zeeman field in arbitrary direction. We also prove that quite generally the splitting of the Majorana bound states in a true time reversal invariant system by time reversal breaking fields is highly anisotropic in spin space. The spatial anisotropy can be used as an experimental signature – the energy splitting can in principle be observed in near zero-bias differential conductance measurements – to identify this exotic state of matter.

Although not considered in the original classification of topologically ordered free fermion systems, crystallographic or spatial symmetries may also stabilize topologically order. Therefore, we constructed a quasi-one-dimensional system with reflection symmetry, i.e. one comprised of one-dimensional topological chains coupled by transverse hopping. We then showed how in the eigenbasis of the spatial reflection op-

erator the total Hamiltonian can be decomposed into non-interacting block diagonal sector. Each individual block represents a non-interacting subspace of the full Hamiltonian and may or may not obey particle hole symmetry, with the details depending on the specific microscopic model. For each particle-hole symmetry preserving sub-sector symmetry one may define a topological invariant, counting the number Majorana zero modes within that sub-sector. In a two dimensional system, which is translationally invariant system along the transverse direction, the Majorana states form a flat band constrained to zero energy. [131].

Afterwards, in chapter 4, we used the chiral symmetry to explain the persistent zero-bias peak recently found in recent STM measurements[98]. In their setup, magnetic atoms (Fe) are deposited onto the surface of an s-wave superconductor with spin-orbit interaction(Pb). Next, the surface atoms self assemble into one-dimensional chains (alternatively one could call this a ferromagnetic nanowire) in a controlled annealing process. With no fine tuning, evidence for Majorana bound states appease in a peak in the zero-bias scanning tunneling conductance at the wire endpoints. Modeling a finite width ferromagnetic based topological superconductor we confirm that a zero-bias signature is kneed a generic feature. Furthermore, we show that increasing the system width will enhance the magnitude of the observed zero-bias signal, even at finite temperature. This simple width manipulation can therefore be used as a diagnostic tool to determine if the character of the topological phase is chiral in nature[132].

5.2 Future Directions

5.2.1 Multiplet exchance statistics

Earlier, we showed how doublets (multiplets) of Majorana bound states arise in class DIII (BDI) systems and that hybridization between these spatially overlapping states is prevented by a time-reversal symmetry with $T^2 = -1(+1)$. Ivanov established that the exchange statistics of Majorana fermions bound to vortex cores in a two-dimensional chiral p-wave superconductor (class D) is identical to that of the Moore-Read (Pfaffian) quantum Hall state. Ivanov's analysis[13] is however limited to the case of spatially isolated zero modes. In the event that Majorana fermions are found in a naturally occurring one-dimensional topological superconductor belonging to BDI or DIII they should appear in clusters consisting of pairs or multiplets. The first important question is, how are exchange statistics modified by this clustering? And secondly, if the non-Abelian statistics are preserved, how robust are the symmetries which forbid hybridization and 'bind' the clusters? The two questions can be summarized by asking, what are the exchange statistics, and to which

perturbations are they robust. The first work to address this issue [90] claims that time-reversal invariance protects the non-Abelian braiding statistics in a $\mathbb{Z}_2$ TR-invariant superconductor. However, recent work[133] has shown that local adiabatic perturbations can cause a rotation in the space spanned by the Kramers pair. More work is surely needed to resolve this conflict and to generalize it to incorporate BDI Majorana multiplets.

5.2.2 Unitary symmetry classification

A&Z introduced the classification of Hamiltonian on the basis of particle-hole and time-reversal symmetries, both of which are represented by anti-unitary operators. These two fundamental symmetries were chosen because they are thought to be more "robust" than unitary symmetries which are typically broken by disorder [134]. For example, consider the translational symmetry of a perfect crystal. We know that real crystals almost always contain dislocations, atomic substitutions or some other impurity which breaks the global translational symmetry. For this reason crystallographic (and spin-rotation?) symmetries are not considered. In contrast time-reversal and charge-conjugation symmetries are intrinsic symmetries, robust to large classes of perturbations, including all the aforementioned crystal deformations.

Despite their deficiencies, unitary symmetries have been tremendously successful in predicting and understanding condensed matter phenomena. Most notably band theory, which correctly describes the electronic strutter of many materials, is formulated in momentum space. How do we then rectify these two opposing viewpoints? Perhaps we must distinguish between weak and strong symmetry breaking, where symmetry protected modes are unaffected in the former case. Another (possibly related) route to enhancing the existing topological classification may be provided by statistical topological phases of matter [135]. In a statistical topological insulator edge modes are protected against localization by the statistical properties of a disordered ensemble. One may even claim this explains why the Quantum Spin Hall effect, a state which requires time-reversal symmetry, was detected using photoemission [118] experiments even though electro*magnetic* radiation locally breaks time-reversal symmetry. Additionally, the interplay between the d-vector direction, spin-orbit coupling or Zeeman coupling orientations should be studied since it is the geometric relationship between these vector quantities which determines the presence or absence of the orthogonal chiral symmetry. Does the superconducting d-vector choose a particular direction in the presence of a magnetic field? How about in the presence of a (spatially dependent) spin-orbit field? These questions may be answered by calculating the proximity induced pair potential in a self-consistent manner.

5.2.3 Interactions and Fractionalized Majorana Fermions

Gapped systems which may not be adiabatically connected without closing the bulk gap are topologically distinct. Interactions do not affect generally affect topological phases since adding small interaction perturbations should not destroy the bulk gap. In a system classified by a $\mathbb{Z}_2$ invariant a single set of edge modes are present in the non-trivial phase (no edge states are permitted in the trivial case). A $\mathbb{Z}$ topological index allows for any infinite number of topological phases, each with a different integer number of edge states. [136, 137] showed that interactions reduce the topological invariant from $\mathbb{Z}$ to $\mathbb{Z}_8$. However this limitation can be overcome by considering only edge theories where this argument does not apply [138]. Indeed in this case it has been shown that interactions (by coupling with fractional quantum hall states) can actually fractionalize Majorana excitations into $\mathbb{Z}_n$ parafermions.

Because MFs are Ising anyons and their topological braids do not support *universal* computation, and therefore must be supplemented with some topologically unprotected operations, they are not the end goal concerning quantum computation. However, the hypothetical parafermions arising from the Read-Rezayi state, which may explain the $\nu = 12/5$ fractional quantum Hall effect, are Fibonacci anyons and can indeed be used to a enact universal quantum logic gates. Analogous to the way in which the semiconducting Majorana nanowire mimics the physics of the Moore-Read $\nu = 5/2$ Pfaffian wavefunction, the goal is to recreate the Read-Rezayi state in superconducting heterostructures[139]. This can be accomplished by combining understood topological states of matter along with quantum hall states to further "fractionalize" MFs into parafermionic excitations. Knowledge and experience gained from the first two research goals should prove useful in the detection, and hopefully manipulation of parafermionic modes.

Bibliography

[1] E. Schrodinger. An undulatory theory of the mechanics of atoms and molecules. *Phys. Rev.*, 28(1049), 1926.

[2] D. Griffiths. *Introduction to Elementary Particles*. Wiley-VCH, 2004.

[3] O. Klein. *Z. Phys.*, 37:895–906, 1926.

[4] W. Gordon. Z. phys. 40(117–133), 1926–1927.

[5] P. A. M. Dirac. The quantum theory of the electron. *Proceedings of the Royal Society A*, 117(778):610, 1928.

[6] R. Jackiw. Emergent fractional charge and multiple majoranas. *arXiv*, (1404.6200), 2014.

[7] C. Cowan, F. Reines, F. Harrison, H. Kruse, and A. McGuire. Detection of the free neutrino: a confirmation. *Science*, 124:103–104, 1956.

[8] F.T. Avignone, S. R. Elliott, and J. Engel. Double beta decay, majorana neutrinos, and neutrino mass. *Rev. Mod. Phys.*, 80(481-516), 2008.

[9] R. Jackiw and C. Rebbi. *Phys. Rev. D.*, 13(3398), 1976.

[10] C. Nayak, S.H. Simon, A. Stern, M. Freedman M, and S. Das Sarma. Non-abelian anyons and topological quantum computation. *Rev. Mod. Phys.*, 80:1083–1159, 2008.

[11] F. Wilczek. Quantum mechanics of fractional-spin particles. *Physical Review Letters (14): 957–959*, 49:957, 1982.

[12] R. B. Laughlin. Anomalous quantum hall effect: An incompressible quantum fluid with fractionally charged excitations. *Phys. Rev. Lett.*, 50(18):1395–98, 1983.

[13] D.A. Ivanov. Non-abelian statistics of half-quantum vortices in p-wave superconductors. *Phys. Rev. Lett.*, 86:268–271, 2001.

[14] J. Chalker. Quantum theory of condensed matter.

[15] C. Caroli, P.-G. de Gennes, and J. Matricon. Bound fermion states on a vortex line in a type ii superconductor. *Phys. Lett.*, 9:307, 1964.

[16] C.W.J. Beenakker. Search for majorana fermions in superconductors. *Annual Review of Condensed Matter Physics*, 4:113–136, 2013.

[17] J.D. Sau, R.M. Lutchyn, S. Tewari, and S. Das Sarma. Generic new platform for topological quantum computation using semiconductor heterostructures. *Phys. Rev. Lett.*, 104(040502), 2010.

[18] S. Tewari, J.D. Sau, and S. Das Sarma. A theorem for the existence of majorana fermion modes in spin-orbit-coupled semiconductors. *Annals of Physics*, 325(219), 2010.

[19] J. D. Sau, S. Tewari, R. M. Lutchyn, T. Stanescu, and S. Das Sarma. Non-abelian quantum order in spin-orbit-coupled semiconductors: Search for topological majorana particles in solid-state systems. *Phys. Rev. B*, 82(214509), 2010.

[20] C. Zhang, S. Tewari, R. M. Lutchyn, and S. Das Sarma. px + ipy superfluid from s-wave interactions of fermionic cold atoms. *Phys. Rev. Lett.*, 101(160401), 2008.

[21] M. Sato, Y. Takahashi, and S. Fujimoto. Non-abelian topological order in s-wave superfluids of ultracold fermionic atoms. *Phys. Rev. Lett.*, 103(020401), 2009.

[22] J. Alicea. Majorana fermions in a tunable semiconductor device. *Phys. Rev. B*, 81(125318), 2010.

[23] L. Mao, J. Shi, Q. Niu, and C. Zhang. Superconducting phase with a chiral f-wave pairing symmetry and majorana fermions induced in a hole-doped semiconductor. *Phys. Rev. Lett.*, 106(157003), 2011.

[24] R.M. Lutchyn, J.D. Sau, and S. Das Sarma. Majorana fermions and a topological phase transition in semiconductor-superconductor heterostructures. *Phys. Rev. Lett.*, 105(077001), 2010.

[25] Y. Oreg, G. Refael, and F. von Oppen. Helical liquids and majorana bound states in quantum wires. *Phys. Rev. Lett.*, 105(177002), 2010.

[26] L. Mao, M. Gong, E. Dumitrescu, S. Tewari, and C. Zhang. Hole-doped semiconductor nanowire on top of an s-wave superconductor: A new and experimentally accessible system for majorana fermions. *Phys. Rev. Lett.*, 108(177001), 2012.

[27] J. Alicea, Y. Oreg, G. Refael, F. von Oppen, and M. P. A. Fisher. Non-abelian statistics and topological quantum information processing in 1d wire networks. *Nature Physics*, 7:412–417, 2011.

[28] F. Hassler, A. R. Akhmerov, C.-Y Hou, and C. W. J. Beenakker. Anyonic interferometry without anyons: how a flux qubit can read out a topological qubit. *New J. Phys.*, 12(125002), 2010.

[29] J. D. Sau, S. Tewari, and S. Das Sarma. Universal quantum computation in a semiconductor quantum wire network. *Phys. Rev. A*, 82(052322), 2010.

[30] C. Nayak and F. Wilczek. 2n quasihole states realize 2n1-dimensional spinor braiding statistics in paired quantum hall states. *Nucl. Phys. B*, 479(529), 1996.

[31] N. Read and D. Green. Paired states of fermions in two dimensions with breaking of parity and time-reversal symmetries, and the fractional quantum hall effect. *Phys. Rev. B*, 61(10267), 2000.

[32] A. Stern, F. von Oppen, and E. Mariani. Geometric phases and quantum entanglement as building blocks for non-abelian quasiparticle statistics. *Phys. Rev. B*, 70(205338), 2004.

[33] A. Y. Kitaev. Fault-tolerant quantum computation by anyons. *Ann. Phys.*, 303:2–30, 2003.

[34] S. Bravyi and A. Kitaev. Universal quantum computation with ideal clifford gates and noisy ancillas. *Phys. Rev. A*, 71(022316), 2005.

[35] H.B. Nielsen and M. Ninomiya. The adler-bell-jackiw anomaly and weyl fermions in a crystal. *Phys. Lett. B*, 130(6):389–396, 1983.

[36] A. Kitaev. Unpaired majorana fermions in quantum wires. *Physics-Uspekhi*, 44:131, 2001.

[37] M. Berry. Quantal phase factors accompanying adiabatic changes. *Proc. R. Soc. London, Ser. A*, 392(1802):45–57, 1984.

[38] G. Sundaram and Q. Niu. Wave-packet dynamics in slowly perturbed crystals: Gradient corrections and berry-phase effects. *Phys. Rev. B*, 59(23):14915, 1999.

[39] D. Xiao, M.-C. Chang, and Q. Niu. Berry phase effects on electronic properties. *Rev. Mod. Phys.*, 82:1959, 2010.

[40] N. Nagaosa, J. Sinova, S. Onoda, A. H. MacDonald, and N. P. Ong. Anomalous hall effect. *Rev. Mod. Phys.*, 82:1539, 2010.

[41] D. Xiao, W. Yao, and Q. Niu. Valley-contrasting physics in graphene: Magnetic moment and topological transport. *Phys. Rev. Lett.*, 97(236809), 2006.

[42] D. Xiao, Y. Yao, Z. Fang, and Q. Niu. Berry-phase effect in anomalous thermoelectric transport. *Phys. Rev. Lett.*, 97(026603), 2006.

[43] C. Zhang, S. Tewari, V. M. Yakovenko, and S. Das Sarma. Anomalous nernst effect from a chiral d-density-wave state in underdoped cuprate superconductors. *Phys. Rev. B , ()*, 78(174508), 2008.

[44] C. Zhang, S. Tewari, and S. Das Sarma. Berry-phase-mediated topological thermoelectric transport in gapped single and bilayer graphene. *Phys. Rev. B*, 79(245424), 2009.

[45] T. Jungwirth, Q. Niu, and A. H. MacDonald. Anomalous hall effect in ferromagnetic semiconductors. *Phys. Rev. Lett.*, 88(207208), 2002.

[46] S. Murakami, N. Nagaosa, and S.-C. Zhang. Dissipationless quantum spin current at room temperature. *Science*, 301:1348, 2003.

[47] Z. Fang, N. Nagaosa, K. S. Takahashi, A. Asamitsu, T. Ogasawara R. Mathieu, H. Yamada, M. Kawasaki, Y. Tokura, and K. Terakura. The anomalous hall effect and magnetic monopoles in momentum space. *Science*, 302:92–95, 2003.

[48] W.-L. Lee, S. Watauchi, V. L. Miller, R. J. Cava, and N. P. Ong. Anomalous hall heat current and nernst effect in the cucr2se(4x)br(x) ferromagnet. *Phys. Rev. Lett.*, 93(226601), 2004.

[49] J. Shi, G. Vignale, D. Xiao, and Q. Niu. Quantum theory of orbital magnetization and its generalization to interacting systems. *Phys. Rev. Lett.*, 99(197202), 2007.

[50] S. Goswami, C. Siegert, M. Pepper, I. Farrer, D. A. Ritchie, and A. Ghosh. Signatures of an anomalous nernst effect in a mesoscopic two-dimensional electron system. *Phys. Rev. B*, 83(073302), 2011.

[51] A. Dyrdal and J. Barnas. Topological spin hall and spin nernst effects in a bilayer graphene. *J. Phys. Cond. Matter*, 24(275302), 2012.

[52] S.-G. Cheng, Y. Xing, Q.-F. Sun, and X. C. Xie. Spin nernst effect and nernst effect in two-dimensional electron systems. *Phys. Rev. B*, 78(045302), 2008.

[53] Y. Zhang and C. Zhang. Quantized anomalous hall insulator in a nanopatterned two-dimensional electron gas. *Phys. Rev. B*, 84(085123), 2011.

[54] R. Winkler. *Spin-Orbit Coupling Effects in Two-Dimensional Electron and Hole Systems*. Springer, 2003.

[55] G. Fishman. Hole subbands in strained quantum-well semiconductors in [hhk] directions. *Phys. Rev. B*, 52(15):11132, 1995.

[56] M. Gong, L. Mao, S. Tewari, and C. Zhang. Majorana fermions under uniaxial stress in semiconductor-superconductor heterostructures. *Phys. Rev. B*, 87(060502(R)), 2013.

[57] L. Fu and C.L. Kane. Superconducting proximity effect and majorana fermions at the surface of a topological insulator. *Phys. Rev. Lett.*, 100(096407), 2008.

[58] V. Mourik, K. Zuo, S.M. Frolov, SR. Plissard, E.P.A.M Bakkers EPAM, and L.P. Kouwenhoven. Signatures of majorana fermions in hybrid superconductor-semiconductor nanowire devices. *Science*, 336(1003–7), 2012.

[59] L. P. Rokhinson, X. Liu, and J. K. Furdyna. The fractional a.c. josephson effect in a semiconductor–superconductor nanowire as a signature of majorana particles. *Nature Physics*, 8:795–799, 2012.

[60] M. T. Deng, C. L. Yu, G. Y. Huang, M. Larsson, P. Caroff, and H. Q. Xu. Anomalous zero-bias conductance peak in a nb–insb nanowire–nb hybrid device. *Nano Lett.*, 12:6414, 2012.

[61] A. Das, Y. Ronen, Y. Most, Y. Oreg, M. Heiblum, and H. Shtrikman. Zero-bias peaks and splitting in an al–inas nanowire topological superconductor as a signature of majorana fermions. *Nature Phys.*, 8:887, 2012.

[62] H. O. H. Churchill, V. Fatemi, K. Grove-Rasmussen, M. T. Deng, P. Caroff, H. Q. Xu, and C. M. Marcus. Superconductor-nanowire devices from tunneling to the multichannel regime: Zero-bias oscillations and magnetoconductance crossover. *Phys. Rev. B*, 87(241401(R)), 2013.

[63] A. D. K. Finck, D. J. Van Harlingen, P. K. Mohseni, K. Jung, and X. Li. Anomalous modulation of a zero-bias peak in a hybrid nanowire-superconductor device. *Phys. Rev. Lett.*, 110(126406), 2013.

[64] J. Alicea. New directions in the pursuit of majorana fermions in solid state systems. *Rep. Prog. Phys.*, 2012(076501), 75.

[65] M. Leijnse and K. Flensberg. Introduction to topological superconductivity and majorana fermions. *Semicond. Sci. Technol.*, 27(124003), 2012.

[66] T.D. Stanescu and S. Tewari. Majorana fermions in semiconductor nanowires: fundamentals, modeling, and experiment. *J. Phys. Condens. Matter*, 25(233201), 2013.

[67] A. P. Schnyder, S. Ryu, A. Furusaki, and A. W. W. Ludwig. Classification of topological insulators and superconductors in three spatial dimensions. *Phys. Rev. B*, 78(195125), 2008.

[68] A. Y. Kitaev. Periodic table for topological insulators and superconductors. *AIP Conf. Proc.*, 1134:22, 2009.

[69] S. Ryu, A. Schnyder, A. Furusaki, and A. W. W. Ludwig. Topological insulators and superconductors: ten-fold way and dimensional hierarchy. *New J. Phys.*, 12(065010), 2010.

[70] I. J. Lee, S. E. Brown, W. G. Clark, M. J. Strouse, M. J.Naughton, W. Kang, and P. M. Chaikin. Triplet superconductivity in an organic superconductor probed by nmr knight shift. *Phys. Rev. Lett.*, 88(017004), 2001.

[71] I. J. Lee, D. S. Chow, W. G. Clark, M. J. Strouse, M. J. Naughton, P. M. Chaikin, and S. E. Brown. Evidence from 77se knight shifts for triplet superconductivity in (tmtsf)2pf6. *Phys. Rev. B*, 68(092510), 2003.

[72] J. Shinagawa, Y. Kurosaki, F. Zhang, C. Parker, S. E. Brown, D. Jérome, J. B. Christensen, and K. Bechgaard. Superconducting state of the organic conductor (tmtsf)2clo4. *Phys. Rev. Lett.*, 98(147002), 2007.

[73] A. G. Lebed, K. Machida, and M. Ozaki. Triplet electron pairing and anisotropic spin susceptibility in organic superconductors (tmtsf)2x. *Phys. Rev. B*, 62(2):R795–R798, 2000.

[74] A. G. Lebed and O. Sepper. Possible triplet superconductivity in the quasi-one-dimensional conductor li0.9mo6o17. *Phys. Rev. B*, 87(100511), 2013.

[75] A. Ardavan, S. Brown, S. Kagoshima, K. Kanoda, K. Kuroki, H. Mori, M. Ogata, S. Uji, and J. Wosnitza. Recent topics of organic superconductors. *J. Phys. Soc. Jpn.*, 81(011004), 2012.

[76] C. Bourbonnais and D. Jerome. *Physics of Organic Superconductors and Conductors*. Springer, 2008.

[77] W. Cho, R. Thomale, S. Raghu, and S. A. Kivelson. Band structure effects on the superconductivity in hubbard models. *Phys. Rev. B*, 88(064505), 2013.

[78] K. Sengupta, I. Zutic, H.-J. Kwon, V. M. Yakovenko, and S. Das Sarma. Midgap edge states and pairing symmetry of quasi-one-dimensional organic superconductors. *Phys. Rev. B*, 63(144531), 2001.

[79] K. T. Law, P. A. Lee, and T. K. Ng. Majorana fermion induced resonant andreev reflection. *Phys. Rev. Lett.*, 103(237001), 2009.

[80] H.-J. Kwon, K. Sengupta, and Victor M. Yakovenko. Fractional ac josephson effect in p- and d-wave superconductors. *The European Physical Journal B ,*, 37:349, 2004.

[81] H.-J. Kwon, V. M. Yakovenko, and K. Sengupta. Fractional ac josephson effect in unconventional superconductors. *Low Temp. Phys.*, 30:613, 2004.

[82] S. Tewari and J. D. Sau. Topological invariants for spin-orbit coupled superconductor nanowires. *Phys. Rev. Lett.*, 109(150408), 2012.

[83] S. Tewari, T.D. Stanescu, J.D. Sau, and S. Das Sarma. Topological minigap in quasi-one-dimensional spin-orbit-coupled semiconductor majorana wires. *Phys. Rev. B*, 86(024504), 2012.

[84] M. Diez, J. P. Dahlhaus, M. Wimmer, and C. W. J. Beenakker. Andreev reflection from a topological superconductor with chiral symmetry. *Phys. Rev. B*, 86(094501), 2012.

[85] L. M. Wong and K. T. Law. Majorana kramers doublets in dx2y2-wave superconductors with rashba spin-orbit coupling. *Phys. Rev. B*, 86(184516), 2012.

[86] S. Deng, L. Viola, and G. Ortiz. Majorana modes in time-reversal invariant s-wave topological superconductors. *Phys. Rev. Lett.*, 108(036803), 2012.

[87] A. Keselman, L. Fu, A. Stern, and E. Berg. Inducing time-reversal-invariant topological superconductivity and fermion parity pumping in quantum wires. *Phys. Rev. Lett.*, 111(116402), 2013.

[88] F. Zhang, C. L. Kane, and E. J. Mele. Time-reversal-invariant topological superconductivity and majorana kramers pairs. *Phys. Rev. Lett.*, 111(056402), 2013.

[89] S. Deng, G. Ortiz, and L. Viola. Multiband s-wave topological superconductors: role of dimensionality and magnetic field response. *Phys. Rev. B*, 87(205414), 2013.

[90] X. J. Liu, C. L. M. Wong, and K. T. Law. Non-abelian majorana doublets in time-reversal-invariant topological superconductors. *Phys. Rev. X*, 4(021018), 2014.

[91] E. Gaidamauskas, J. Paaske, and K. Flensberg. Majorana bound states in two-channel time-reversal-symmetric nanowire systems. *Phys. Rev. Lett.*, 112(126402), 2014.

[92] S. Nakosai, J. C. Budich, Y. Tanaka, B. Trauzettel, and N. Nagaosa. Majorana bound states and nonlocal spin correlations in a quantum wire on an unconventional superconductor. *Phys. Rev. Lett.*, 110(117002), 2013.

[93] X.L. Qi, T. L. Hughes, and S.C. Zhang. Topological invariants for the fermi surface of a time-reversal-invariant superconductor. *Phys. Rev. B*, 81(134508), 2010.

[94] M. Sato, Y. Tanaka, K. Yada, and T. Yokoyama. Topology of andreev bound states with flat dispersion. *Phys. Rev. B*, 83(224511), 2011.

[95] J. C. Budich and E. Ardonne. Topological invariant for generic 1d time reversal symmetric superconductors in class diii. *Phys. Rev. B*, 88(134523), 2013.

[96] F. Zhang and C. L. Kane. Topological mirror superconductivity. *Phys. Rev. Lett.*, 111(056403), 2013.

[97] E. Dumitrescu and S. Tewari. Topological properties of the time-reversal-symmetric kitaev chain and applications to organic superconductors. *Phys. Rev. B*, 88(220505(R)), 2013.

[98] S. Nadj-Perge, I. K. Drozdov, J. Li, H. Chen, S. Jeon, J. Seo, A. H. MacDonald, B. A. Bernevig, and A. Yazdani. Observation of majorana fermions in ferromagnetic atomic chains on a superconductor. *Science*, 346(6209):602–607, 2014.

[99] S. Nadj-Perge, I. K. Drozdov, B. A. Bernevig, and A. Yazdani. Proposal for realizing majorana fermions in chains of magnetic atoms on a superconductor. *Phys. Rev. B*, 88(020407(R)), 2013.

[100] F. Pientka, L. I. Glazman, and F. von Oppen. Topological superconducting phase in helical shiba chains. *Phys. Rev. B , ()*., 88(155420), 2013.

[101] F. Pientka, L. I. Glazman, and F. von Oppen. Unconventional topological phase transitions in helical shiba chains. *Phys. Rev. B*, 89(180505(R)), 2014.

[102] T.-P. Choy, J. M. Edge, A. R. Akhmerov, and C. W. J. Beenakker. Majorana fermions emerging from magnetic nanoparticles on a superconductor without spin-orbit coupling. *Phys. Rev. B*, 84(195442), 2011.

[103] L. Yu. Bound state in superconductors with paramagnetic impurities. *Acta Phys. Sin.*, 21:75–91, 1965.

[104] H. Shiba. Classical spins in superconductors. *Prog. Theor. Phys.*, 40:435, 1968.

[105] A. I. Rusinov. On the theory of gapless superconductivity in alloys containing paramagnetic impurities. *JETP Lett.*, 29(6):1101, 1969.

[106] J. Klinovaja, P. Stano, A. Yazdani, and D. Loss. Topological superconductivity and majorana fermions in rkky systems. *Phys. Rev. Lett.*, 111(186805), 2013.

[107] M. M. Vazifeh and M. Franz. Self-organized topological state with majorana fermions. *Phys. Rev. Lett.*, 111(206802), 2013.

[108] Y. Kim, M. Cheng, B. Bauer, R. M. Lutchyn, and S. Das Sarma. Helical order in one-dimensional magnetic atom chains and possible emergence of majorana bound states. *Phys. Rev. B.*, 90(060401(R)), 2014.

[109] P. M. R. Brydon, H.-Y. Hui, and J. D. Sau. Topological shiba chain from spin-orbit coupling. *arXiv:1407.6345 [cond-mat.mes-hall]*, 2014.

[110] M. Duckheim and P. W. Brouwer. Andreev reflection from noncentrosymmetric superconductors and majorana bound-state generation in half-metallic ferromagnets andreev reflection from noncentrosymmetric superconductors and majorana bound-state generation in half-metallic ferromagnets. *Phys. Rev. B*, 83(054513), 2011.

[111] S. Takei and V. Galitski. Microscopic theory for a ferromagnetic nanowire/superconductor heterostructure: Transport, fluctuations, and topological superconductivity. *Phys. Rev. B*, 86(054521), 2012.

[112] J. Wang et. al. Interplay between superconductivity and ferromagnetism in crystalline nanowires. *Nature Phys.*, 6:389–394, 2010.

[113] H.-Y. Hui, P. M. R. Brydon, J. D. Sau, S. Tewari, and S. Das Sarma. Majorana fermions in a ferromagnetic wire on the surface of a bulk spin-orbit coupled s-wave superconductor. *arXiv:1407.7519 [cond-mat.mes-hall]*, 2014.

[114] K. Sengupta, I. Zutic, H.-J. Kwon, V. M. Yakovenko, and S. Das Sarma. Midgap edge states and pairing symmetry of quasi-one-dimensional organic superconductors. *Phys. Rev. B*, 63(144531), 2001.

[115] S. Tewari, J. D. Sau, and S. Das Sarma. A theorem for the existence of majorana fermion modes in spin-orbit-coupled semiconductors. *Ann. Phys.*, 325(219), 2010.

[116] E. Dumitrescu, J.D. Sau, and S. Tewari. Magnetic field response and chiral symmetry of time reversal invariant topological superconductors. *arXiv:1310.7938 [cond-mat.mes-hall]*, 2014.

[117] A. Altland and M.R. Zirnbauer. Nonstandard symmetry classes in mesoscopic normal-superconducting hybrid structures. *Phys. Rev. B 55*, 55(2):1142–61, 1997.

[118] M. Z. Hasan and C. L. Kane. Colloquium: Topological insulators. *Rev. Mod. Phys.*, 82:3045, 2010.

[119] J.C. Budich and E. Ardonne. Topological invariant for generic 1d time reversal symmetric superconductors in class diii. *Phys. Rev. B*, 88(134523), 2013.

[120] S. Tewari and J. D. Sau. Topological invariants for spin-orbit coupled superconductor nanowires. *Phys. Rev. Lett.*, 109(150408), 2012.

[121] C. Qu, M. Gong, Y. Xu, S. Tewari, and C. Zhang. Majorana fermions in quasi-1d and higher dimensional ultracold fermionic optical lattices. *arXiv:1310.7557 [cond-mat.quant-gas]*, 2013.

[122] G.E. Blonder, M. Tinkhan, and T.M. Klapwijk. Transition from metallic to tunneling regimes in superconducting microconstrictions: Excess current, charge imbalance, and supercurrent conversion. *Phys. Rev. B*, 25:4515–32, 1982.

[123] P. San-Jose, E. Prada, and R. Aguado. ac josephson effect in finite-length nanowire junctions with majorana modes. *Phys. Rev. Lett.*, 108(257001), 2012.

[124] C. W. Groth, M. Wimmer, A. R. Akhmerov, and X. Waintal. Kwant: a software package for quantum transport. *New J. Phys.*, 16(063065), 2014.

[125] K. Flensberg. Tunneling characteristics of a chain of majorana bound states. *Phys. Rev. B*, 82(180516(R)), 2010.

[126] M. Cheng, R. M. Lutchyn, V. Galitski, and S. Das Sarma. Splitting of majorana-fermion modes due to intervortex tunneling in a px+ipy superconductor. *Phys. Rev. Lett. 103,*, 103(107001), 2009.

[127] J. D. Sau, S. Tewari, and S. Das Sarma. Experimental and materials considerations for the topological superconducting state in electron- and hole-doped semiconductors: Searching for non-abelian majorana modes in 1d nanowires and 2d heterostructures. *Phys. Rev. B*, 85(064512), 2012.

[128] M. Houzet, J. S. Meyer, D. M. Badiane, and L. I. Glazman. Dynamics of majorana states in a topological josephson junction. *Phys. Rev. Lett.*, 111(046401), 2013.

[129] M. Tinkham. *Introduction to Superconductivity*. Dover Publ., New York, 2004.

[130] E. Dumitrescu, C. Zhang, D.C. Marinescu, and S. Tewari. Topological thermoelectric effects in spin-orbit coupled electron and hole doped semiconductors. *Phys. Rev. B*, 85(245301), 2012.

[131] E. Dumitrescu, T. D. Stanescu, and S. Tewari. Hidden symmetry decoupling of majorana fermions. *arXiv:1403.3093 [cond-mat.mes-hall]*, 2014.

[132] E. Dumitrescu, B. Roberts, S. Tewari, J.D. Sau, and S. Das Sarma. Majorana fermions in chiral topological ferromagnetic nanowires. *arXiv:1410.5412 [cond-mat.supr-con]*, 2014.

[133] K. Wolms, A. Stern, and K. Flensberg. Local adiabatic mixing of kramers pairs of majorana bound states. *arXiv:1405.5104 [cond-mat.mes-hall]*, 2014.

[134] C. W. J. Beenakker. Random-matrix theory of majorana fermions and topological superconductors. *arXiv:1407.2131 [cond-mat.mes-hall]*, 2014.

[135] I. C. Fulga, B. van Heck, J. M. Edge, and A. R. Akhmerov. Statistical topological insulators. *Phys. Rev. B*, 89(155424), 2014.

[136] L. Fidkowski and A. Kitaev. Topological phases of fermions in one dimension. *Phys. Rev. B*, 2011(075103), 83.

[137] A. M. Turner, F. Pollmann, and E. Berg. Topological phases of one-dimensional fermions: An entanglement point of view. *Phys. Rev. B*, 83(075102), 2011.

[138] D. J. Clarke, J. Alicea, and K. Shtengel. Exotic circuit elements from zero-modes in hybrid superconductor–quantum-hall systems. *Nature Physics*, 10:877–882, 2014.

[139] D. J. Clarke, J. Alicea, and K. Shtengel. Exotic non-abelian anyons from conventional fractional quantum hall states. *Nature Commun.*, 4(1348), 2013.